



**INVESTIGATION OF THE POTENTIAL FOR FTIR AS A NONDESTRUCTIVE
INSPECTION TECHNIQUE FOR AIRCRAFT COATING DEGRADATION**

THESIS

Hans G. Korth, Captain, USAF

AFIT-ENP-14-M-19

**DEPARTMENT OF THE AIR FORCE
AIR UNIVERSITY**

AIR FORCE INSTITUTE OF TECHNOLOGY

Wright-Patterson Air Force Base, Ohio

**DISTRIBUTION STATEMENT A.
APPROVED FOR PUBLIC RELEASE; DISTRIBUTION UNLIMITED.**

The views expressed in this thesis are those of the author and do not reflect the official policy or position of the United States Air Force, Department of Defense, or the United States Government. This material is declared a work of the U.S. Government and is not subject to copyright protection in the United States.

**INVESTIGATION OF THE POTENTIAL FOR FTIR AS A NONDESTRUCTIVE INSPECTION
TECHNIQUE FOR AIRCRAFT COATING DEGRADATION**

THESIS

Presented to the Faculty
Department of Engineering Physics
Graduate School of Engineering and Management
Air Force Institute of Technology
Air University
Air Education and Training Command
In Partial Fulfillment of the Requirements for the
Degree of Master of Science

Hans G. Korth, BS

Captain, USAF

March 2014

DISTRIBUTION STATEMENT A.
APPROVED FOR PUBLIC RELEASE; DISTRIBUTION UNLIMITED.

**INVESTIGATION OF THE POTENTIAL FOR FTIR AS A NONDESTRUCTIVE INSPECTION
TECHNIQUE FOR AIRCRAFT COATING DEGRADATION**

Hans G. Korth, BS

Captain, USAF

Approved:

//Signed//
Timothy Zens, PhD (Chairman)

06 March 2014
Date

//Signed//
Kevin Gross, PhD (Member)

06 March 2014
Date

//Signed//
Adam Cooney, PhD (Member)

11 March 2014
Date

Abstract

Polyurethane-based aircraft coating samples were examined using Diffuse Reflectance Infrared Fourier Transform spectroscopy (DRIFTS) to determine its potential use as a nondestructive inspection technique capable of characterizing the state of degradation and predicting the remaining service life. Two sample sets of fielded coating layer configurations were aged in an autoclave; each containing four samples. Sample set A contained two as-cured samples and two samples treated to a level of visual degradation. Sample set B contained one sample left as-cured, one aged for one day, one aged for two days, and one aged for four days to generate a continuum of degradation levels. DRIFTS spectra were collected on sample set B and singular value decomposition (SVD) was used to reveal trends between the degradation levels. Linear discriminant analysis (LDA) was then applied to the SVD coefficients to determine the most accurate spectral band for classification of unknown degradation. The 1220-850 cm^{-1} band, the fingerprint region of polymers, proved to be the most accurate at discerning between degradation levels with 98.3% accuracy. The approach was then applied to sample set A using one each of the as-cured and degraded samples as unknown degradation levels. The prediction accuracy of LDA was 100% for the as-cured sample, but only 28% for the visibly degraded sample in the fingerprint region. When the misclassification cost was adjusted, the accuracy improved to 78%. It is recommended that this work continue towards generating a field NDI technique.

Acknowledgements

I would like to thank my advisor, Maj Timothy Zens, and the members of the committee, Dr. Adam Cooney and Dr. Kevin Gross, for their guidance and patience. I appreciate all the lessons I learned from them throughout the course of this work.

I would also like to extend my gratitude to AFRL/RXCA for sponsoring this work and for the use of the equipment, lab space, and samples during this effort. Without those resources, this work would not have been accomplished.

Hans G. Korth

Table of Contents

	Page
Abstract	iv
Acknowledgements	v
List of Figures	ix
List of Tables.....	xv
I. Introduction.....	1
1.1. Background.....	1
1.2. Problem Statement	2
1.3. Research Objectives and Hypotheses	3
1.4. Research Focus	3
1.5. Methodology	4
1.6. Assumptions and Limitations	5
1.7. Implications	7
II. Theory.....	8
2.1. Polyurethane Degradation	8
2.1.1. Ultraviolet (UV) Exposure.....	9
2.1.2. Exposure to Moisture.....	10
2.1.3. Physical Aging.....	12
2.1.4. Accelerated Aging.....	13
2.2. Fourier Transform Infrared (FTIR) Spectroscopy.....	14
2.2.1. Vibrational Energies of Molecules.....	15
2.2.2. Interferograms and the Fourier Transform.....	20
2.2.3. Advantages of FTIR.....	22
2.2.4. Limitations of FTIR.....	23
2.2.5. Transmission FTIR.....	24
2.2.6. Reflectance FTIR.....	24
2.3. IR Spectrum Analysis	26
2.3.1. Spectra comparison.....	26
2.3.2. Pattern Recognition.....	28
2.3.3. Discriminant Analysis.	32
III. Experimental Methods.....	36
3.1. Sample Preparation	36
3.2. Equipment	38
3.3. Experimental Process	39
3.3.1. Device Characterization.	39

	Page
3.3.2. Sample Data Collection	47
3.4. Data Analysis	51
3.4.1. Singular Value Decomposition	52
3.4.2. Discriminant Analysis	59
3.4.3. Classifying New Sample Data	61
IV. Results and Discussion	64
4.1. Introduction.....	64
4.2. Degradation Detection	64
4.3. Singular Value Decomposition (SVD).....	66
4.3.1. $975-875 \text{ cm}^{-1}$ (10.3-11.4 μm).....	66
4.3.2. $1220-850 \text{ cm}^{-1}$ (8.2-11.8 μm).....	71
4.4. Spot to Spot Variation	76
4.5. Time-dependent Behavior.....	84
4.6. Classifying New Sample Data	94
4.6.1. Classification using Entire Sampling Spectrum	96
4.6.2. Classification using the Fingerprint Region.....	99
V. Conclusions	106
5.1. Accomplishments	106
5.2. Future Work	109
Appendix A. Device Calibration Data	112
A.1. Repeated Recalibration.....	112
A.2. Initial Calibration Only.....	114
Appendix B. Paint Sample Orientation Diagram	118
B.1. Paint Sample Orientation Diagram: Sample set A	118
B.2. Paint Sample Orientation Diagram: Sample set B	119
Appendix C. MATLAB Code.....	120
C.1. Discriminant Analysis by Band for Sample Set B	120
C.2. SVD Analysis and LDA Sample Set A (Entire Spectrum)	123
C.3. SVD Analysis and LDA Sample Set A (Fingerprint Region).....	125
Appendix D. SVD Coefficient Plots	128
D.1. SVD Coefficient Plots by Band for Sample Set B	128
D.1.1. $1150-850 \text{ cm}^{-1}$ (8.7-11.8 μm)	128
D.1.2. $1150-1050 \text{ cm}^{-1}$ (8.7-9.5 μm).....	130

	Page
D.1.3. 1200-800 cm^{-1} (8.3-12.5 μm)	131
D.1.4. 1800-800 cm^{-1} (5.6-12.5 μm)	133
D.1.5. 1800-1200 cm^{-1} (5.6-8.3 μm)	134
D.1.6. 1800-1450 cm^{-1} (5.6-6.9 μm)	136
D.1.7. 1800-1650 cm^{-1} (5.6-6.1 μm)	137
D.1.8. 1800-800 minus 1500-1200 cm^{-1}	139
D.2. Spot to Spot Variation	140
D.2.1. Untreated Sample (B1)	141
D.2.2. 24 Hour Treatment (B2)	143
D.2.3. 48 Hour Treatment (B3)	145
D.2.4. 96 Hour Treatment (B4)	147
D.3. Time-Dependent Behavior	149
D.3.1. Untreated Sample (B1)	149
D.3.2. 24 Hour Treatment (B2)	151
D.3.3. 48 Hour Treatment (B3)	153
D.3.4. 96 Hour Treatment (B4)	155
Appendix E. Discriminant Analysis Data	158
Appendix F. Data Normalization and SVD Details	162
F.1. Effect of Normalization on SVD Coefficient Clustering	162
F.2. SVD Details	164
References	167

List of Figures

	Page
Figure 2.1: Schematic diagram of polyurethane molecular structure.	8
Figure 2.2: Cross-section micrographs of a polyurethane aircraft coating	9
Figure 2.3: Tapping mode AFM images of filiform corrosion.....	11
Figure 2.4: A schematic of transmission and reflectance FTIR measurements.....	15
Figure 2.5: Diagram of particle interactions with electromagnetic radiation.....	16
Figure 2.6: Massless spring model used to represent harmonic oscillations.....	17
Figure 2.7: Schematic of the stretching and bending vibrational modes of CO ₂	19
Figure 2.8: Schematic diagram of a Michelson Interferometer	21
Figure 2.9: Schematic diagrams of specular and diffuse reflectance.....	25
Figure 3.1: Schematic of coating layer configuration used on all samples in the study	36
Figure 3.2: Pictures of the four samples in set B.....	37
Figure 3.3: Image of Agilent Exoscan 4100 used for FTIR spectra collection[32].	38
Figure 3.4: Mean reflectance with repeated recalibration	40
Figure 3.5: Reflectance spectrum for gold in the visible-IR spectrum	41
Figure 3.6: Mean-subtracted data with repeated calibration.....	42
Figure 3.7: Standard deviation as a percent of mean reflectance with repeated calibration	43
Figure 3.8: Mean reflectance without repeated calibration	44
Figure 3.9: Deviation from the mean by trial without repeated recalibration	44
Figure 3.10: Standard deviation as a percent of the mean without recalibration.....	45
Figure 3.11: Comparison of reflectance spectra collected on SiNC samples	46
Figure 3.12: Picture of the scene shown in the hyperspectral image in figure 3.13.....	48

	Page
Figure 3.13: Hyperspectral image taken in the 8-12 μm region of the IR spectrum.....	49
Figure 3.14: Example functions used to illustrate SVD analysis.....	53
Figure 3.15: A plot of the mean-subtracted data for the four example functions.	54
Figure 3.16: Plot of the first and second coefficients for the example functions.	55
Figure 3.17: A plot of the second and third coefficients for the four example functions.....	56
Figure 3.18: Plot of the original and reconstructed mean-subtracted functions.....	57
Figure 3.19: Plot of the original and reconstructed functions	57
Figure 3.20: Plot of first two coefficients generated from coating samples.....	58
Figure 3.21: Schematic of how discriminant analysis generates a classifier.....	60
Figure 3.22: Schematic of an idealized classification scenario.....	62
Figure 3.23: Plot of first two coefficients generated from the fingerprint region	63
Figure 4.1: Plot of the mean reflectance for sample set B collected the first week	65
Figure 4.2: Plot of the far end of the sampling spectrum for sample set B	65
Figure 4.3: Plot of the first two coefficients in the 975-875 cm^{-1} band for sample set B	67
Figure 4.4: Plot of first and third coefficients in the 975-875 cm^{-1} band for sample set B	68
Figure 4.5: Plot of second and third coefficients in the 975-875 cm^{-1} band for sample set B	69
Figure 4.6: Plot of the first two coefficients in the 1220-850 cm^{-1} band for sample set B	72
Figure 4.7: Plot of first and third coefficient in the 1220-850 cm^{-1} band for sample set B.....	73
Figure 4.8: Plot of second and third coefficients in 1220-850 cm^{-1} band for sample set B	74
Figure 4.9: Plot of first two coefficients by spot in 1220-850 cm^{-1} band for sample B1	77
Figure 4.10: Plot of first two coefficients by spot in 1800-1200 cm^{-1} band for sample B1	78
Figure 4.11: Plot of first two coefficients by spot in 1220-850 cm^{-1} band for sample B2	79

	Page
Figure 4.12: Plot of first two coefficients by spot in 1800-1200 cm^{-1} band for sample B2	80
Figure 4.13: Plot of first two coefficients by spot in 1220-850 cm^{-1} band for sample B2	81
Figure 4.14: Plot of first two coefficients by spot in 1800-1200 cm^{-1} band for sample B3	82
Figure 4.15: Plot of first two coefficients by spot in 1220-850 cm^{-1} band for sample B3	83
Figure 4.16: Plot of first two coefficients by spot in 1800-1200 cm^{-1} band for sample B3	84
Figure 4.17: Plot of first two coefficients by week in 1220-850 cm^{-1} band for sample B1	86
Figure 4.18: Plot of first two coefficients by week in 1800-1200 cm^{-1} band for sample B1	87
Figure 4.19: Plot of first two coefficients by week in 1220-850 cm^{-1} band for sample B2	88
Figure 4.20: Plot of first two coefficients by week in 1800-1200 cm^{-1} band for sample B2	89
Figure 4.21: Plot of first two coefficients by week in 1220-850 cm^{-1} band for sample B3	90
Figure 4.22: Plot of first and third coefficients by week in 1800-1200 cm^{-1} band for sample B3 ..	91
Figure 4.23: Plot of first two coefficients by week in 1220-850 cm^{-1} band for sample B4	92
Figure 4.24: Plot of first two coefficients by week in 1800-1200 cm^{-1} band for sample B4	93
Figure 4.25: Mean reflectance of the four samples in set A collected the first day	96
Figure 4.26: Plot of first two coefficients for A1 and A3 using the entire spectrum.....	97
Figure 4.27: Plot of first two coefficients for sample set A using entire spectrum.....	98
Figure 4.28: Plot of first two coefficients for A1 and A3 in the fingerprint region	100
Figure 4.29: Plot of first two coefficients for sample set A in the fingerprint region	101
Figure 4.30: Plot of second and third coefficients for sample set A in fingerprint region	103
Figure 4.31: Plot of first two coefficients with the classification rule with adjusted cost	104
Figure A.1: Mean reflectance of the gold reference standard with recalibration	112
Figure A.2: Mean subtraction of gold reference standard with recalibration	113

	Page
Figure A.3: Standard deviation for gold reference standard with recalibration.....	114
Figure A.4: Mean reflectance of gold reference standard without recalibration	115
Figure A.5: Mean subtraction of gold reference standard without recalibration.....	116
Figure A.6: Standard deviation for gold reference standard without regular recalibration.....	117
Figure B.1: Sample diagram for sample set A.....	118
Figure B.2: Sample diagram for sample set B.....	119
Figure D.1: Plot of first two coefficients in 1150-850 cm^{-1} band for sample set B.....	128
Figure D.2: Plot of first and third coefficients in 1150-850 cm^{-1} band for sample set B	129
Figure D.3: Plot of second and third coefficients in 1150-850 cm^{-1} band for sample set B	129
Figure D.4: Plot of first two coefficients in 1150-1050 cm^{-1} band for sample set B.....	130
Figure D.5: Plot of first and third coefficients in 1150-1050 cm^{-1} band for sample set B	130
Figure D.6: Plot of second and third coefficients in 1150-1050 cm^{-1} band for sample set B	131
Figure D.7: Plot of first two coefficients in 1200-800 cm^{-1} band for sample set B.....	131
Figure D.8: Plot of first and third coefficients in 1200-800 cm^{-1} band for sample set B	132
Figure D.9: Plot of second and third coefficients in 1200-800 cm^{-1} band for sample set B	132
Figure D.10: Plot of first two coefficients in 1800-800 cm^{-1} band for sample set B.....	133
Figure D.11: Plot of first and third coefficients in 1800-800 cm^{-1} band for sample set B	133
Figure D.12: Plot of second and third coefficients in 1800-800 cm^{-1} band for sample set B.....	134
Figure D.13: Plot of first two coefficients in 1800-1200 cm^{-1} band for sample set B.....	134
Figure D.14: Plot of first and third coefficients in 1800-1200 cm^{-1} band for sample set B	135
Figure D.15: Plot of second and third coefficients in 1800-1200 cm^{-1} band for sample set B	135
Figure D.16: Plot of first two coefficients in 800-1450 cm^{-1} band for sample set B.....	136

	Page
Figure D.17: Plot of first and third coefficients in 1800-1450 cm^{-1} band for sample set B	136
Figure D.18: Plot of second and third coefficients in 1800-1450 cm^{-1} band for sample set B	137
Figure D.19: Plot of first two coefficients in 1800-1650 cm^{-1} band for sample set B.....	137
Figure D.20: Plot of first and third coefficients in 1800-1650 cm^{-1} band for sample set B	138
Figure D.21: Plot of second and third coefficients in 1800-1650 cm^{-1} band for sample set B	138
Figure D.22: First two coefficients in 1800-800 minus 1500-1200 cm^{-1} band for sample set B .	139
Figure D.23: First and third coefficients in 1800-800 minus 1500-1200 cm^{-1} band for set B	139
Figure D.24: Second and third coefficients in 1800-800 minus 1500-1200 cm^{-1} band for set B.	140
Figure D.25: Plot of first and third coefficients by spot for B1 in 1220-850 cm^{-1} band.....	141
Figure D.26: Plot of second and third coefficients by spot for B1 in 1220-850 cm^{-1} band.....	141
Figure D.27: Plot of first and third coefficients by spot for B1 in the 1800-1200 cm^{-1} band	142
Figure D.28: Plot of second and third coefficients by spot for B1 in 1800-1200 cm^{-1} band	142
Figure D.29: Plot of first and third coefficients by spot for B2 in 1220-850 cm^{-1} band.....	143
Figure D.30: Plot of second and third coefficients by spot for B2 in 1220-850 cm^{-1} band.....	143
Figure D.31: Plot of first and third coefficients by spot for B2 in 1800-1200 cm^{-1} band.....	144
Figure D.32: Plot of second and third coefficients by spot for B2 in 1800-1200 cm^{-1} band	144
Figure D.33: Plot of first and third coefficients by spot for B3 in 1220-850 cm^{-1} band.....	145
Figure D.34: Plot of second and third coefficients by spot for B3 in 1220-850 cm^{-1} band.....	145
Figure D.35: Plot of first and third coefficients by spot for B3 in 1800-1200 cm^{-1} band.....	146
Figure D.36: Plot of second and third coefficients by spot for B3 in 1800-1200 cm^{-1} band	146
Figure D.37: Plot of first and third coefficients by spot for B4 in 1220-850 cm^{-1} band.....	147
Figure D.38: Plot of second and third coefficients by spot for B4 in 1220-850 cm^{-1} band.....	147

	Page
Figure D.39: Plot of first and third coefficients by spot for B4 in 1800-1200 cm^{-1} band.....	148
Figure D.40: Plot of second and third coefficients by spot for B4 in 1800-1200 cm^{-1} band	148
Figure D.41: Plot of first and third coefficients by week in 1220-850 cm^{-1} band for B1	149
Figure D.42: Plot of second and third coefficients by week in 1220-850 cm^{-1} band for B1	150
Figure D.43: Plot of first and third coefficients by week in 1800-1200 cm^{-1} band for B1	150
Figure D.44: Plot of second and third coefficients by week in 1800-1200 cm^{-1} band for B1.....	151
Figure D.45: Plot of first and third coefficients by week in 1220-850 cm^{-1} band for B2	151
Figure D.46: Plot of second and third coefficients by week in 1220-850 cm^{-1} band for B2	152
Figure D.47: Plot of first and third coefficients by week in 800-1200 cm^{-1} band for B2	152
Figure D.48: Plot of second and third coefficients by week in 1800-1200 cm^{-1} band for B2.....	153
Figure D.49: Plot of first and third coefficients by week in 1220-850 cm^{-1} band for B3	153
Figure D.50: Plot of second and third coefficients by week in 1220-850 cm^{-1} band for B3	154
Figure D.51: Plot of first and second coefficients by week in 1800-1200 cm^{-1} band for B3	154
Figure D.52: Plot of second and third coefficients by week in 1800-1200 cm^{-1} band for B3	155
Figure D.53: Plot of first and third coefficients by week in 1220-850 cm^{-1} band for B4	155
Figure D.54: Plot of second and third coefficients by week in 1220-850 cm^{-1} band for B4	156
Figure D.55: Plot of first and third coefficients by week in 1800-1200 cm^{-1} band for B4	156
Figure D.56: Plot of second and third coefficients by week in 1800-1200 cm^{-1} band for B4.....	157
Figure F.1: First two coefficients for set B in 1220-850 cm^{-1} band without normalization.....	162
Figure F.2: First two coefficients for set B in the 1220-850 cm^{-1} band with normalization	163
Figure F.3: Plot of percent of the data variance captured by each basis vector	165
Figure F.4: Plot of the first three basis vectors for sample set B in the 1220-850 cm^{-1} band	166

List of Tables

	Page
2.1. List of characteristic frequencies of some polymer functional groups	27
3.1. Sample naming convention and treatment conditions.....	38
4.1. Confusion matrix and error rates for the 975-875 cm ⁻¹ band.....	70
4.2. Confusion matrix and error rates for the 1220-850 cm ⁻¹ band	75
4.3. Confusion matrix and error rates for the classifier for sample set A.	98
4.4. Confusion matrix and error rates in the fingerprint region.	101
E.1. Confusion matrix and error rates for the 1150-850 cm ⁻¹ band	158
E.2. Confusion matrix and error rates for the 1150-1050 cm ⁻¹ band	158
E.3. Confusion matrix and error rates for the 1200-800 cm ⁻¹ band	159
E.4. Confusion matrix and error rates for the 1800-800 cm ⁻¹ band	159
E.5. Confusion matrix and error rates for the 1800-1200 cm ⁻¹ band	160
E.6. Confusion matrix and error rates for the 1800-1450 cm ⁻¹ band	160
E.7. Confusion matrix and error rates for the 1800-1650 cm ⁻¹ band.....	161
E.8. Confusion matrix and error rates for the 1800-800 minus 1500-1200 cm ⁻¹ band.....	161

INVESTIGATION OF THE POTENTIAL FOR FTIR AS A NONDESTRUCTIVE INSPECTION TECHNIQUE
FOR AIRCRAFT COATING DEGRADATION

I. Introduction

1.1. Background

Aircraft have long been coated to protect against damage, provide camouflage, and aesthetic purposes. One of the most important functions of a coating material is to protect against corrosion of the underlying panel. When the coating fails, moisture and air are able to penetrate to the interface between the coating and substrate where it reacts with both the coating and underlying panel[1], [2]. This reaction manifests as corrosion and weakens both the structural integrity of the panel as well as eroding the bond between the coating and substrate, ultimately disbonding the coating completely. Corrosion costs the USAF billions of dollars per year, making corrosion prevention and control a priority for the USAF and congress[3].

There are several nondestructive inspection techniques already employed by the USAF to detect surface corrosion, including visual, eddy current, magnetic particle, liquid penetrant, and thermography[4]. The primary limitation of each of these techniques is that corrosion must already be present, which means the coating has already failed and repair or replacement of the component is required. If the coating material itself could be characterized and the remaining service life predicted, costly repairs or replacement could be avoided.

1.2. Problem Statement

All of the inspection techniques currently employed by the USAF are capable of detecting corrosion. However, these tools can only tell the inspector whether there is or is not corrosion present. They are not capable of predicting when the coating will fail if it has not already. Furthermore, these methods require the use of chemicals, surface preparation, and clean up. In the case of thermography, the panel to be inspected must be removed from the aircraft.

The primary inspection method for coating failure is a visual inspection. Visual inspections are inexpensive and do not require extensive training or certification of the inspector. The inspector walks around and on the aircraft looking for visible indications of coating failure. These indications are typically cracking, wrinkling, blistering, and chipping. In extreme cases, large sections of coating may have fallen off the aircraft. By the time the coating has degraded to this extent, corrosion has already started to attack the underlying component.

There are laboratory characterization tools that are capable of characterizing the degradation present in the coating material. However, these tools are impractical due to both their destructive nature and the requirement that samples be removed from the aircraft and sent to the lab for evaluation. The USAF is in need of a field nondestructive inspection method that is capable of characterizing the current state of coating degradation and estimating the remaining service life of the coating.

1.3. Research Objectives and Hypotheses

The primary objective of this research effort is to investigate whether or not a handheld FTIR device is suitable as a nondestructive inspection tool that can be used in the field. A handheld FTIR device is both portable and nondestructive because the energy of IR radiation is enough to induce molecular vibration, but not enough to break chemical bonds, making it ideal for this application. The entire effort to establish a new inspection for the field is extensive and beyond the scope of this research. Additionally, there are other teams working to determine the root cause of the degradation, so it was not pursued here.

Polymers have several common failure mechanisms, but often it is a combination of many that lead to the eventual failure. In the case of aircraft coatings, exposure to heat, moisture, and UV radiation are the primary causes of degradation[5]–[8]. There are changes in the chemical composition and polymer chain structure associated with these degradation mechanisms that will be discussed in detail in the next chapter. These changes in composition and structure are molecular changes that should be detectable by FTIR spectroscopy.

1.4. Research Focus

The focus of this research is the use of Diffuse Reflectance Infrared Fourier Transform spectroscopy (DRIFTS) to characterize the state of degradation of polyurethane aircraft coatings. This is an initial effort to demonstrate proof of concept and that the technique has the ability to detect and classify degradation levels in the polyurethane coatings. The IR spectra collected on laboratory samples will be analyzed

using pattern recognition algorithms and statistical analysis to distinguish the states of increasing degradation from each other. As mentioned earlier, root cause analysis of the degradation and the establishment of a field inspection are not within the scope of this effort. However, should the results of this work be accepted as a valid approach to coating inspection, those efforts can be pursued using this approach. Additionally, once the spectra have been classified correctly, a correlation between the FTIR data collected on laboratory prepared samples and fielded samples from aircraft can be generated to estimate remaining life of the coating.

1.5. Methodology

The samples, equipment, and lab space utilized during this study were all supplied by AFRL/RX. The sample coating materials and layer thicknesses were representative of coating layers applied to fielded aircraft. The samples were placed in an autoclave under the same conditions, but for differing amounts of time, to generate the degradation levels.

The equipment used is commercially available and was previously purchased by AFRL/RXCA. This saved a lot of time and money during the early stages of the study because equipment did not have to be constructed or acquired. It also provided an opportunity to examine an actual handheld device that would likely be considered for acquisition if the USAF does pursue this avenue in the future.

The device was examined for its ability to collect accurate and reliable FTIR data. This included an analysis of the calibration interval used for data collection and a

comparison with a bench top system. It was determined that the handheld device was capable of producing quality data that could be relied upon for inspection purposes.

The experimental set up was rudimentary and minimally controlled. Samples were left on a desk in an office between collections and the samples were held up to the device aperture by hand. This was done intentionally to mimic uncontrolled field conditions since the purpose of the investigation was to determine whether or not a handheld FTIR device is suitable for a field inspection. Data collection was conducted over a six week period to allow for investigation into any potential time-dependent behavior in the material.

The FTIR spectra were analyzed using singular value decomposition (SVD) and the samples were classified using linear discriminant analysis (LDA). Both of these methods are discussed at length in the next chapter. SVD is commonly used as a pattern recognition technique, making it an ideal tool to search for a trend in the degradation levels of the samples. LDA is a simple data classification algorithm that made sample classification objective and quantitative rather than subjective based on qualitative analysis. LDA also provides the ability to predict which degradation level a new sample measurement falls into, which is the final goal of the study.

1.6. Assumptions and Limitations

The first assumption made during this study was that the coating materials used on the samples is the same material that is applied to fielded aircraft. This had to be assumed because the coating material composition is proprietary and an extensive compositional analysis to prove it was the same would have been too time-consuming.

It should be noted that even if the sample materials are not exactly the same as the fielded materials, the research goals could still be met. As long as the base material is polyurethane and the rest of the ingredients present, the proof of concept of being able to detect different levels of coating degradation is still valid.

The other assumption made is that the accelerated aging applied to the samples leads to the same degradation seen in the field. As stated previously, there is another team at AFRL/RX working the root cause of the degradation. Part of that effort required the lab to recreate the same degradation seen in the field for the purposes of determining what the root cause is. The aging treatment used on the samples in this research effort is one that the root cause team determined best resembles the visual indications of degradation seen in the field.

There were several limitations that needed to be considered when examining this work. The primary limitation is the number of samples. There were only eight total samples generated for this study due to budget constraints. This limitation prevented more comprehensive studies using destructive techniques in concert with DRIFTs to reinforce the conclusions drawn from the data. The limited sample set also prevents definitive conclusions to be drawn about the ability of DRIFTs to accurately estimate the remaining service life of the coating. However, the objective of this research is to determine the viability of pursuing DRIFTs further and the number of samples provided was enough to make that determination. Additionally, real aircraft panels were not made available for study due to cost and classification concerns. Examination of panels removed from fielded aircraft would allow for an accurate correlation between the data

collected on laboratory samples and fielded samples. Without that information, the conclusions reached using the laboratory samples rely on extrapolation to what might be expected in the field.

The final limitation is that only one handheld FTIR device was used to collect data. Ideally, several devices from several manufacturers would be used to eliminate any defects or shortcomings of the device from the data.

1.7. Implications

As stated earlier, corrosion is a very expensive problem for the USAF. Inspection programs are designed to detect whether or not corrosion is present and to what extent. A practical, nondestructive inspection tool capable of characterizing the state of degradation locally and estimating remaining life will save the USAF money, time, and operational capabilities. Knowing if the protective coating has failed or an estimate of when it will fail will better guide the structural integrity program inspections and provide more tools in the corrosion prevention toolbox. Furthermore, rather than stripping and recoating an entire aircraft because one panel has degraded, maintainers will be able to quickly characterize each panel and determine the extent of the degradation. Decisions can be made about whether individual panels or entire aircraft need to be recoated. They will also be able to develop a more efficient depot flow plan that prioritizes aircraft with the most urgent need, while laying out a future schedule for aircraft that will be needing resurfacing.

II. Theory

2.1. Polyurethane Degradation

Polyurethane is a complex material and can be synthesized in many ways for use as a protective coating[9]. The synthesis chemistry and curing process greatly affect the material properties and susceptibility to degradation mechanisms[9]. Generally, all polymer materials are susceptible to the same degradation mechanisms that include photo-degradation upon exposure to UV/Vis radiation in the presence of water and oxygen, temperature, and physical aging[5]–[8], [10]–[14].

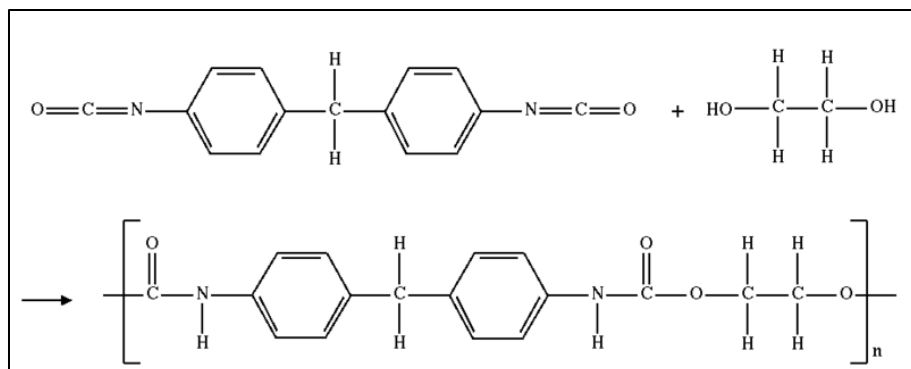


Figure 2.1: Schematic diagram of polyurethane molecular structure.

Figure 2.1 is a schematic diagram of the molecular structure of polyurethane. With the exception of physical aging, all the degradation mechanisms that affect polyurethane alter the molecular weight of the chains. This occurs through the production and subsequent consumption of free radical groups.

2.1.1. Ultraviolet (UV) Exposure.

Exposure to UV radiation in the presence of water and oxygen is a critical contributor to polymer degradation[5], [7], [8], [11], [13], [14]. The photo-generation of oxidants such as hydro-peroxides, carbonyl and peroxide groups, ketones, and aldehydes in polyurethanes in the presence of water or oxygen has been investigated and is well documented[5], [7], [8], [11], [13], [14].

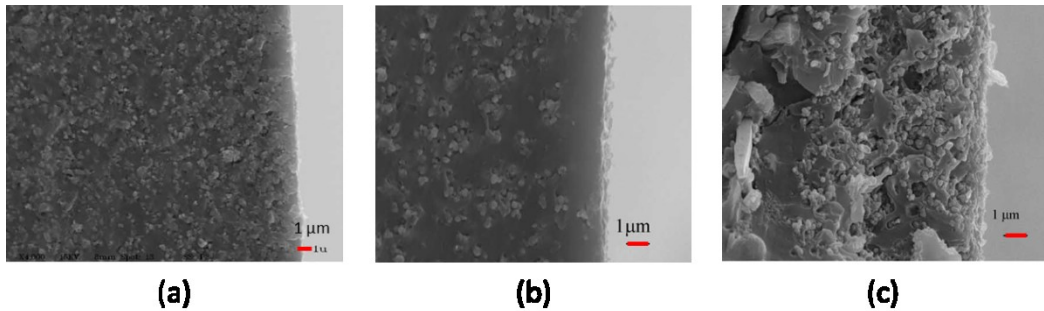


Figure 2.2: Cross-section micrographs of a polyurethane aircraft coating: a) coating before exposure; b) after 27 weeks of alternating QUV/prohesion chamber exposure; c) after 24 weeks of QUV exposure. The results of this study performed by Yang, Tallman, et. al. showed that UV exposure is more damaging than salt fog to polyurethane coatings[6]. Reprinted with permission from Elsevier.

Figure 2.2 is a scanning electron microscope (SEM) cross-sectional micrograph of a polyurethane film after QUV and alternating QUV and salt fog treatments. A QUV chamber simulates natural weather environments by exposing the sample to moisture and UV radiation from fluorescent lamps. Figure 2.2(a) is the film before exposure and shows that there are no cracks or voids in the material. Figure 2.2(b) is a micrograph taken after 27 weeks of alternating QUV and salt fog exposure. There are still no cracks or voids evident in the film. Figure 2.2(c) is a micrograph taken after 24 weeks of QUV

exposure and the cracks and voids are clearly visible. This demonstrates how damaging exposure to UV radiation in the presence of moisture is to polymer materials.

2.1.2. Exposure to Moisture.

Upon exposure to water, such as humidity or condensation, water penetrates into the coating material through several migration methods including diffusion through the polymer matrix, capillary forces in cracks or the interface between substrate and coating, or through defects in the coating surface[7]. Figure 2.3 contains tapping mode atomic force microscope (AFM) images of the surface of a polyurethane coating material after a Harrison's solution (saltwater) treatment. Figure 2.3(a) illustrates how large ridges and blisters form on the surface of the coating as a result of water penetrating the material. The ridges are known as filiforms and lead to filiform corrosion which is commonly seen in coating materials. Figure 2.3(b) is an image zoomed in on what appears to be an unaffected region of the coating in figure 2.3(a). It reveals that micro-scale threadlike filiforms are forming on the surface.

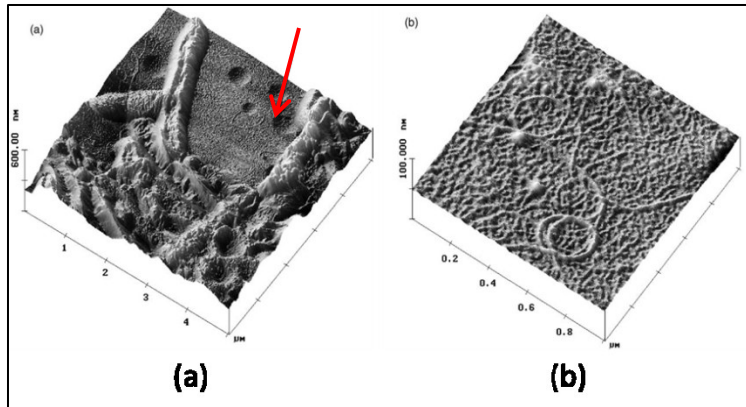


Figure 2.3: Tapping mode AFM images of filiform corrosion forming in a polyurethane coating after exposure to Harrison's solution (3.5 g/l $(\text{NH}_4)_2\text{SO}_4$ + 0.5 g/l NaCl, pH=5). Image (b) is a magnification of the seemingly flat region in (a) indicated by the red arrow. Yang, Tallman, et. al. reported that nanoscale thread-like structures form quickly on the surface of a polyurethane coating when exposed to water. Eventually, filiform structures form, as shown in (b) and cracks open[7]. Reprinted with permission from Elsevier.

There are several chemical explanations for this behavior proposed by various research groups. Kamal and Saxon hypothesized that there are three primary effects of polymer exposure to water[15]. The first is a hydrolysis of the ester or amide bonds, the second is a breaking of the interfacial bonds with the substrate leading to de-adhesion, and the third is the generation of free radicals when combined with UV exposure mentioned earlier. Yang, Tallman, *et al.* also proposed the formation of osmotic cells with soluble impurities leading to surface damage [7]. It is understood in the polymer community that aside from UV exposure, moisture is the most critical source of degradation. However, as mentioned above, other factors such as temperature, also play a role in polymer degradation.

2.1.3. Physical Aging.

Physical aging is the spontaneous relaxation of a coating material in its glassy state as a result of being in a non-equilibrium state [11]. Physical aging corresponds to a change in volume, enthalpy, and entropy in the material and is correlated to the temperature at which the material ages. The rate of physical aging increases as the temperature approaches the glass transition temperature, T_g , of the material; however, the magnitude of change decreases. As a simplistic analogy, this can be envisioned as a ball rolling down a hill. As the ball nears the bottom of the hill, it is traveling much faster than it was at the top of the hill. However, as the bottom of the hill begins to flatten out, the change in elevation of the ball is much less than when it was near the top. Nearly all material properties are affected by physical aging including mechanical, thermal, electrical, and optical. Unlike chemical degradation, physical aging can be reversed in some polymers by heating the material above its T_g for sufficient time. For most polymer materials, the effect of physical aging is negligible during the life of the part; however, thermosetting organic coatings are cured at high temperatures and contain a relatively high level of free volume. The reduction in free volume due to physical aging leads to changes in mechanical, electrical and thermal properties that affect the coating performance. Additionally, and perhaps more evidently, the reduction in free volume leads to a contraction of the material and a corresponding increase in density[11], [14]. This allows for neighboring polymer chains to come into closer proximity and affect the interactions between them, even if only slightly. It is not expected that physical aging would contribute much to the degradation of coating

samples over the course of this research when compared to the expected chemical effects of accelerated aging. It was included in the discussion about degradation mechanisms because the accelerated aging treatment used to prepare the samples included significantly elevating the temperature of the samples.

2.1.4. Accelerated Aging.

All of the studies about the various degradation mechanisms in polymers have contributed to the understanding and development of faster and more reliable accelerated aging tests. This is important because manufacturers are constantly developing polymers with longer and longer lifespans, and the use of primitive degradation tests would add years to the development. For decades, the standard exposure tests were the Florida and Arizona tests because of the differences in the amount of daylight and humidity. Samples were simply left out in the elements in for standardized lengths of time. Over the past two decades, researchers have relied on machines such as QUV chambers, prohesion chambers, and autoclaves to accelerate the aging process in a laboratory environment[5], [16]. The use of accelerated aging tests shortens the development, while allowing the testing to be conducted in a more controlled and reliable environment. There are two drawbacks to using the accelerated aging techniques that must be considered. As a general rule, it is understood that there is an inverse relationship between the intensity of the accelerated aging and the correlation to natural exposure[16]. This prevents any real predictions about service life from being made from these tests. However, they do allow a direct comparison between materials and their degradation response to the treatment. The other primary

drawback is that the polymer sample under test will generally not respond to the treatment uniformly[16]. This means large samples will have wide-ranging degradation levels across the sample. It is important to keep these factors in mind, as well as the intended environment for the material, when choosing an accelerated aging treatment. Knowledge about the material response to the accelerated aging treatment, whether the degradation is physical or chemical in nature, is useful in pursuing a characterization technique capable of detecting it. An appropriate method is one capable of detecting the molecular changes taking place while not damaging the material.

2.2. Fourier Transform Infrared (FTIR) Spectroscopy

FTIR spectroscopy has become, arguably, the most widely used vibrational spectroscopic technique for materials characterization[17]. Its advantages over other techniques include the low relative cost and size of the equipment, speed of data acquisition, and flexibility in its application depending the sample phase and material class. Many different applications of FTIR have been developed to accommodate the various types of material that spectroscopists encounter in the lab, but fall into two basic categories: transmission and reflection. Transmission data is collected by passing infrared (IR) radiation through a sample and detecting it on the opposite side of the sample from the source, as shown in figure 2.4(a). Reflection data is a one-sided measurement where the detector and source are on the same side of the sample, as shown in figure 2.4(b).

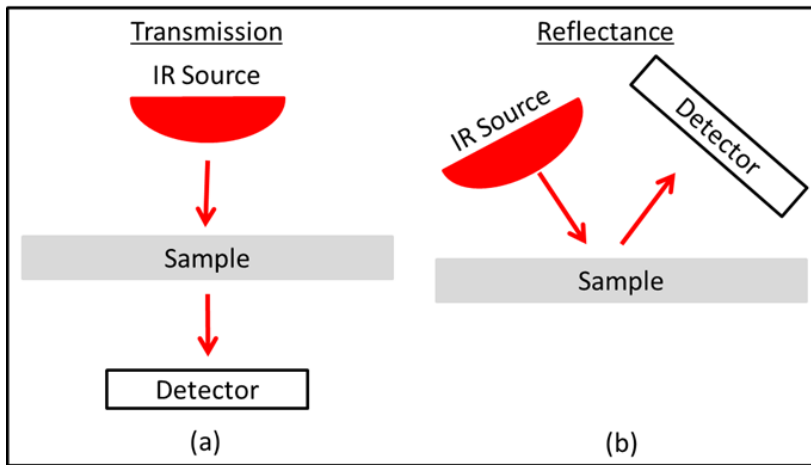


Figure 2.4: A schematic of transmission and reflectance FTIR measurements. Figure 2.4(a) demonstrates how transmission FTIR is a two-sided measurement with the source and detector on opposite sides of the sample. Figure 2.4(b) shows how reflectance FTIR is a one-sided measurement with the source and detector on the same side of the sample.

The sample to be measured is the determining factor in which technique to be used. An understanding of the fundamental theory of FTIR and the different techniques is instrumental to successful characterization of a sample.

2.2.1. Vibrational Energies of Molecules.

Solid state physics and quantum mechanics provide the basic theory for vibrational spectroscopy. The sizes of the different constituents of a material, from the electrons up through large chain molecules, vibrate at different frequencies. The smaller the component is (i.e. electrons), the higher the resonant frequency of vibration. It is understood that electromagnetic radiation interacts with different particles depending upon the frequency of the radiation as depicted in Figure 2.5.

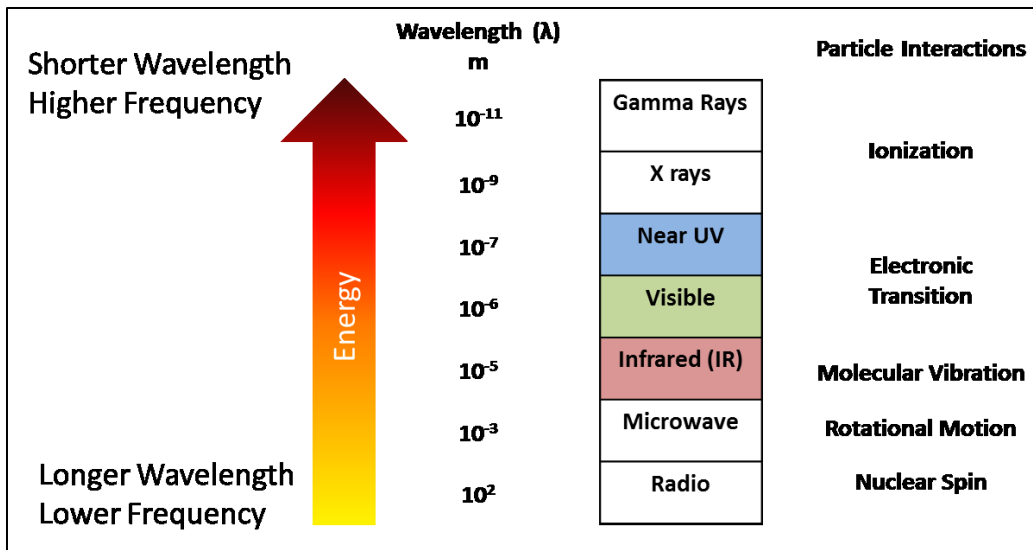


Figure 2.5: Diagram of the interactions between atomic and subatomic particles with electromagnetic radiation. The energies of the bands of the spectrum correspond to the energies associated with the different particle responses.

The very high frequency, or short wavelength, portion of the spectrum interacts with the smallest particles. The low frequency, or long wavelength, portion of the electromagnetic spectrum interacts with larger particles. A molecule containing n atoms has $3n$ degrees of freedom in three-dimensional space as well as three degrees of freedom to describe translational motion and another three degrees of freedom to describe rotational motion. Therefore, there are $3n-6$ degrees of freedom that correspond to the fundamental vibrational modes for a nonlinear molecule in free space. The standard model for this interaction is to represent the chemical bond in a diatomic molecule as a harmonic oscillator composed of a massless spring between two nuclei shown in Figure 2.6.

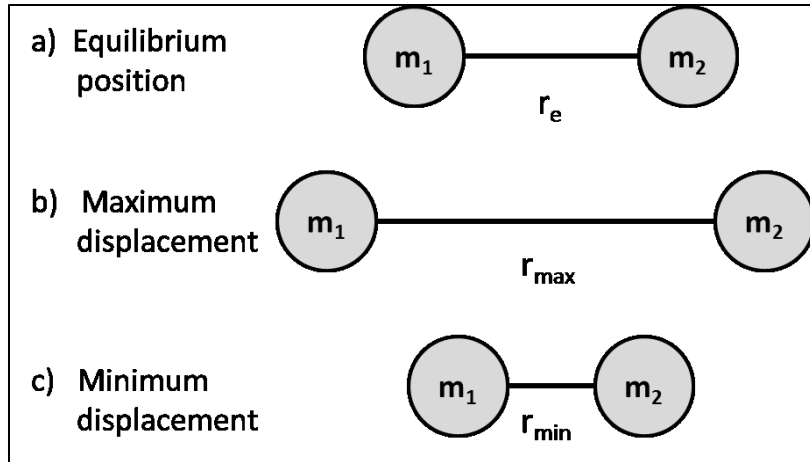


Figure 2.6: Massless spring model used to represent the harmonic oscillations of atoms in a diatomic molecule. The spring model is a useful estimation of the bond energy in a molecule that can be found to identify absorbance peaks in FTIR spectra.

Figure 2.6(a) represents the equilibrium position of the molecule and Figures 2.6(b) and (c) represent the maximum and minimum displacements of the molecule, respectively, from its equilibrium position. The force due to linear elastic deformation is found using equation 2.1.

$$F = -K(\Delta r) = -K(r - r_e) \quad (2.1)$$

In equation 2.1, K is the spring constant and r is the displacement from equilibrium.

From equation 2.1, the potential energy of a harmonic vibration can be found using equation 2.2.

$$E_{vib} = \frac{1}{2}K(\Delta r)^2 = \frac{1}{2}K(r - r_e)^2 \quad (2.2)$$

Equation 2.2 presents the potential energy as a continuous parabolic harmonic curve, when quantum mechanics requires that the vibrational energies be quantized.

$$E_{vib} = h\nu_{vib} \left(\nu + \frac{1}{2} \right) \quad \nu = 0, 1, 2, \dots \quad (2.3)$$

Equation 2.3 is the quantized energy of vibration for a diatomic molecule, where h is Planck's constant, v is the vibrational quantum number, and ν_{vib} is the vibrational frequency of the molecule. When the energy of the incident radiation is equal to the vibrational energy of the molecule, it is absorbed. Many molecules have a center of positive charge and a center of negative charge separated by a distance, l . The dipole moment, μ , of the molecule is defined as the distance between the charge centers, l , multiplied by the magnitude of the charge, e :

$$\mu = el \quad (2.4)$$

If the excited vibrational mode alters the dipole moment of the molecule, it is said to be IR active:

$$\left(\frac{\delta\mu}{\delta q}\right)_{q=0} \neq 0 \quad (2.5)$$

where q is the distance from the molecule's equilibrium position, represented as Δr in equation 2.2 above[17]. A common molecule used to visualize IR active and non-IR active vibrational modes is CO_2 because it is a linear molecule that has stretching and bending modes. Figure 2.7 is a schematic of the stretching and bending modes seen in CO_2 .

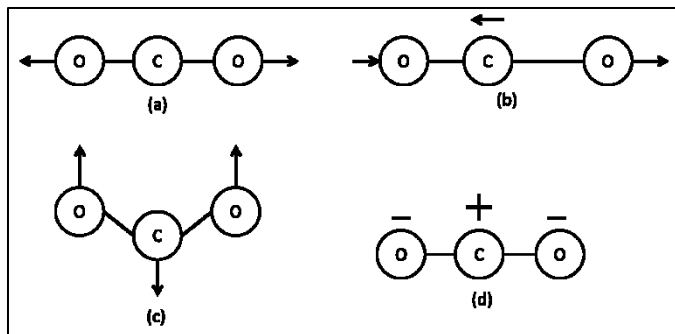


Figure 2.7: A schematic of the stretching and bending vibrational modes of CO_2 . Figure 2.7(a) is a symmetrical stretching from the central C atom, which is not IR active; (b) is the asymmetric stretching mode that is IR active; (c) and (d) are the in-plane and out-of-plane bending modes, respectively, and are both IR active.

Figure 2.7 represents the four normal vibrational modes of the CO_2 molecule. Figure 2.7(a) is the symmetrical stretching mode. It is not IR active because it does not change the dipole moment. Figure 2.7(b) is an IR active mode because it is asymmetric, therefore changing the dipole moment. Figures 2.7(c) and 2.7(d) are the in-plane and out-of-plane bending modes, which are both IR active. IR spectroscopy is a popular choice for characterizing organic polymers because they are composed of molecules that have resonant frequencies in the mid-IR range of the electromagnetic spectrum ($4000\text{-}400\text{ cm}^{-1}$ or $2.5\text{-}25\text{ }\mu\text{m}$)[18]. The large, repeating, chain molecules in polymers are typically composed of smaller hydrocarbon molecules, such as carbonyls and carboxylic acid groups, with distinct vibrational frequencies. When these frequencies are known, IR spectroscopy can be used as a tool for identifying the composition and structure of the material under examination.

2.2.2. Interferograms and the Fourier Transform.

Using a modern-day FTIR spectrometer connected to a computer, it is easy to forget that the spectrum displayed on the computer screen is not what is actually measured by the device. What is actually measured is the intensity of detected light as a function of path-length difference between two beams of light. When the optical path-length difference, δ , is equal to an integer multiple of the wavelength, $n\lambda$, the interference between the two beams is entirely constructive. When $\delta=(1/2 + n)\lambda$, the interference is entirely destructive. A plot of detected light intensity as a function of path-length difference is called an interferogram. During the early years of IR spectroscopy, researchers had to scan through the wavelengths of interest one wavelength at a time using a monochromator. The advent of the interferometer combined with the Fourier Transform led to the invention of the FTIR spectrometer, which allows the sampling of all wavelengths simultaneously and the digital conversion of an interferogram into an absorbance or reflectance spectrum. The most common interferometer is the Michelson Interferometer, a schematic of which is shown in figure 2.8. The IR radiation from the source is focused as a beam into the interferometer where it is split into two beams of equal intensity by a beam splitter. One of the beams split off by the splitter is reflected back to the beam splitter from a fixed mirror and the other from a moving mirror. This generates the path-length difference between the two beams. The detector transmits the intensity of the incident radiation that passes through the sample back to a computer, which creates the interferogram.

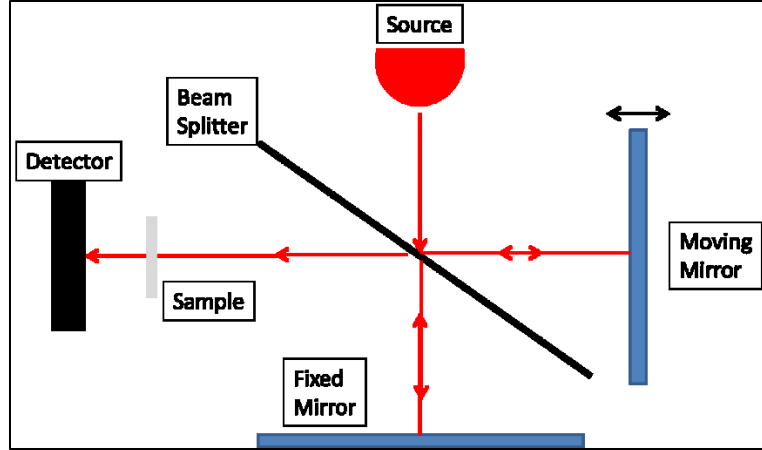


Figure 2.8: Schematic diagram of a Michelson Interferometer. The IR beam generated by the source is comprised of all sampling wavelengths. The beam is split into two beams by the beam splitter. The optical path-length difference is generated between the two beams by moving one mirror and holding the other in a fixed position.

Once the interferogram is generated, it is digitally converted into the more familiar IR spectrum that is displayed on the computer screen. This conversion is done using the Fourier Transform[17]:

$$F(\omega) = \frac{1}{\sqrt{2\pi}} \int_{-\infty}^{\infty} f(t) e^{-i\omega t} dt \quad (2.6)$$

This operation converts the intensity as a function of time, $f(t)$, generated using the velocity of the moving mirror, into intensity as a function of frequency, $F(\omega)$.

Fortunately, FTIR spectrometers come equipped with an interferometer and the software that executes the Fourier Transform. This makes taking FTIR measurements relatively fast and straightforward.

2.2.3. Advantages of FTIR.

As mentioned earlier, there are many advantages to using IR spectroscopy for materials characterization. The primary advantage is the relatively short amount of time required to collect data on a sample. Because the interferometer operates over the entire sampling wavelength range, a spectrum can be collected in seconds or minutes depending on the spectral resolution of the device. This reduction in time of FTIR measurements compared to dispersive, monochromatic spectrometers is called the Felgett advantage[19]. Furthermore, computers are able to conduct the Fourier Transform from intensity versus optical path difference to intensity versus wavenumber of the interferogram instantly. Another advantage to using FTIR is derived from the fact that they utilize an interferometer rather than dispersive or filtering slits as with dispersive spectrometers. This is called the Jacquinot advantage, or throughput advantage[19]. This conserves energy in the beam incident on the sample, thus allowing for measurements using energy-limited methods. Another advantage of modern FTIR spectrometers is that the software that communicates with the device is often preloaded with a database of known materials spectra. This makes identification of unknown samples relatively quick and easy if the sample is made of a material that is in the database. If the material is unique or proprietary, chances are high that it will not be in the database. Finally, as mentioned earlier, the flexibility of FTIR and how it can be applied is perhaps its greatest advantage. FTIR can be used to characterize solids, liquids, and gases using transmission or one of the many reflectance techniques[17]–[20]. This allows a wide range of organic, inorganic, and biological materials and sample

configurations to be characterized with IR spectroscopy. For all the advantages of FTIR, it should be noted that there are also limitations that must be considered when selecting the appropriate method.

2.2.4. Limitations of FTIR.

There are several limitations to using FTIR, but many can be overcome by either proper sample preparation or selecting the appropriate measurement technique. For example, many metals are highly reflective in the IR region of the spectrum. This makes FTIR a poor choice as a characterization technique because none of the energy of the incident radiation is absorbed. However, the reflective nature of metals in the IR region makes them good candidates as IR mirrors and calibration references, as discussed in Chapter 3. Solid samples prepared for transmission FTIR must be thin enough to allow the IR beam to pass through while also being thick enough to contain enough material to absorb the energy corresponding to the molecular bonds in the material. This problem can often be avoided by using one of the many reflectance measurement techniques, such as diffuse or specular reflectance. As discussed later in this chapter, reflectance measurements are unable to provide much of the quantitative information about the material that transmission measurements can. Additionally, many molecular bonds have energies that overlap similar bonds in complex materials such as polymers[17], [18]. This can make identification of an unknown material difficult or impossible. Other phenomena that complicate spectrum analysis are the existence of overtones (integer multiples of characteristic frequencies), coupling of fundamental modes, and the coupling of overtones with fundamental frequencies[17], [19].

2.2.5. Transmission FTIR.

Transmission FTIR is the standard IR spectrum collection technique because it has a high signal-to-noise ratio and it allows the direct interpretation of the spectra to determine absorbance peak locations [17], [18], [21], [22]. Transmission measurements are also consistent from measurement to measurement when compared to reflectance measurements, which make it the preferred choice for laboratory work. However, extensive sample preparation is often necessary to acquire transmission spectra. Solid samples must be reduced to powders or thin films less than 20 μm thick to allow transmission through the sample, but not less than 1 μm or the absorption will be too weak to detect[19]. These limitations make transmission FTIR a poor choice as a non-destructive inspection tool for aircraft coatings.

2.2.6. Reflectance FTIR.

Reflectance FTIR spectroscopy is useful for samples that are too thick, too large or the geometry of the sample is not conducive to transmission measurements. Even if a sample is transparent to IR radiation, a sample that is too thick will absorb all of the incident radiation, eliminating the ability to conduct transmittance measurements. In these instances, reflectance measurements become very useful. There are many techniques for collecting reflectance FTIR measurements, but the two primarily used for bulk samples are diffuse and specular. Unlike transmission measurements, reflection measurements are often difficult to interpret because of variability due to scatter from the non-uniform surface[23]. This is an important consideration when analyzing reflection FTIR spectra.

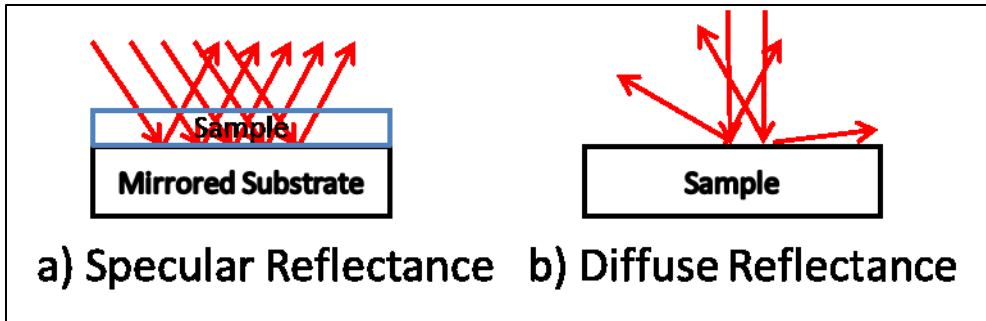


Figure 2.9: Schematic diagrams of specular and diffuse reflectance. Specular reflectance FTIR is used on very smooth surfaces or on thin films applied to mirrored substrates. Diffuse reflectance is used on powder samples or when the surface of the sample is rough.

Specular reflectance is used on smooth, reflective surfaces or for thin films applied to mirrored substrates as depicted in Fig 2.9(a). In the case of a sample with a smooth, mirror-like surface, specular reflectance will provide reflection data on the surface of the sample. For thin films ($<10 \mu\text{m}$) on a mirrored substrate, specular reflectance will provide reflection-absorption data. In specular reflectance, the reflected angle of the IR beam is the same as the incident angle as shown in Figure 2.9(a).

Diffuse reflectance is used on rough surfaces or powder samples. The incident beam is scattered from the surface and reflects at all angles as depicted in Figure 2.9(b). Diffuse reflectance is often referred to as Diffuse Reflectance Infrared Fourier Transform spectroscopy (DRIFTS) and has become a popular tool for the characterization of soil samples and polymer surfaces[24], [25]. The primary advantage of DRIFTS over transmittance or specular reflection as a characterization technique is that there is no sample preparation required for *in situ* measurements. The primary disadvantage is its inability to penetrate beyond the surface of the sample.

2.3. IR Spectrum Analysis

There are many ways to analyze experimental spectra depending on the purpose for collecting the data[22]. The first question the experimenter must ask when analyzing the spectrum is “what is the end result of my analysis going to be used for?” The answer to this question ranges from identifying a completely unknown sample to characterizing a completely known sample for the purposes of quality control[22]. The analysis approach and subsequent interpretation will depend on the method used to collect the spectra and the purpose for collecting it.

2.3.1. Spectra comparison.

The majority of the literature about IR spectroscopy discusses the principles of comparing FTIR spectra of samples to each other or to reference spectra in databases[17], [18], [21], [22]. Spectrum comparison involves identifying the precise location of absorbance peaks in the experimental spectrum and attributing a corresponding molecular vibration to it. If an experiment is intended to identify a particular material, the experimental spectrum is compared to a database of known material spectra. As mentioned earlier, this can be difficult or impossible when the material being identified is not in any databases.

There are two important regions of the IR spectrum of an organic polymer. The first region is called the functional region. Depending on the source, the functional region is located in the $4000-1500\text{ cm}^{-1}$ (2.5-6.7 μm) to $4000-1300\text{ cm}^{-1}$ (2.5-7.7 μm) range of the IR spectrum. The absorption bands seen in this region are typically due to stretching vibrations from single-, double-, and triple-bonded molecules. It is called the

functional region because it allows for the identification of functional groups present in the material. Table 2.1 contains a list of characteristic frequencies for common molecules found in polymer materials.

Table 2.1: List of characteristic frequencies for some functional groups found in polymers[18].

Functional Group	Characteristic Frequency (cm ⁻¹)
Alkanes	
ν -CH	2950-2850
δ -CH	1465-1380
Alkene	
ν -CH	>3000
Aromatic Rings	
In-plane bending	1225-950
Out-of-plane bending/ring puckering	<900
Hydroxyl	
ν -OH	3300
Ether	1250
Carbonyl	1900-1500
Triple Bonds	2300-2000
C≡C stretching	2140-2100
C≡N stretching	2260-2200
Double Bonds	1900-1500
Single Bonds	1300-800
Amides	
Primary – CONH ₂	1690
Secondary – CONH	1700

Each functional group has an absorption peak due to stretching at a characteristic wavelength, but some of them overlap. It is obvious from looking at characteristic frequencies in table 2.1 that many of the functional groups share the same values or can be found in ranges of values, making identification of polymers a difficult task. Also complicating the interpretation of an IR spectrum for polymers is the fact that hydrogen bonding significantly influences the peak shape and intensity[21]. Fortunately, there is

another region of the spectrum that, when combined with the peak locations in the functional region, makes polymer identification a little easier.

The other region of particular importance in an IR spectrum is the fingerprint region. As with the functional region, the precise location of the fingerprint region varies depending on the source, but is generally considered to begin where the functional region ends ($1500-1300\text{ cm}^{-1}$) and ends around $910-600\text{ cm}^{-1}$ (11-16.7 μm)[17], [21]. The fingerprint region is aptly named because it contains absorbance peaks arising from the complex interactions of molecules in the material and is unique to the material being examined. Molecular vibrations seen in this region include wagging, twisting, scissoring, and rocking as well as interactions between the functional groups[17]. Some texts refer to the $900-650\text{ cm}^{-1}$ region as the aromatic region because it is the region where the absorbance peaks due to out-of-plane aromatic bending occur[21]. The fingerprint region is very useful when characterizing polymers because they contain many of the same functional groups. For this reason, many polymer spectra will look very similar in the functional region, but will have a unique fingerprint region.

2.3.2. Pattern Recognition.

When the intended purpose for using FTIR to characterize a material is not for identification, but rather for distinguishing between similar materials, pattern recognition techniques can be useful. Singular value decomposition (SVD) is commonly applied to facial recognition, data reduction, and quality control[26], [27]. The strength of SVD is its ability to reduce the dimensionality of a data set and reveal the true

dynamics of a system while simultaneously minimizing noise and redundancy. The intention of applying SVD is to reveal whether or not the experimental data can be re-expressed onto a new basis that is a linear combination of the original basis. In other words, is there another basis that the original data set can be projected onto that will reduce noise and redundancy and reveal a previously hidden relationship in the data? As an aside, principal component analysis (PCA) is a common SVD technique applied to experimental data and the terms PCA and SVD are often used interchangeably. It should be noted that SVD is the more general approach while PCA is a specific SVD method. In order to apply SVD to experimental data, there are some assumptions that must be made. The primary assumption is linearity because SVD asks whether or not the data can be re-expressed onto a new basis, which requires linearity in the data. While the physics and chemistry of FTIR spectroscopy and polymer degradation are complex and nonlinear phenomena, local linear approximations within the system are reasonable and allow for the application of SVD to the data[28]. The second assumption is that the probability distribution of the data is Gaussian. This assumption allows the mean and variance to completely describe the data set. The Central Limit Theorem postulates that most real data sets are normally distributed, so this assumption is valid for most applications. The third assumption is that the singular values corresponding to eigenfunctions with large variances represent interesting dynamics within the system while those with lower variances represent noise. An implied assumption within that statement is that the data has a high signal-to-noise ratio. Finally, the fourth assumption that SVD makes is that the eigenfunctions, or basis vectors, are orthogonal.

This assumption permits linear algebra decomposition techniques to be applied to the data.

Given the assumptions described above are true for the data set, the process of performing the singular value decomposition is straightforward. Let D be the $n \times m$ data matrix, where each row represents a measurement and each column contains the measurement values for the given measurement:

$$D = \begin{bmatrix} D_{11} & \cdots & D_{1m} \\ \vdots & \ddots & \vdots \\ D_{n1} & \cdots & D_{nm} \end{bmatrix} \quad (2.7)$$

In the case of reflectance IR data, each row is a frequency or wavelength sampled and each column contains the measured reflectance values for that frequency or wavelength. From linear algebra, the eigenvalues and corresponding eigenvectors of the square matrix, $D^T D$, can be calculated for any $m \times m$ matrix using equation 2.8.

$$(D^T D) \hat{e}_i = \lambda_i \hat{e}_i \quad (2.8)$$

In equation 2.8, \hat{e}_i is a set of orthonormal $m \times 1$ eigenvectors and λ_i is the set of associated eigenvalues for the matrix $D^T D$. The singular values, s_i , for the matrix D are $s_i \equiv \sqrt{\lambda_i}$ and are positive real numbers. If \hat{u}_i is the set of orthonormal $n \times 1$ vectors defined by $\hat{u}_i \equiv \frac{1}{s_i} D \hat{e}_i$, then equation 2.8 can be restated as equation 2.9.

$$D \hat{e}_i = s_i \hat{u}_i \quad (2.9)$$

The set of eigenvectors, \hat{e}_i , and the set of vectors, \hat{u}_i , are the new bases for the data. If all of the eigenvectors are put into a matrix, E , all the \hat{u} vectors put into a matrix, U , and all the singular values put on the diagonal of matrix, Σ , in descending order, then

equation 2.9 can be rewritten as equation 2.10, and then rearranged to form equation 2.11.

$$DE = U\Sigma \quad (2.10)$$

$$D=U\Sigma E^T \quad (2.11)$$

Equation 2.11 is the fundamental singular value decomposition equation. In this representation, the columns of U and the rows of E^T contain the unique and orthonormal eigenfunctions, or basis vectors, of D . Once the basis vectors have been calculated using SVD, the goal is to determine a linear combination of variables that best reproduces the original data as shown in equation 2.12.

$$D = \sum_{i=1}^{\infty} a_i \Psi_i \quad (2.12)$$

The coefficients, a_i , are weighted by their importance in projecting the data onto the new basis composed of the basis vectors in U or E^T . The variables, Ψ_i , are the orthonormal eigenvectors of D . The Kronecker delta for the inner product of two vectors can be applied to determine the coefficients because the basis vectors are orthonormal:

$$\delta_{ij} = \begin{cases} 0 & \text{if } i \neq j \\ 1 & \text{if } i = j \end{cases} \Rightarrow \vec{a} \cdot \vec{b} = \sum_{ij} \vec{a}_i \delta_{ij} \vec{b}_j \quad (2.13)$$

Once the coefficients have been determined, they are plotted against each other to reveal any potential patterns that might exist in the data. Since one of the objectives in this work is sample classification, any groups that emerge in the SVD coefficients must be classified in a statistically significant manner. That is where a classification technique such as linear discriminant analysis (LDA) is useful.

2.3.3. Discriminant Analysis.

Discriminant analysis is a statistical approach to data classification first developed by Sir Ronald A. Fisher and explained in his paper pertaining to classifying which species of Iris a flower belonged to using petal and sepal measurements[29]. Since its introduction in 1936, it has been expounded upon and applied to data classification problems in many fields of study including taxonomy, biology, pattern recognition, and signal processing. Commonly, either PCA/SVD or discriminant analysis is used independently to classify data [20], [26], [30]. PCA or SVD are more commonly used when all the variables are quantitative and LDA is more appropriate when the dependent variable is categorical (e.g. type of Iris) and the independent variables are quantitative. However, if the principal components show separation or clustering, discriminant analysis can be applied to the principal components to improve classification accuracy [31].

There are many types of discriminant analysis that have been derived from Fisher's initial work, but the most common is Linear Discriminant Analysis (LDA). LDA is just Fisher's original classification method and can be applied to two or more classes. When more than two classes are involved, it is called Multivariate Discriminant Analysis (MDA). There are several key assumptions that are made when applying linear discriminant analysis. First, there is assumed to be a linear relationship between the dependent and independent variables. Second, the data is multivariate normally distributed. In other words, all the independent variables can be modeled by a Gaussian distribution. Finally, the variance-covariance matrices for each group must be equal.

The first step in applying LDA to a dataset is collecting truth data for generating the discriminant function(s). In this phase, the group that each observation belongs to is known *a priori*. It's important that each observation be assigned to appropriate group and that all data is gathered independently.

Step two is to determine the prior probability that an observation belongs to a group. There are three choices that can be made. The first is equal prior probability or the group sizes are equal or $\hat{p}_i = \frac{1}{g}$ where \hat{p}_i is the expected portion of the observations and g is the number of groups. An example of this case is one in which a data set is comprised of 100 observations and is divided into two groups of 50. The next option for prior probability is to assign arbitrary probabilities or $\hat{p}_1 + \hat{p}_2 + \hat{p}_3 + \dots + \hat{p}_g = 1$. The third option is to estimate the prior probabilities by $\hat{p}_i = \frac{n_i}{N}$ where n_i is the number of observations from population π_i and N is the total number of observations.

Step three is to determine whether or not the variance-covariance matrices of the groups are equal or not. Bartlett's test can be used to make this determination. As stated earlier, LDA can be used when the variance-covariance matrices are equal and QDA must be used when they are not.

Step four is to compute the sample mean vectors and variance-covariance matrices used to determine the probability density functions. Equations 15 and 16 are the equations for the mean vector and variance-covariance matrix, respectively.

$$\bar{x} = \frac{1}{n} \sum_{i=1}^n x_i \quad (2.15)$$

In equation 15, \bar{x} is the sample mean vector, n is the number of observations and X_i is the observation for the i^{th} subject.

$$S = \begin{bmatrix} s_1^2 & \cdots & s_{1p} \\ \vdots & \ddots & \vdots \\ s_{p1} & \cdots & s_p^2 \end{bmatrix} \quad (2.16)$$

In equation 16, S is the sample variance-covariance matrix where the diagonal is populated with the variance for each sample and the off-diagonal elements are populated with the covariance between the j^{th} and k^{th} variables for the sample.

Step five is computing the discriminant functions. First, the pooled sample variance-covariance matrix must be estimated from the sample variance-covariance matrix.

$$S_p = \frac{\sum_{i=1}^g (n_i - 1) S_i}{\sum_{i=1}^g (n_i - 1)} \quad (2.17)$$

The pooled variance-covariance matrix, S_p , can be substituted for the variance-covariance matrix in the estimated linear score function.

$$\hat{s}_i^L(x) = -\frac{1}{2} \bar{x}_i' S_p^{-1} \bar{x}_i + \bar{x}_i' S_p^{-1} x + \log \hat{p}_i = \hat{d}_{i0} + \sum_{j=1}^p \hat{d}_{ij} x_i + \log p_i \quad (2.18)$$

Where $\hat{d}_{i0} = -\frac{1}{2} \bar{x}_i' S_p^{-1} \bar{x}_i$ represents an intercept term and $\hat{d}_{ij} = j^{th}$ element of $\bar{x}_i' S_p^{-1}$ represents regression coefficients of sorts. The classification rule will classify a new subject to the population that has the highest estimated linear score.

Step six is to determine the accuracy of the discriminant function(s) using a method such as the holdout method or cross-validation. After the model has been

developed using these steps and deemed acceptable at classifying the data, the final step is to apply the model to new data with unknown classification.

Many computational software packages will execute either PCA or LDA using just a few lines of code. All of the computation is done automatically by the algorithm, but it is important to understand how the program is executing the classification in order to know how and when to apply it.

III. Experimental Methods

3.1. Sample Preparation

All samples used for the study were prepared by AFRL/RX. The initial set of samples, sample set A, was prepared using a standard rain-erosion coat (REC) material for both the top coat and underlying REC. The coating layers were applied to an aluminum substrate. A schematic of the coating layer configuration is shown in figure 3.1.

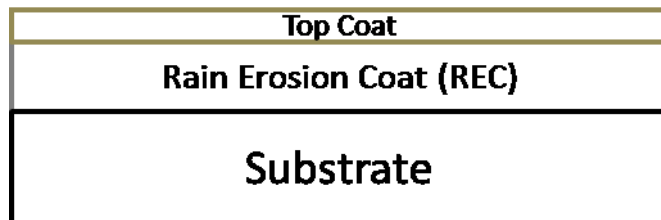


Figure 3.1: Schematic of coating layer configuration used on all samples in the study. A rain-erosion coating (REC) layer is applied to an aluminum substrate and a top coat layer is applied over the REC.

This coating layer combination is a fielded combination; however, it would normally be applied over several other coating layers. Sample set A contained four 3" x 6" rectangles cut from one large substrate and sealed along the edges using an epoxy before exposure. Two samples were left in an as-prepared condition and two were aged in an autoclave to the extent of visible degradation. The treatment conditions were 95 °C, approximately 130% relative humidity, and 144 hours of exposure.

The second set of samples, sample set B, was prepared with a different fielded REC and top coat combination. The top coat layer in sample set B has not been as

susceptible to degradation in the field, so it presents a more significant challenge to detect than the combination in set A. The top coat was 0.002" thick (50.8 μm) and the REC was 0.009" thick (228.6 μm). The layers were also applied to an aluminum substrate as shown in figure 3.1 above. Sample set B consisted of four 3" x 3" samples cut from a common large sample and sealed along the edges using an epoxy prior to exposure, as shown in figure 3.2.

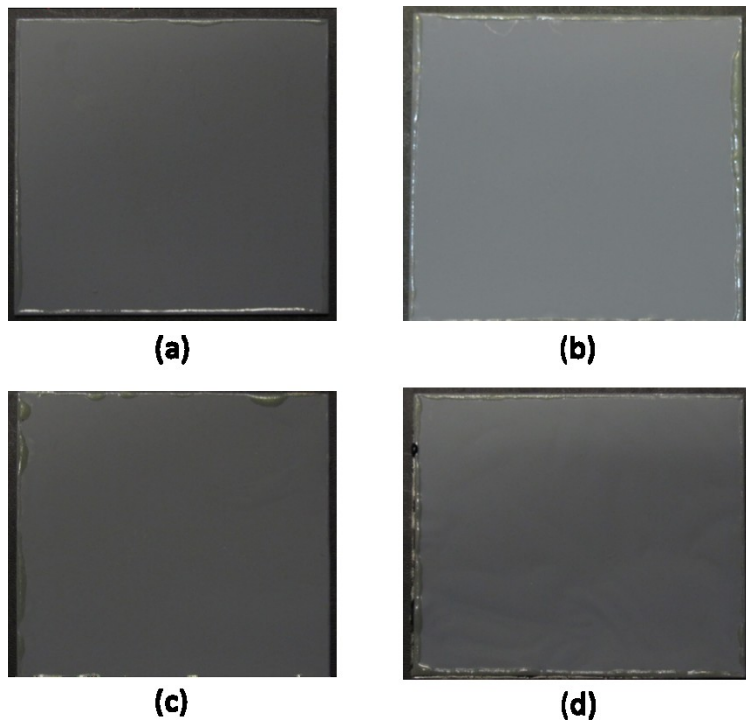


Figure 3.2: Pictures of the four samples in set B. The untreated sample is shown in (a), the 24 hour treatment is shown in (b), the 48 hour treatment is shown in (c), and the 96 hour treatment is shown in (d).

One baseline sample was left as-prepared (sample B1) and three samples were placed in an autoclave (B2-B4). The treatment conditions were 101 °C and approximately 130% relative humidity. Sample B2 was left in the autoclave for 24 hours, B3 for 48 hours, and B4 for 96 hours. The 96 hour exposure generated a level of visible degradation, while

samples B2 and B3 provided an intermediate level of degradation for the purpose of investigating the ability of FTIR to detect the degradation before it becomes visible to the eye. Table 3.1 is a summary of the treatment conditions for each sample set used during the study.

Table 3.1: Sample naming convention and treatment conditions for samples used during study.

Set A:		Set B:	
-95 °C		-101 °C	
Sample	Exposure Time	Sample	Exposure Time
A1	0 hrs	B1	0 hrs
A2	0 hrs	B2	24 hrs
A3	144 hrs	B3	48 hrs
A4	144 hrs	B4	96 hrs

3.2. Equipment

The hand-held FTIR device used for this study was an Agilent 4100 Exoscan, depicted in figure 3.3.



Figure 3.3: Image of Agilent Exoscan 4100 used for FTIR spectra collection[32].

The sampling band of the device includes both the functional region and the fingerprint region of the IR spectrum as discussed in the previous chapter. The external reflectance

sampling head was used for all data collection and a gold diffuse reflectance reference was used for calibration. The Exoscan utilizes a Michelson interferometer with a 4 cm^{-1} maximum resolution and a range of $4000\text{-}650\text{ cm}^{-1}$. The beam splitter is ZnSe and the detector is a deuterated triglycine sulfate (dTGS) pyroelectric detector with a detection range of $4000\text{-}650\text{ cm}^{-1}$. As a commercially available device, the device is assembled and sealed in this configuration at the factory. The internal components are not removable, but the specifics are included here to satisfy academic curiosity. All data was collected using the battery power source to better represent acquisition in a field environment. The Exoscan comes with a portable, handheld computer for instances when connection to a laptop or desktop computer is impractical; however, in this instance it was connected via USB cable to a non-networked desktop computer that was loaded with A2 Technologies software. This software suite communicated with the Agilent device, performing the calibration and saving the data.

3.3. Experimental Process

The experimental steps taken to demonstrate the potential of a handheld FTIR device for use as a field inspection for aircraft coatings are discussed in this section. It begins with device characterization and data collection and ends with the data analysis techniques used for pattern recognition and sample classification.

3.3.1. Device Characterization.

Two steps were taken to show that trends in the data are a result of the material changes in the samples, not a result of device inputs. The first step was to characterize the ability of repeated calibration throughout the course of the experiment to eliminate

device inputs into the data. This was done by collecting spectra on the calibration reference in the same manner as would be collected on the samples. Five spectra were collected per trial and three trials were conducted on each virtual sample. The device was recalibrated between trials and this process was repeated for four virtual samples. The mean, mean-subtraction, and standard deviation of the reflectance are plotted in figures 3.4, 3.6, and 3.7, respectively.

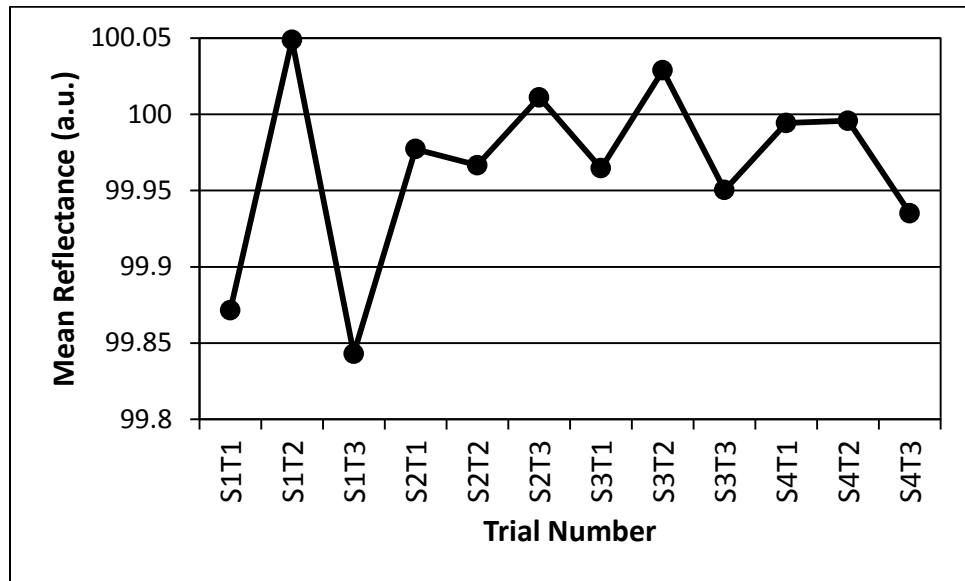


Figure 3.4: Mean reflectance data for repeated recalibration collected on a gold calibration reference. The first three trials deviate most from the expected value of 100% reflectance, but still all trials remain within 0.15% of the expected value.

Figure 3.4 is a plot of the mean reflectance collected on the diffuse reflectance gold reference standard provided with the device. It is expected that the mean reflectance would be 100% because gold is highly reflective in the infrared region of the spectrum, as shown in figure 3.5.

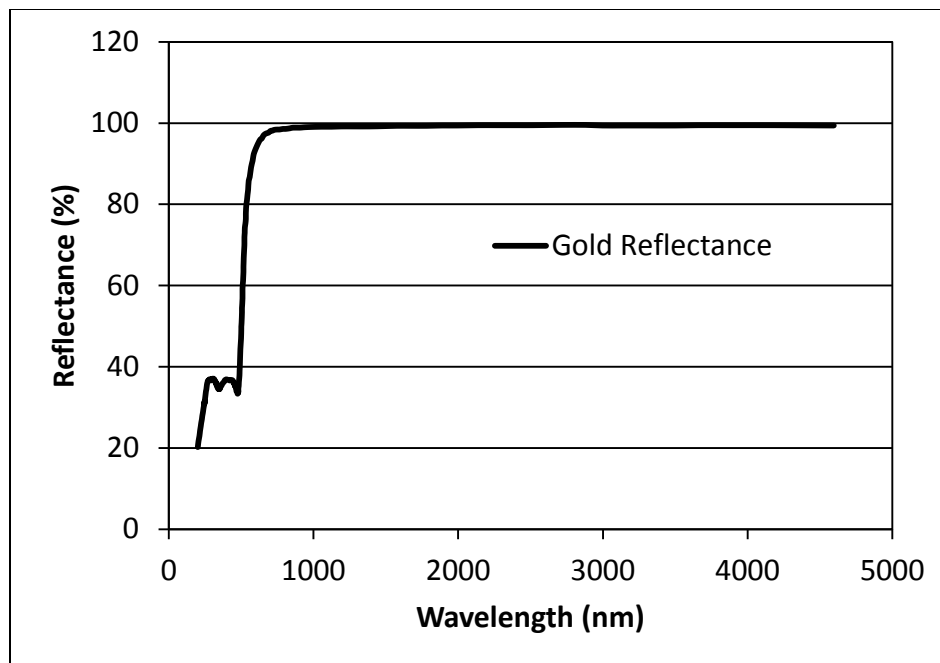


Figure 3.5: Reflectance spectrum for gold in the visible-IR spectrum. Gold (Au) is a nearly perfect reflector in the IR region of the electromagnetic spectrum.

The mean reflectance of the first trial collected after initial start-up deviates the most, with each successive trial getting closer to 100% reflectance. This behavior is also demonstrated in figures 3.6 and 3.7, the mean-subtraction and standard deviation of the reference standard data, respectively.

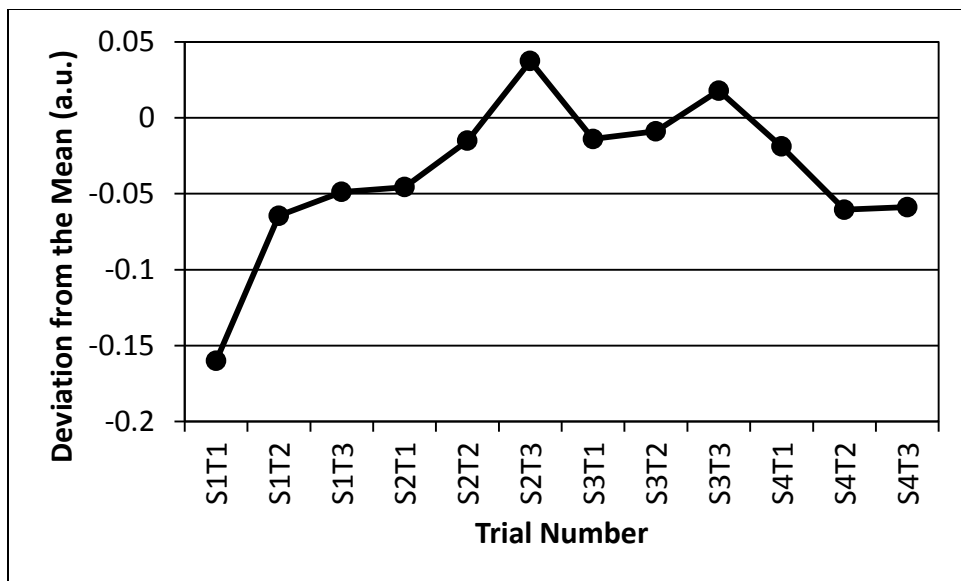


Figure 3.6: Mean-subtracted data for the repeated calibration reference sampling. The first trial after initial start-up shows the greatest deviation from the mean, with most trials deviating less than 0.05% from the mean value.

Figure 3.6 is a plot of the mean-subtraction of spot five, the last spot collected before recalibration. The mean subtraction was done on this spot because it was the longest elapsed time since the previous calibration and would deviate from the trial mean the most. As mentioned previously, the first trial after initial start-up has the highest mean deviation, with each successive trial showing less and less deviation. This behavior can be explained by the fact that the Exoscan utilizes a pyroelectric detector, which detects changes in temperature and converts that to a voltage. The greatest changes in temperature are experienced while the device warms up until the internal temperature of the device stabilizes.

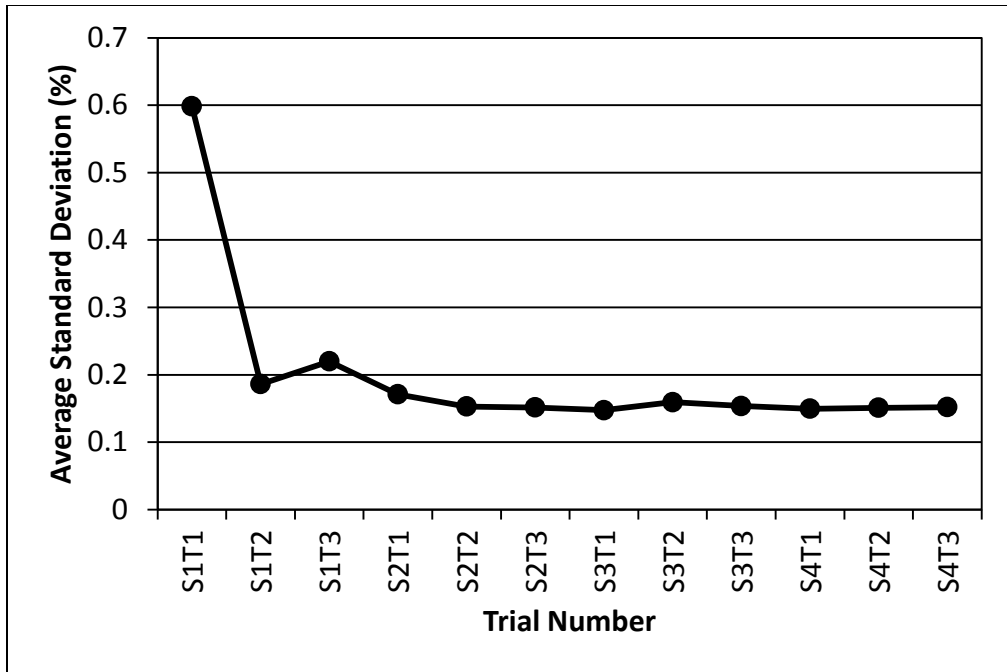


Figure 3.7: Average standard deviation as a percent of the mean reflectance for repeated calibration. The standard deviation is highest for the first trial after initial start-up, eventually leveling off around 0.15% after the third trial and re-calibration.

Figure 3.7 is a plot of the average standard deviation of the reference standard reflectance as a percentage of the mean reflectance. Again, the first trial shows the highest standard deviation with each successive trial becoming less noisy as the internal temperature stabilizes. The standard deviation remains near or below 1% of the mean reflectance, which is a strong indication that the signal-to-noise ratio for the Exoscan device is high. This information supports the assertion that any patterns or trends detected in the degradation of the samples are a result of functional differences between the samples, not the device. To further support that assertion, the device was allowed to cool down and another round of data was collected in the same manner as before. Five “spots” were collected per trial and three trials were collected per “sample” for four “samples”. The difference this time was that after the initial

calibration, the device was not re-calibrated. The same statistics were applied to the calibration reference standard spectra and plotted in figures 3.8-3.10.

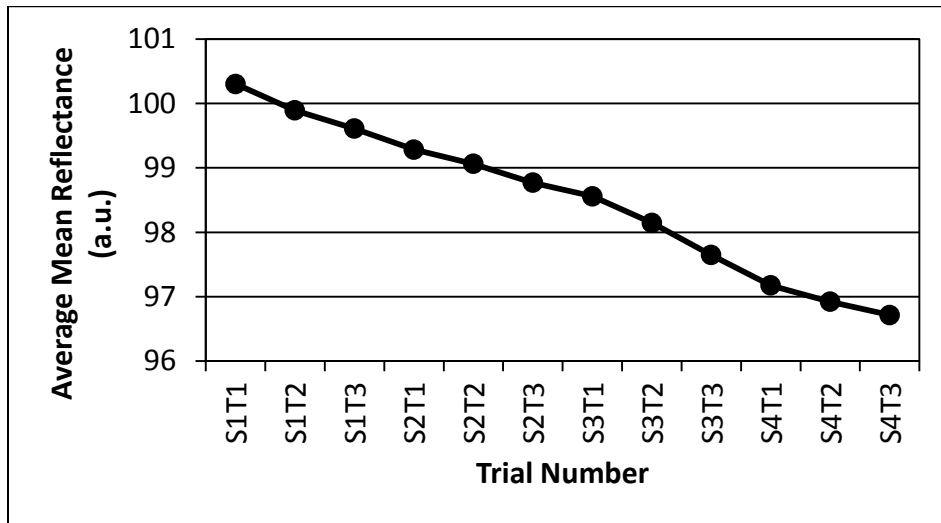


Figure 3.8: Average mean reflectance by trial collected using a gold reference standard without repeated calibration. The mean reflectance continues to decrease in magnitude throughout the sampling when the device is not recalibrated repeatedly. The expected mean reflectance is 100%.

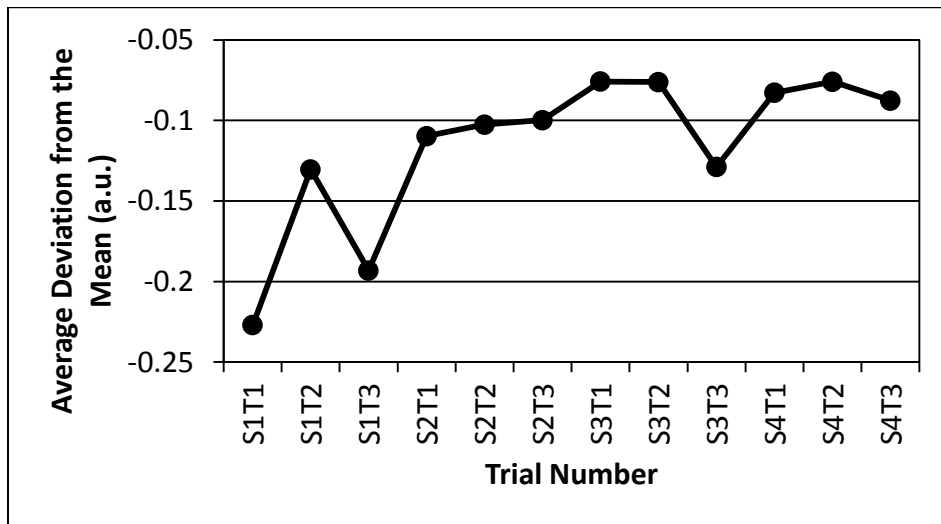


Figure 3.9: Average deviation from the mean by trial collected using a gold reference standard without repeated recalibration. The first few trials show the greatest deviation from the mean as with repeated recalibration. However, without the recalibration, the deviation never approaches zero.

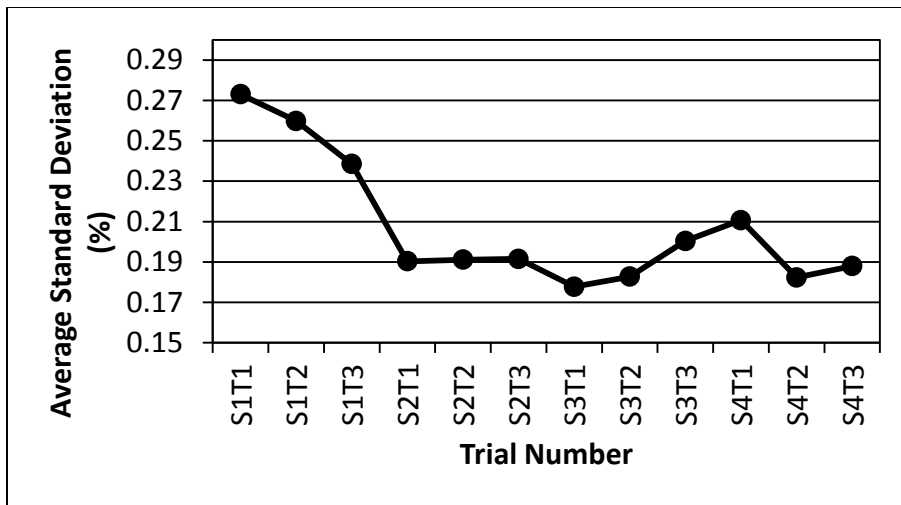


Figure 3.10: Average standard deviation as a percent of the mean reflectance collected using a gold reference standard without repeated recalibration. The device still has a high signal to noise ratio without repeated recalibration, but the standard deviation levels out around 0.19% of the mean.

Ultimately, the importance of this information is to demonstrate that the recalibration interval used during data collection is sufficient to ensure any patterns in the sample data are not the result of device contributions to the signal. Furthermore, and perhaps more importantly, this information must be considered if an inspection is ever developed using this technique. Regular recalibration of whatever device is used will have to be built into the inspection to ensure accurate scoring of the coating material. For this device, recalibration approximately every five minutes would be appropriate.

The other step that was taken to characterize the handheld FTIR device was to compare data taken with it to data taken with a bench top FTIR system for the same samples. The bench top system used for comparison was a Bruker Vertex 80v spectrometer connected to a Harrick Omni-Spec probe. Specular reflectance data was

collected on SiNC samples and compared to diffuse reflectance data collected with the Exoscan handheld. This data was used for comparison because it already existed from a previous study, which saved time in collecting it. It also demonstrates of how heat treatment can alter the FTIR reflectance spectrum of a material. In the case of SiNC composites, a large reflectance peak emerges as a result of the heat treatment with an oxide absorption valley at 1200 cm^{-1} as seen in figure 3.11.

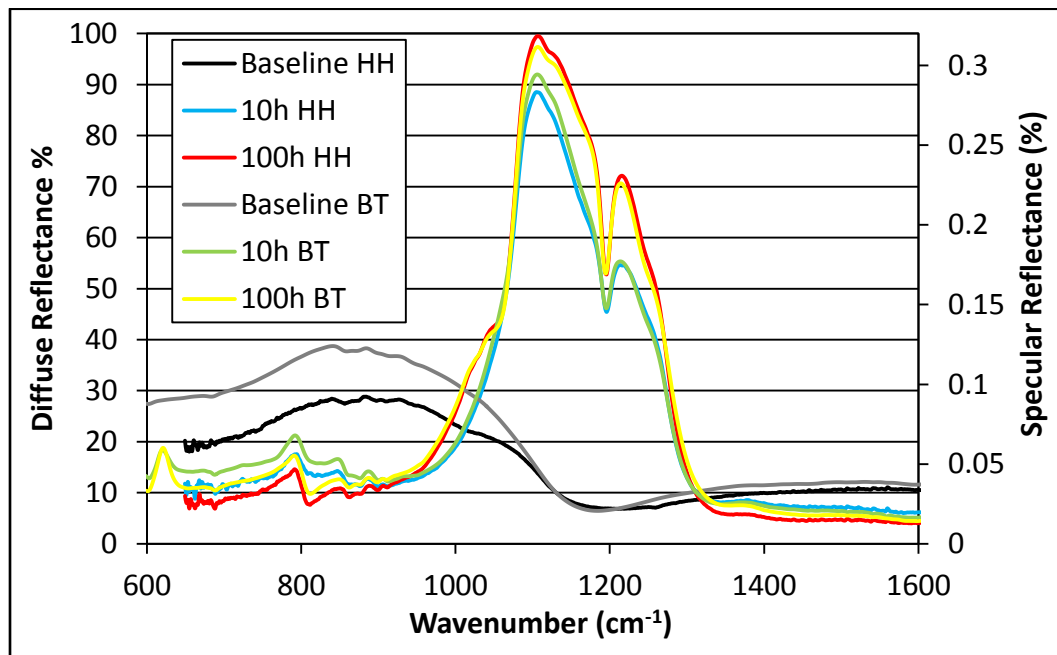


Figure 3.11: A comparison of the spectra collected on SiNC samples using the bench top and hand-held systems shows good agreement between the two. Note that the bench top data was collected using specular reflectance while the hand-held data was collected using diffuse reflectance.

Figure 3.11 is a plot of the diffuse reflectance of the SiNC samples collected using the Exoscan handheld compared to the specular reflectance collected using the Bruker bench top system. The comparison shows that the handheld device is capable of detecting all the same features at the same location as the bench top system, which provides more confidence in the data collected using the handheld device.

3.3.2. Sample Data Collection.

Because the primary objective of this research is to investigate whether or not a handheld FTIR device is capable of characterizing aircraft coating degradation in the field, the experimental setup was as representative of a field inspection as possible. However, limitations in the number of samples available for data collection and the need to re-use the same samples week after week drove some of the process. It was discovered on sample set A that the aperture would leave small rings in the surface if the device was pressed too hard on the sample. Therefore, the samples in set B were held up to the aperture gently by hand while the handheld device lay on its side near the edge of the table. This prevented the rings from being left in the surface and had the added benefit of good location repeatability. A hyperspectral image taken in the 8-12 μm region of the IR spectrum of an untreated sample and treated sample from sample set A illustrates that the coating material was applied uniformly across the sample as shown in figure 3.13. A picture of the scene is shown in figure 3.12 for comparison to the hyperspectral image.



Figure 3.12: Picture of the scene shown in the hyperspectral image in figure 3.13. The sample on the left is the untreated sample and the one on the right was treated to the level of visible degradation. Both samples are from sample set A. An exposed blister can be seen on the right-center of the treated sample.

The samples were irradiated with a blackbody source that elevated the temperature of the samples approximately 3°C above room temperature. Without raising the temperature, the samples could not be seen by the hyperspectral camera. The results of the scan are shown in figure 3.13. It is a color map of the average radiance and emittance of the sample by pixel without a background subtraction. The scene was scanned 64 times and averaged with a 4 cm^{-1} resolution. The untreated sample shows good uniformity across the sample surface. It must be noted that the hyperspectral imaging was done long after the FTIR data collection had been conducted, so the sample uniformity information was unknown during sampling.

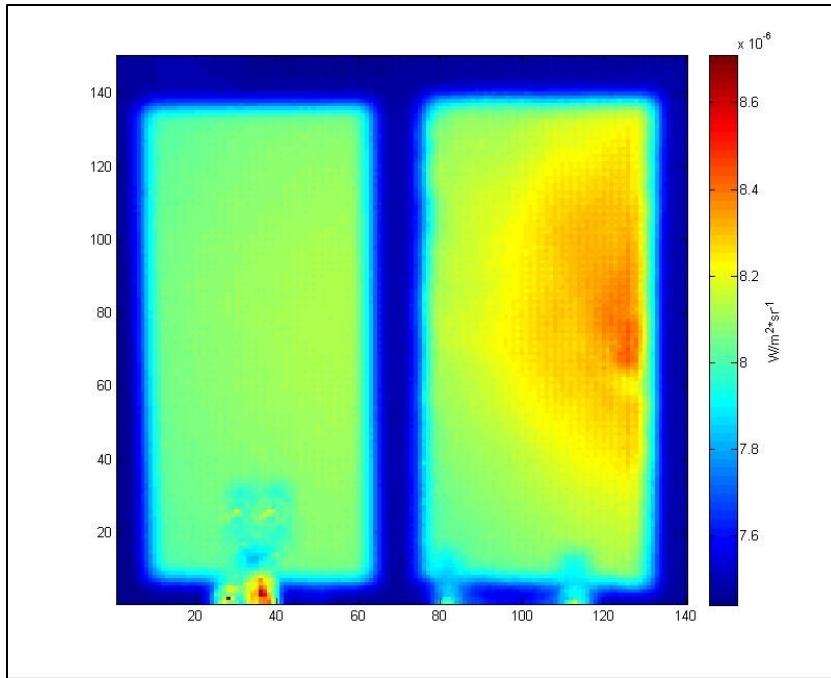


Figure 3.13: Hyperspectral image taken in the 8-12 μm region of the IR spectrum. The sample on the left is the untreated sample and the one on the right was treated to visible degradation. The red region of the treated sample is likely due to an increased emissivity of the sample caused by a delamination below the coating around the exposed blister.

There were two primary reasons for collecting data on several spots across the sample surface. The primary reason was because, as discussed in Chapter 2, DRIFTS is a highly variable FTIR sampling technique. Because it was unknown at the time of data collection how uniform the degradation was across the sample, the multi-spot sampling method provided more uniform coverage of each sample. By collecting several spots of data on each sample and repeating that process with recalibration between each trial, noise and variability could be reduced relative to any potential functional differences in the samples. The other reason for collecting several spots on each sample was the limited number of samples. The spectra generated at each spot could be analyzed as

individual samples, thus virtually increasing the number of samples. As will be discussed in the data analysis section, the multi-spot approach also allowed an investigation into tangential questions about degradation uniformity and time-dependent behavior. Due to the size of the samples in set A, six spots were used down the long edges of the samples. A diagram of the spot locations can be found in Appendix B, figure B.1. For sample set B, five spots were used: one in each corner and one in the center of the sample. A diagram of the spot locations for set B can also be found in Appendix B, figure B.2. All spots were interrogated once during a trial and three trials were conducted per sample per day for both sample sets.

For sample set A, two consecutive days of data collection were conducted immediately after the samples were prepared. Sample set A was prepared primarily as a practice set and a proof of concept set. The two sample extremes, untreated and visibly degraded, allowed for a demonstration of the ability of DRIFTS to detect the most extreme degradation. At the time, it was unknown if the approach would even detect the degradation. When it was shown that DRIFTS could detect the degradation on sample set A, sample set B was prepared with the intermediate levels of degradation and a different top coat material. Sampling was conducted on set B once per week for six weeks, skipping week five. The first sampling was conducted the day after the samples were prepared and repeated on the same day (Tuesday) each week thereafter. The fifth week was skipped because schedules did not allow for the work to be done. It also allowed for a two-week jump in any potential time-dependent behavior that might be degrading the coating. If there was time-dependent behavior to the degradation, a

two-week jump would be expected to be more visible in the data than the regular one week between sampling. Researchers working on the effort previously had noted that samples brought in from the field would not have significant visible degradation when they arrived, but it would manifest over time while sitting in the lab. If this behavior repeated itself with the samples used in this experiment, it would provide an opportunity to detect it in conjunction with the effort to detect the primary differences in degradation levels brought on through the heat treatment.

3.4. Data Analysis

There were four primary phases of data analysis conducted during this study. The first phase was analyzing the calibration data to demonstrate that the experimental procedure used for sample data collection reduced or eliminated any input from the handheld tool. Simple statistics were used for this analysis as discussed earlier in the calibration section of this chapter.

After it was shown that the procedure could be trusted to provide data with acceptable accuracy and precision, sample data was collected. After the first week's data had been collected, the average reflectance of each sample was plotted and compared. The reflectance spectra were examined for peak growth or changes in peak location. In the case of sample set A, that was the end of the analysis until much later because the reflectance spectra showed that coating degradation could be detected. For sample set B, examination of the mean reflectance of the four samples revealed that DRIFTs could detect the difference between the intermediate levels of degradation, but there was no clear trend in progression. It was decided that singular value

decomposition (SVD) would be applied to the data to see if it might reveal an otherwise undetectable pattern.

3.4.1. Singular Value Decomposition.

The mathematical theory behind SVD was discussed in Chapter 2, but the discussion that follows illustrates the steps that were taken in the application. For sample set B, a LabVIEW program was written to execute the SVD analysis and generate coefficient plots. Most computational programs such as MATLAB or Mathematica are capable of performing the same analysis and, in fact, MATLAB was used for the SVD analysis of sample set A as discussed later in this chapter. As an illustration of the process, a primitive example is provided using some simple functions to represent sample data. The original functions are plotted in figure 3.14. The functions used are sine and exponential functions. Each function represents a sample measurement. In the case of the data actually collected on the coating samples, each function would be a separate DRIFTS spectrum.

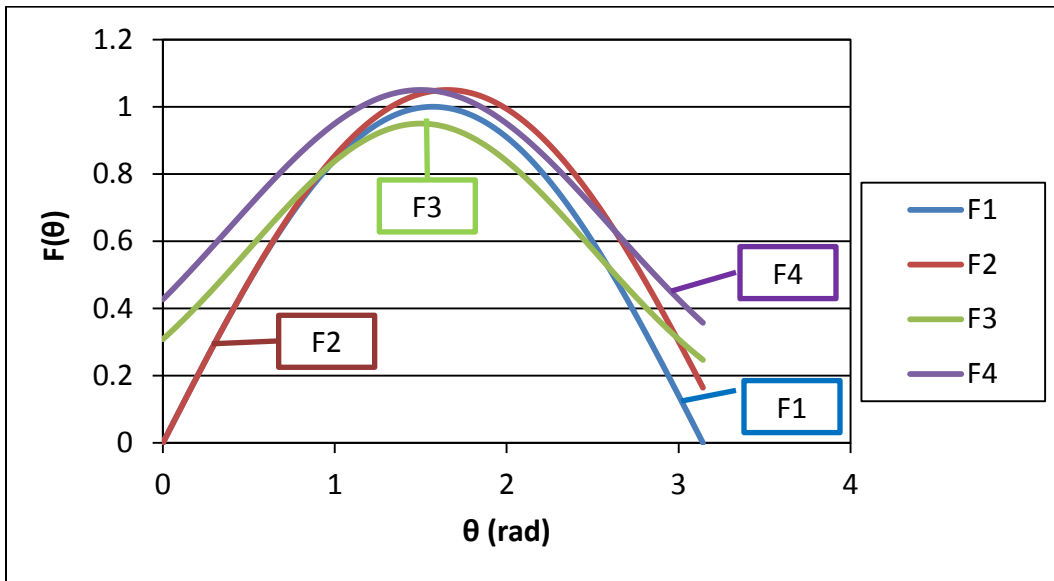


Figure 3.14: A plot of example functions used to illustrate the data analysis process applied to the sample data. Each function represents a separate measurement taken on a sample.

The first step in applying SVD as a pattern recognition technique is to execute a mean-subtraction of the data. The objective of conducting the SVD analysis is to find a linear combination of functions that best recreates the original data set, much like a Taylor series expansion of a function, as shown in Equation 3.1:

$$F(x) = a_0 + a_1 f_1(x) + a_2 f_2(x) + \cdots a_n f_n(x) \quad (3.1)$$

In equation 3.1, $F(x)$ is the original data, the a_n terms are weighted coefficients, and the $f_n(x)$ terms are the eigenfunctions of the data. If the mean is not subtracted first, then the first coefficient term is the mean of the data, a_0 . By executing the mean-subtraction before applying the SVD analysis, the coefficients that result from the operation are the remaining weighted coefficients and equation 3.1 becomes equation 3.2:

$$F'(x) = a_1 f_1(x) + a_2 f_2(x) + \cdots a_n f_n(x) \quad (3.2)$$

The mean is calculated across all the measurements for each x-value. In the example, the mean of the four functions is calculated for each value of theta. In the sample data, the mean reflectance is calculated for all measurements by wavenumber. The mean is then subtracted from each sample measurement by wavenumber. Figure 3.15 is a plot of the mean-subtracted data for the example functions.

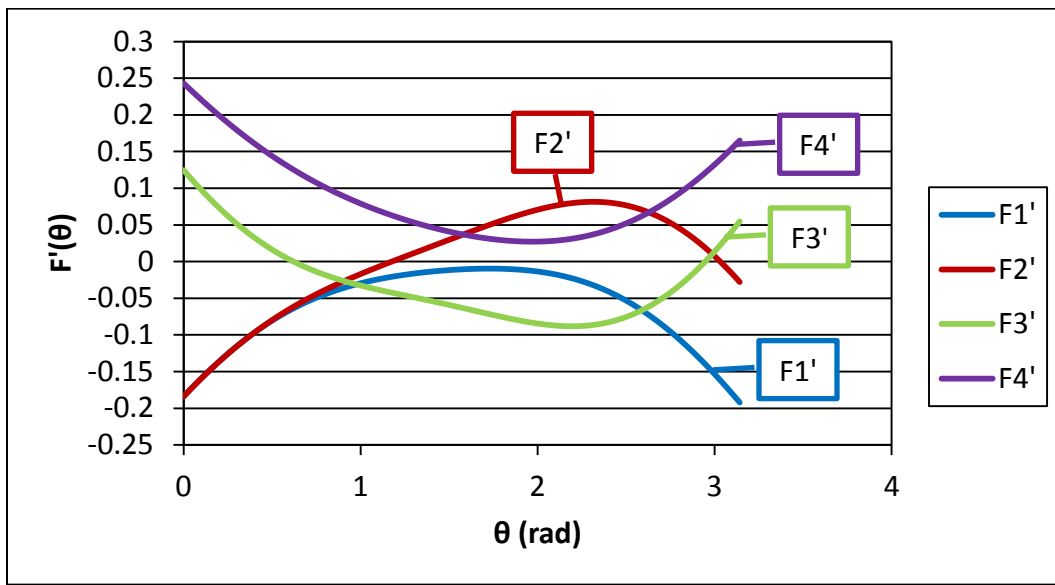


Figure 3.15: A plot of the mean-subtracted data for the four example functions.

After the mean-subtraction is done, SVD is conducted on the resulting mean-subtracted data matrix to generate the new basis functions. In the SVD equation, these new basis functions are the columns of U and V (Refer to Chapter 2). It does not matter which matrix is used as the new basis, but whichever one is selected must be the one that is used throughout the analysis. To find the weighted coefficients, the Kronecker delta function can be applied because the basis vectors in the columns of U and V are orthonormal as discussed in Chapter 2. In other words, to calculate the coefficients, the new basis function matrix is multiplied by the mean-subtracted data matrix. The

coefficient matrix will have the same number of columns as measurements and the same number of rows as there are functions. In the example being used, there are 180 coefficients (the columns) for each function because the functions have 180 measurements (180 degrees/pi radians). There are four rows of coefficients because there are four functions, or samples. In the example scenario, the coefficients after the third one for each function are all practically zero (10^{-17} or less), so only the first three are used. This is common for most instances of SVD analysis, including the DRIFTs data collected and analyzed for this research. The first three coefficients for the example functions are plotted in figures 3.16 and 3.17.

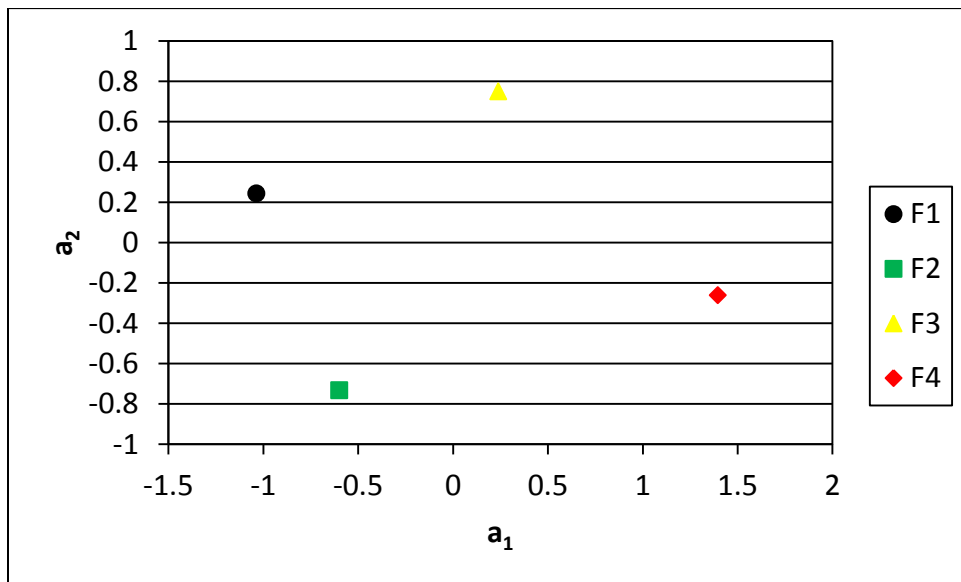


Figure 3.16: Plot of the first and second coefficients for the example functions.

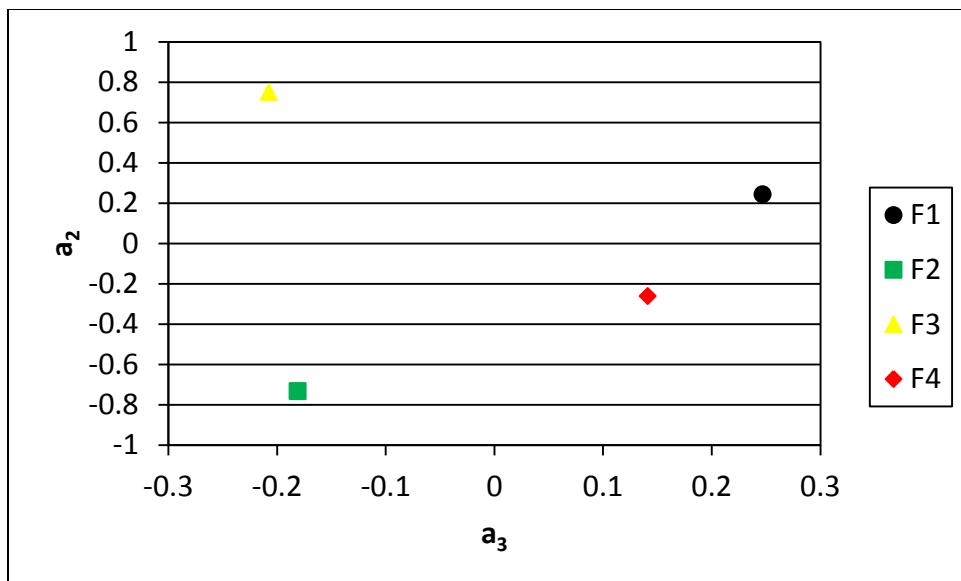


Figure 3.17: A plot of the second and third coefficients for the four example functions.

The importance of figures 3.16 and 3.17 is how an entire function can be reduced to a data point on a scatter plot. The same steps were taken with the spectra collected on the coating materials. Using this process, each spectrum collected is reduced to a data point. To demonstrate the validity of the process, the reverse steps can be taken to reconstruct the original functions. However, only the first three coefficients will be used to show they capture most of the data. When the first three coefficients are multiplied by the corresponding basis functions and plotted, what results is a reconstruction of the mean-subtracted functions as shown in figure 3.18. The mean-subtracted functions, reconstructed using only the first three coefficients, lay almost perfectly on top of the original mean-subtracted example functions.

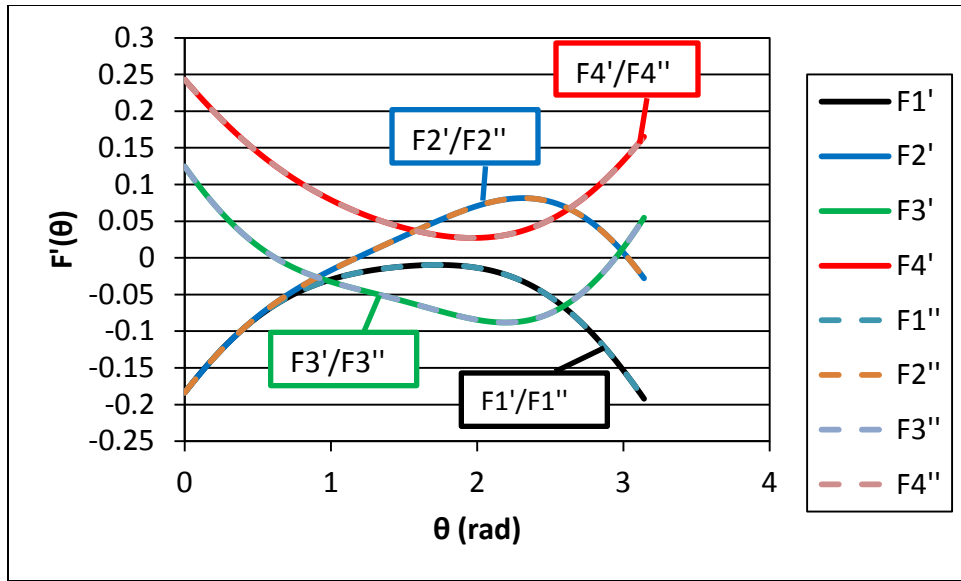


Figure 3.18: A plot of the original mean-subtracted example functions and the mean-subtracted functions reconstructed using only the first three SVD coefficients and basis functions. The functions $F1'-F4'$ are the original mean-subtracted functions and the functions $F1''-F4''$ are the reconstructions.

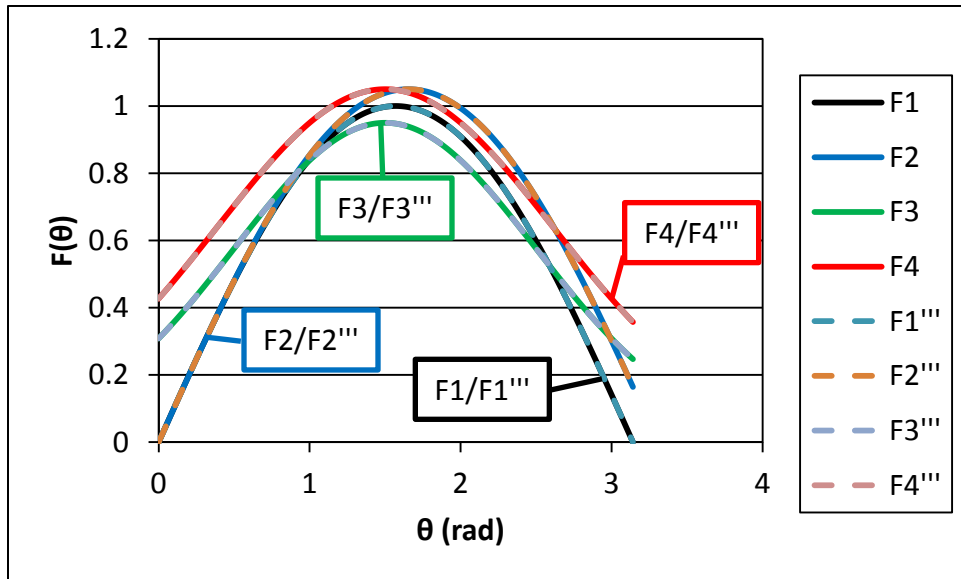


Figure 3.19: A plot comparing the functions reconstructed using only the first three coefficients and basis functions with the original example functions. The reconstructed functions lie on top of the original functions, demonstrating how SVD analysis is capable of dimensionality reduction.

When the mean is added back into the reconstructed mean-subtracted functions and plotted with the original functions, they are almost identical as shown in figure 3.19. The last two steps shown here were included as a demonstration of the power of the SVD technique to reduce a complex function with 180 components down to only three. They were not actually executed on the coating sample data. Once the coefficients were calculated, they were plotted as shown above and examined for patterns. An example of one of the coefficient plots generated from the coating samples is shown in figure 3.20. The rest of the coefficient plots can be found in the next chapter or in Appendix D.

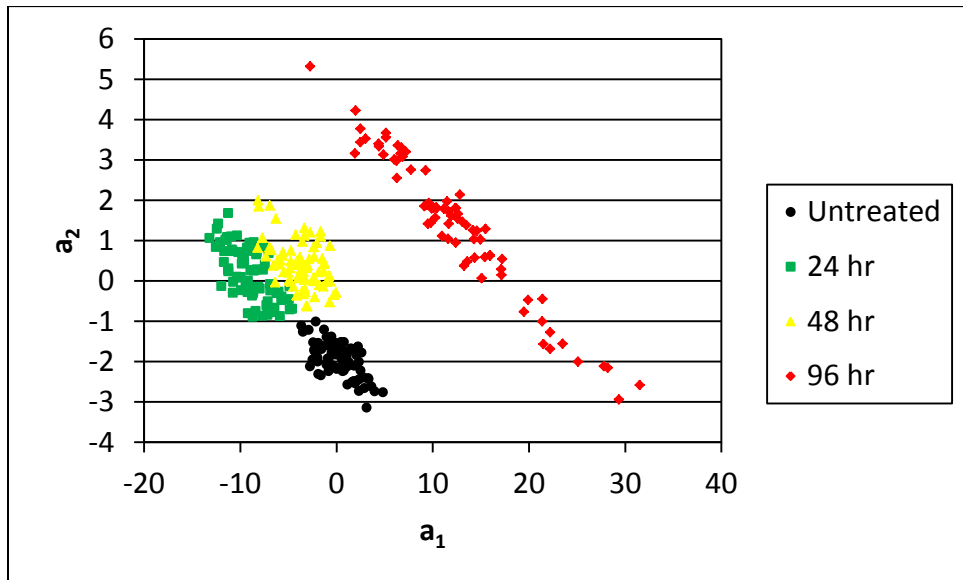


Figure 3.20: A plot of the first two coefficients generated from coating samples in various states of degradation.

The LabVIEW program that was used allowed the selection of smaller bands of the spectrum to be examined, which permitted the analysis of individual features as well as groups of features. Initially, each individual feature, such as a prominent peak or valley, was analyzed for trends in the SVD coefficients, but none emerged. Then groups of

features were analyzed and the best groups were selected based on coefficient clustering and separation.

3.4.2. Discriminant Analysis.

After qualitatively selecting bands for their coefficient clustering and separation, discriminant analysis was used to quantitatively determine the best bands for classification purposes. The first three coefficients for each band of interest were taken from the LabVIEW program and run through MATLAB for the discriminant analysis. The ClassificationDiscriminant.fit command was used to generate the classifiers for each band. The code used for the discriminant analysis can be found in Appendix C. For sample set B, all the sample data was included in the development of the classifier. This is because discriminant analysis was being used as a quantitative method of determining which bands demonstrated the most separation between samples. An idealized illustration of how discriminant analysis generates a classification function is shown in figure 3.21.

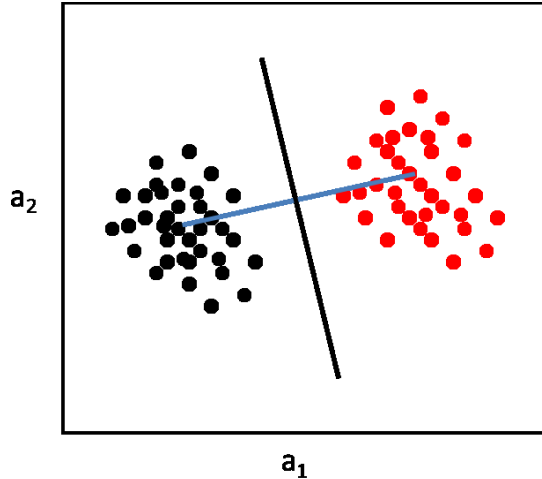


Figure 3.21: An idealized schematic of how discriminant analysis generates a classifier using all the data collected. The black line represents the discriminant function used to classify the samples. The black dots represent the untreated sample and the red dots represent the treated sample used to generate the classification rule.

Initially, only the first two coefficients were used to generate the classifier because there seemed to be sufficient separation between the samples to provide a highly accurate classifier. Several bands did produce a model that had less than 5% error, which is an acceptable rate for this type of inspection. The third coefficient was included in the classification rule and compared to the error from only using the first two coefficients. In some bands, the inclusion of the third coefficient made the model even more accurate. However, in some bands the inclusion of the third coefficient had a negative effect on the accuracy. The classifier accuracy, or ability of the band to distinguish between degradation levels, was determined using re-substitution and k-fold

analysis. Confusion matrices were also generated for all the bands examined in sample set B. The detailed results and discussion of the analysis are in the next chapter.

3.4.3. Classifying New Sample Data.

The data collected on sample set A was analyzed using MATLAB to execute the SVD, instead of LabVIEW. Again, the MATLAB code can be found in Appendix C. Sample set A was used to demonstrate how the proposed approach would be applied as an inspection in the field. Since it contained a pair of untreated samples and a pair of samples treated to the same level of degradation, it provided an opportunity to test the proposed classification approach. Two samples, one untreated and one degraded, were analyzed using SVD to determine the first three coefficients for use as the reference set. The other two samples in set A represent new measurements on unknown coatings. In this case, it is known *a priori* that one of the new samples is an untreated coating and the other is a treated coating. In an inspection situation, the coating degradation would not be known. If an inspection were generated from the proposed approach, reference data would be collected on known samples and a classification rule would be generated. This set is called the training set. The mean of the training set is subtracted from the data collected on the unknown samples. This is done because the new measurements must be projected onto the basis established by the training set for classification. If each set of samples are analyzed separately, then two separate bases are generated. The objective is not to compare how the training basis is related to the new measurement basis, rather to determine where the new measurements lie on the training set basis. The basis functions generated from the training set are then

multiplied by the new mean-subtracted data set to generate the coefficients. An idealized schematic of a situation where the new measurements can be classified with 100% accuracy is shown in figure 3.22. The locations of the training set data and the discriminant function do not change when the new data is added to the plot. In figure 3.22, the black and blue dots represent the known and unknown sample data for one class of sample while the red and orange dots represent the known and unknown sample data for the other class of sample.

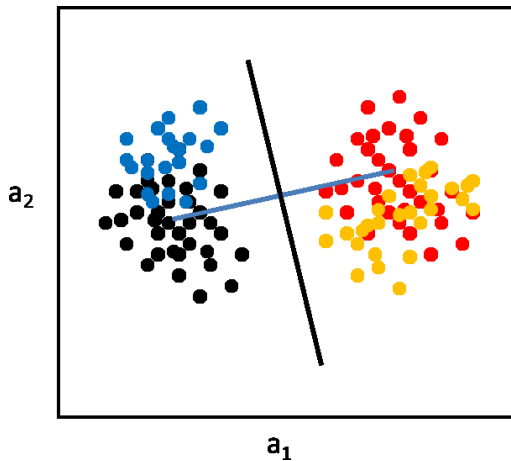


Figure 3.22: A schematic of an idealized case where the new measurements can be classified with 100% accuracy. The blue dots represent new measurements on an untreated sample and the orange dots represent new measurements on a treated sample.

It is probable, and perhaps even more likely, that the new measurements will not be able to be classified 100% correctly because of variability in the coating or the measurement. This was the case with the new measurement data generated from the samples in set A. Figure 3.23 is a plot of the first two coefficients generated from the training set and the “unknown” sample set in the fingerprint region. The new

measurements of the “unknown” untreated sample project onto the training set nicely, but the “unknown” treated sample varies from the treated sample used in the training set. The detailed discussion of the results of the process can be found in Chapter 4.

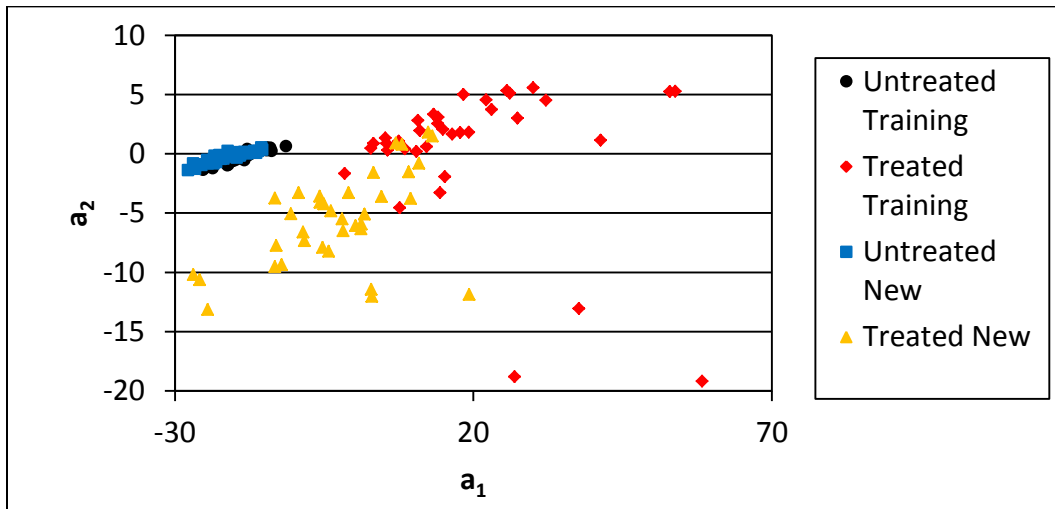


Figure 3.23: A plot of the first two coefficients generated from the fingerprint region for both the training set and the new data set for prediction. The new untreated sample is on top of the untreated sample used for training and the treated sample is clearly distinct from the untreated samples.

For sample set A, the first three SVD coefficients were generated using both the entire spectrum and the fingerprint region. An investigation into other bands was not done on set A because the work done on sample set B, combined with the literature regarding IR spectra of polymers, showed that the fingerprint region provides unique information about the coatings. As with sample set B, classification rules were generated using both the first two and first three coefficients of the training set. Then the coefficients generated from the unknown samples were input into the respective classification rules for prediction of the degradation level. Again, a detailed discussion of the results of the process can be found in the next chapter.

IV. Results and Discussion

4.1. Introduction

All of the discussion in the previous chapters lays the foundation that this chapter is based upon. Since the theory and process have already been explained in chapters two and three, respectively, they are not repeated here. The results of the research are presented in logical progression from the initial effort of determining whether or not the system could detect coating degradation through a spot-to-spot analysis of each sample, investigation into the potential existence of time-dependent behavior, and finally the classification of new sample data using a training sample set.

4.2. Degradation Detection

Figures 4.1 and 4.2 are plots of the mean reflectance collected the first week on sample set B. Figure 4.1 is the entire sampling spectrum and figure 4.2 is a closer look at the $1800-800\text{ cm}^{-1}$ range to better illustrate the subtleties of the features. From a qualitative examination of the spectra, there are clearly changes in reflectance intensities. Throughout the sampling spectrum, the 24 hour treatment sample has the highest reflectance, followed by the 48 hour treatment sample, the untreated sample, and finally the 96 hour treatment sample. It was expected that any evident trend in the data would progress in order from the untreated to the maximum treatment level or vice versa. Additionally, there is no evident change in feature location, emergence of new features, or diminishing of existing features as anticipated from the literature. This

development is what prompted the use of SVD to analyze each spectrum individually and look for a pattern in the samples.

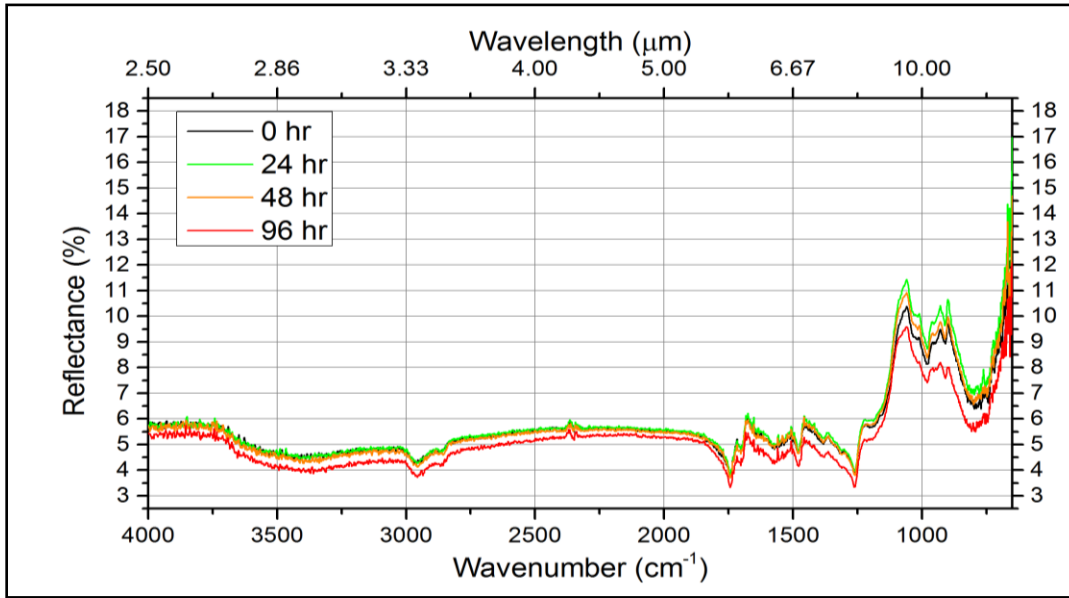


Figure 4.1: Plot of the mean reflectance for sample set B collected the first week. Examination of the spectra does not immediately reveal an apparent relationship between duration of exposure and peak intensity or location.

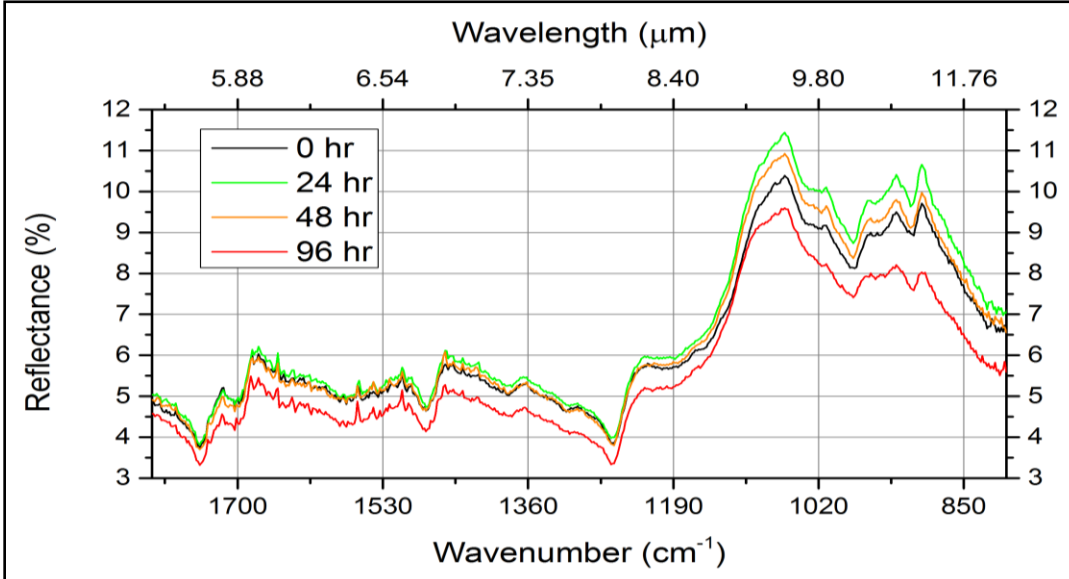


Figure 4.2: Plot of the far end of the sampling spectrum, including the fingerprint region, for sample set B collected the first week. No apparent relationship exists between reflectance and exposure duration.

4.3. Singular Value Decomposition (SVD)

The discussion that follows primarily pertains to the specific bands being considered, but it generally applies to the other bands of the spectrum as well. Initially, the entire spectrum was analyzed using SVD. When the coefficients did not demonstrate potential for discrimination between samples, individual spectral features were selected and examined. Again, the SVD coefficients did not show sufficient discrimination between samples so larger bands that captured groups of spectral features were examined. Many of these spectral bands qualitatively showed potential for discrimination between samples and one representative band is discussed here, the $975-875 \text{ cm}^{-1}$ ($10.3-11.4 \mu\text{m}$) band. The remaining coefficient plots for all the bands examined can be found in Appendix D. The SVD coefficients for the other bands exhibited similar clustering behavior, but not necessarily with the same values or relationship to one another. Each data point on one of the plots below represents one entire reflectance spectrum collected on one of the samples. Since 15 spectra were collected per sample per week for five weeks, there are 300 data points representing 300 spectra on each plot. The objective of the research is to detect and accurately classify the varying levels of degradation with the eventual goal of predicting how much service life is left in the material. Therefore, the desired results are tightly clustered groups that are clearly separable from the other groups for classification purposes.

4.3.1. $975-875 \text{ cm}^{-1}$ ($10.3-11.4 \mu\text{m}$).

At the far end of the sampling spectrum, there are several reflectance peaks in the $900-1000 \text{ cm}^{-1}$ range that might reveal a recognizable pattern. Figure 4.3 is a plot of

the first two SVD coefficients for the $975-875 \text{ cm}^{-1}$ band, where a pattern does indeed emerge.

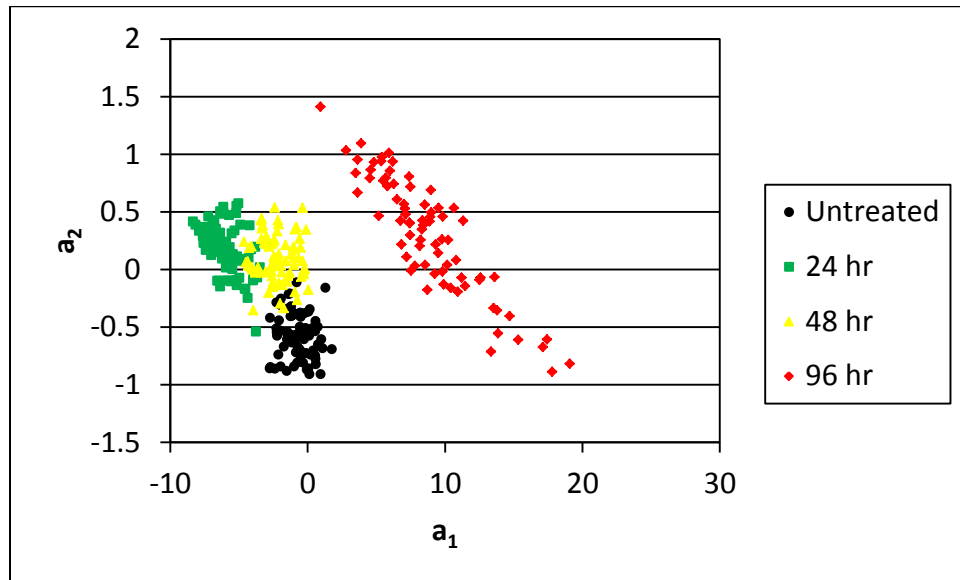


Figure 4.3: Plot of the first two coefficients in the $975-875 \text{ cm}^{-1}$ band for sample set B. The 96 hr treatment level is clearly distinguishable from the other three samples while the other three have some overlap between them.

When the first two coefficients are plotted against each other, a clustering pattern emerges for each of the samples. Samples B1-B3 show some overlap around the edges while sample B4 is clearly distinct from the other three. The overlapping of coefficients from samples B2 and B3 is common throughout all the bands. A potential explanation of this behavior is that those spots on the sample are actually at a degradation level consistent with a different treatment level. In other words, there are spots on the 24 hour sample that are mixed in with the 48 hour sample and vice versa. It is possible that some spots on the 24 hour sample are actually degraded to a 48 hour treatment level or spots on the 48 hour sample are only degraded to a 24 hour treatment level. This poses a potential problem when considering the objective of data classification and developing

an inspection. It is probable that fielded coating degradation levels, as represented by the laboratory samples in this work, will demonstrate similar non-uniformity across the surface of the aircraft.

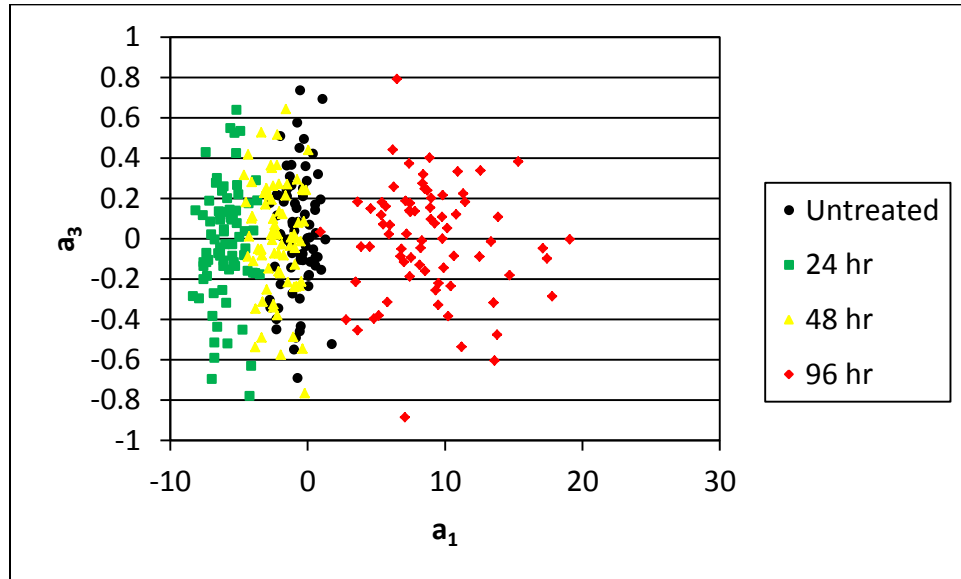


Figure 4.4: Plot of the first and third coefficients in the $975-875\text{ cm}^{-1}$ band for sample set B. There is some separation between samples along the first coefficient, but not in the third coefficient.

When the first and third coefficients are plotted against each other in figure 4.4, the distinction between samples along the first coefficient is still visible. The third coefficient contributes little to the clustering of the samples. This behavior is common throughout the bands analyzed. In some bands, the plot of the first and third coefficient against each other is an incoherent cluster of all four samples like figure 4.5 below, which is a plot of the second and third coefficients in the $975-875\text{ cm}^{-1}$ ($10.3-11.4\text{ }\mu\text{m}$) band.

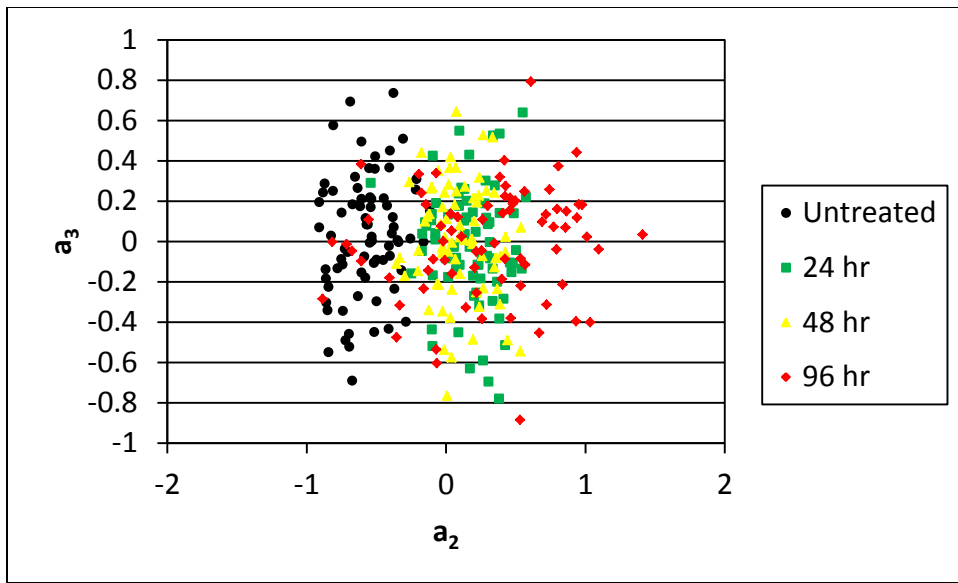


Figure 4.5: Plot of the second and third coefficients in the $975-875\text{ cm}^{-1}$ band for sample set B. The untreated sample is separable along the second coefficient from the rest of the samples, but there is still overlap with the 96 hr sample. The other samples are indistinguishable from each other.

A plot of the second and third coefficients in the $975-875\text{ cm}^{-1}$ band for sample set B is shown in figure 4.5. It was not expected that the second and third coefficient would reveal a useful separation between samples because of how little information about the original data they contain. However, the plot is included here because it is representative of the second versus third coefficient plots for many of the other bands.

After narrowing down the number of bands of the spectrum for consideration, the question of how to determine which band had the best clustering had to be answered. Examination of the coefficient plots shows that a line could be drawn between two samples and a count conducted of how many spectra are on either side of the line. Linear discriminant analysis (LDA) does exactly that with statistical significance built into the algorithm. Since the application of SVD requires the assumption of

linearity to be made up front, LDA should also be capable of producing a statistically significant classifier that can discriminate between samples.

LDA was used as a statistical method of determining which bands demonstrated the best clustering and greatest separation between samples. Since the coefficient plots show that the first and second coefficients generate most of the discrimination between samples, only the first two coefficients were initially used to generate the classifiers. As discussed in Chapter 3, many computational software packages have the ability to quickly execute LDA and MATLAB was used in this case. Confusion matrices, re-substitution error rates, and k-fold error rates were generated for each band and compared. This information for the 975-875 cm⁻¹ band is presented in table 4.1 below. The confusion matrices and error rates for the other bands can be found in Appendix D.

Table 4.1: Confusion matrix and error rates for the 975-875 cm⁻¹ band of sample set B. The addition of the third coefficient as a discriminator does not affect the error rates in this band.

975-875 (cm ⁻¹)	2 Coefficients	Predict	0	24	48	96	Resubstitution Error %	Number of Errors (per 300)	Kfold Error (10 Fold) %
		Truth	hr	hr	hr	hr			
975-875 (cm ⁻¹)	2 Coefficients	0 hr	70	0	5	0	9.33	28	9.33
		24 hr	1	66	8	0			
		48 hr	4	10	61	0			
		96 hr	0	0	0	75			
975-875 (cm ⁻¹)	3 Coefficients	0hr	70	0	5	0	9.33	28	9.33
		24 hr	1	66	8	0			
		48 hr	4	10	61	0			
		96 hr	0	0	0	75			

As would be expected from looking at the coefficient plots for this band, the classifier does a reasonable job of discriminating between the samples using only the first two

coefficients. Also as expected, the misclassifications occur primarily between the 24 and 48 hour samples. The classifier correctly classifies the 96 hour sample for 100% of the spectra. Since some of the bands also displayed clustering along the third coefficient, a new classifier was generated for each band with it included to see if it would improve the accuracy of the classification rule. Again, confusion matrices and error rates were generated for each band and compared to the error rates of the other bands as well as to the error rates from using only the first two coefficients. This information is also presented in table 4.1. The inclusion of the third coefficient had no effect on the accuracy of the classifier in the $975-875\text{ cm}^{-1}$ band. In some instances, the inclusion of the third coefficient improved the accuracy of the classifier and in some instances it actually reduced the accuracy. Again, the confusion matrices and error rates for all the bands can be found in Appendix D for further examination. After comparing all of the bands, there was one band that showed the greatest accuracy using both the first two and first three coefficients. This band was discussed in Chapter 2 as the fingerprint region of the spectrum, the $1220-850\text{ cm}^{-1}$ band, and is discussed next.

4.3.2. $1220-850\text{ cm}^{-1}$ (8.2-11.8 μm).

The $1220-850\text{ cm}^{-1}$ region of the spectrum falls within the fingerprint region of the IR spectrum for polymer samples. As discussed in Chapter 2, this region is often unique to a specific material because it contains the energies associated with complex vibrational modes. Therefore, it was expected to have the greatest potential of any of the bands to discriminate between the samples. Figures 4.6-4.8 are plots of the first three SVD coefficients in this band for sample set B.

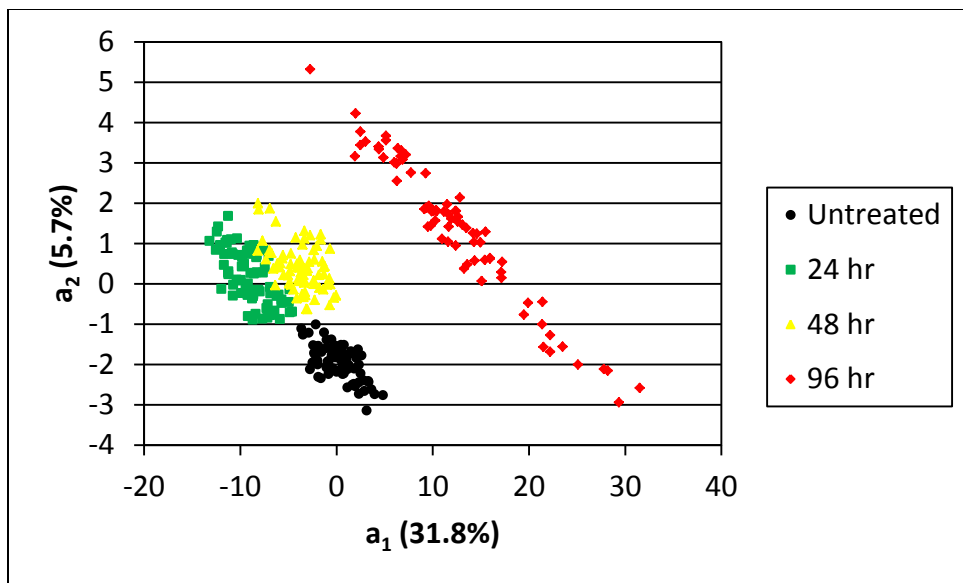


Figure 4.6: Plot of the first two coefficients in the $1220-850\text{ cm}^{-1}$ band for sample set B. There is significant clustering of the samples that makes each sample clearly distinguishable from each other.

Figure 4.6 is a plot of the first two coefficients for the $1220-850\text{ cm}^{-1}$ band for sample set B. Unlike many of the other bands, both the untreated sample and the 96 hour sample are completely separated from the 24 and 48 hour samples. There is some overlap between the 24 and 48 hour samples, but the groups are tightly clustered. The magnitude of the variance captured by each basis vector is included in the axis titles to illustrate the importance of each to describing the data set. Typical values for the first basis vector (a_1) are often 85% or higher, but is only 31% here. The reduction in magnitude from a_1 to a_2 is still significant, which indicates that a_1 is still capturing the majority of the variance in the data. More information about the basis vectors and relative importance of each can be found in Appendix F.

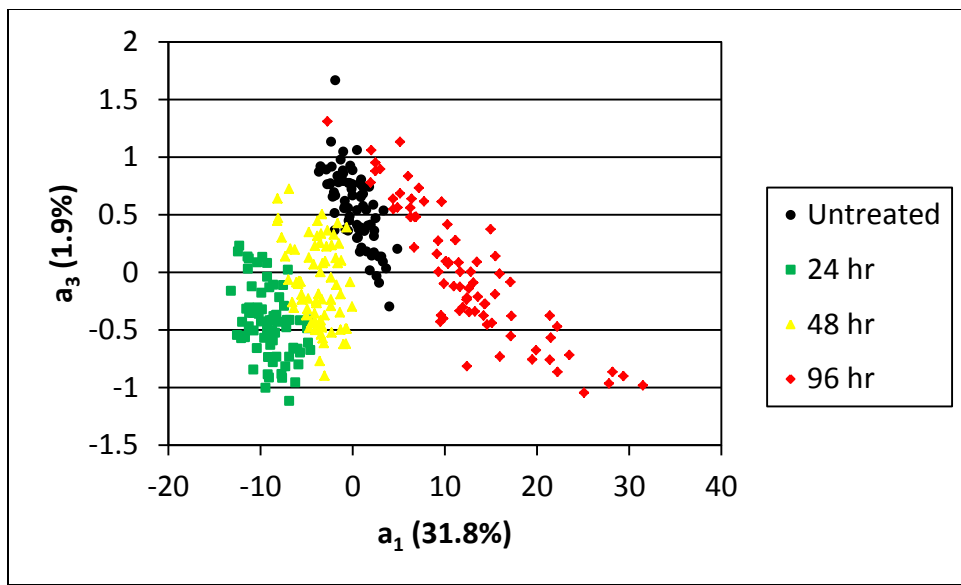


Figure 4.7: Plot of the first and third coefficient in the $1220-850\text{ cm}^{-1}$ band for sample set B. There is separation in the first coefficient, but not in the third coefficient.

Figure 4.7 is a plot of the first and third SVD coefficients in the $1220-850\text{ cm}^{-1}$ band for sample set B. Again, unlike many of the other bands, there is still significant separation between the samples. While there is not a progression from the untreated sample to the 96 hour sample, there is little overlap between the samples. This is a good indication that the inclusion of the third coefficient in the LDA analysis will improve the accuracy of the classifier.

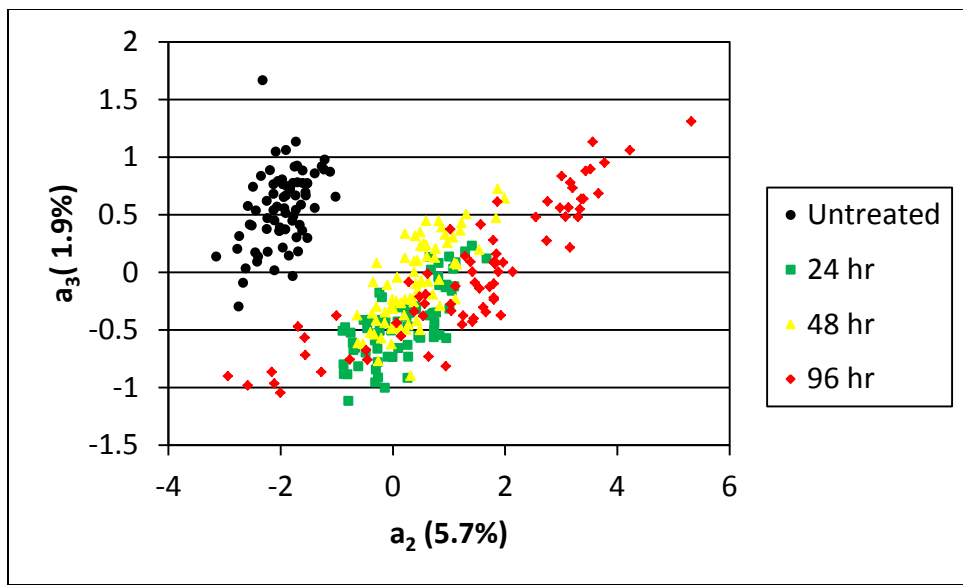


Figure 4.8: Plot of the second and third coefficients in the $1220-850\text{ cm}^{-1}$ band for sample set B. The untreated sample has separation from the other three, but the other three samples are indistinguishable from each other.

In figure 4.8, the second and third coefficients are plotted against each other. This plot demonstrates the power of using this approach for analyzing FTIR spectra. The untreated sample is clearly separated from all the treated samples, which is what is intuitively expected. Even though the treated samples all lie on top of each other in this figure, they are still clustered together. When taken together, figures 4.6-4.8 show why this band has great potential for use in detection and classification of coating degradation should this approach be pursued for an inspection. Even more promising are the results of the LDA analysis of this band.

Table 4.2 contains the results of generating classifiers using the first two and the first three coefficients. In both instances, the classifier correctly assigns both the untreated and the 96 hour samples 100% of the time.

Table 4.2: Confusion matrix and error rates for sample set B in the $1220-850 \text{ cm}^{-1}$ band. This band has the lowest error of all the bands examined using both the first two and all three coefficients. Using the first three coefficients reduces the error compared to using only the first two coefficients.

1220-850 (cm^{-1})	2 Coefficients	Truth \ Predict	0 hr	24 hr	48 hr	96 hr	Resubstitution Error %	Number of Errors (per 300)	Kfold Error (10 Fold) %
			0 hr	24 hr	48 hr	96 hr			
1220-850 (cm^{-1})	2 Coefficients	0 hr	75	0	0	0	3.0	9	3.33
		24 hr	0	70	5	0			
		48 hr	3	1	71	0			
		96 hr	0	0	0	75			
1220-850 (cm^{-1})	3 Coefficients	0hr	75	0	0	0	1.67	5	2.0
		24 hr	0	72	3	0			
		48 hr	0	2	73	0			
		96 hr	0	0	0	75			

This is what would be expected from an examination of the coefficient plots. When only the first two coefficients were used to generate the classifier, the error rate was only 3%. As with most of the bands, the misclassifications occurred primarily between the 24 and 48 hour samples. This is also expected when examining the coefficient plots. However, as discussed above, there is still significant separation between the samples in the third coefficient. Therefore, when the third coefficient was included in the generation of the classifier, the error rate becomes less than 2% with the misclassifications being between the 24 and 48 hour samples. Obviously, this comes from a limited sample set that was prepared in a lab environment from the same material batch so any conclusions must be qualified appropriately. Even so, the significance of this revelation to the potential development of an inspection algorithm that can be applied in the field is substantial. After demonstrating the ability of SVD to

reveal differences between the samples, the same approach was used to look for other patterns in the degradation that might have been present during the study.

4.4. Spot to Spot Variation

The primary reason for collecting data from several spots on the same sample was the uncertainty of sample uniformity across the surface and seeming difficulty in discriminating between the 24 and 48 hour treatment levels. The same approach that was used to look for trends between degradation levels was applied to each sample to determine whether the treatment was affecting the samples uniformly. As discussed in Chapter 3, this was done by analyzing each sample independently of the others. Only the $1800-850\text{ cm}^{-1}$ region was analyzed because the previous examination had already shown that the rest of the spectrum did not contain any useful information for SVD analysis. Figures 4.9-4.16 are plots of the first two coefficients by spot in the $1220-850\text{ cm}^{-1}$ and $1800-1200\text{ cm}^{-1}$ bands for sample set B. Only the plots of the first two coefficients in these bands are included here. The other coefficient plots can be found in Appendix D.

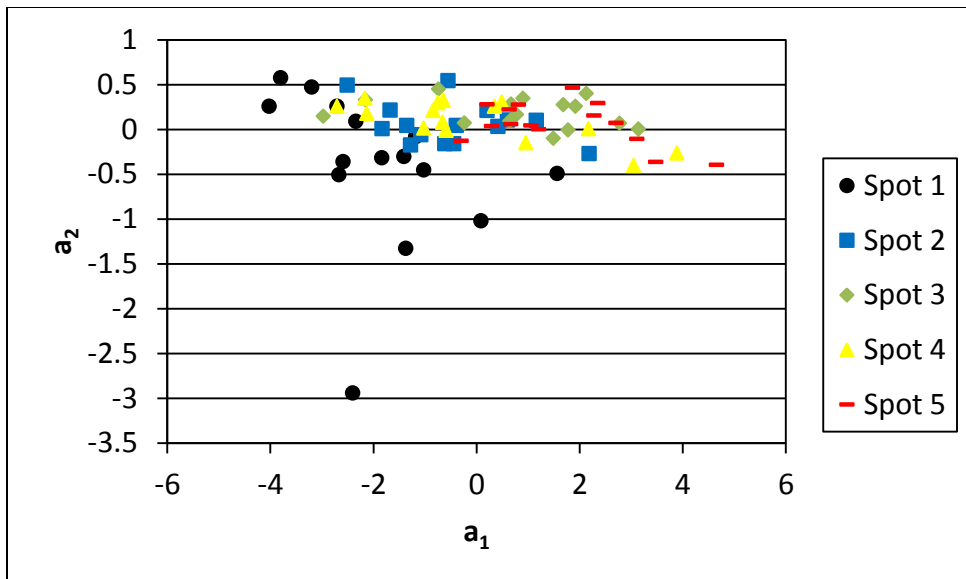


Figure 4.9: Plot of the first two coefficients for the untreated sample by spot in the $1220-850\text{ cm}^{-1}$ band. Overall, the spots have significant overlap with no separation, which is an indication of sample treatment uniformity.

In figure 4.9, the first two coefficients for the untreated sample in the $1220-850\text{ cm}^{-1}$ region are plotted. As shown in the previous section, this is the region that would be expected to reveal any differences between the spots, if there are any. With the exception of three spectra collected on spot 1 that are apparent outliers, the spots do not appear distinct from each other. The three outliers are likely the first sample collected each week and caused by collecting data while the device was still warming up as discussed in the calibration section of Chapter 3. The fact that the remainder of the spectra significantly overlap is an indication of good sample uniformity, which is expected on the untreated sample.

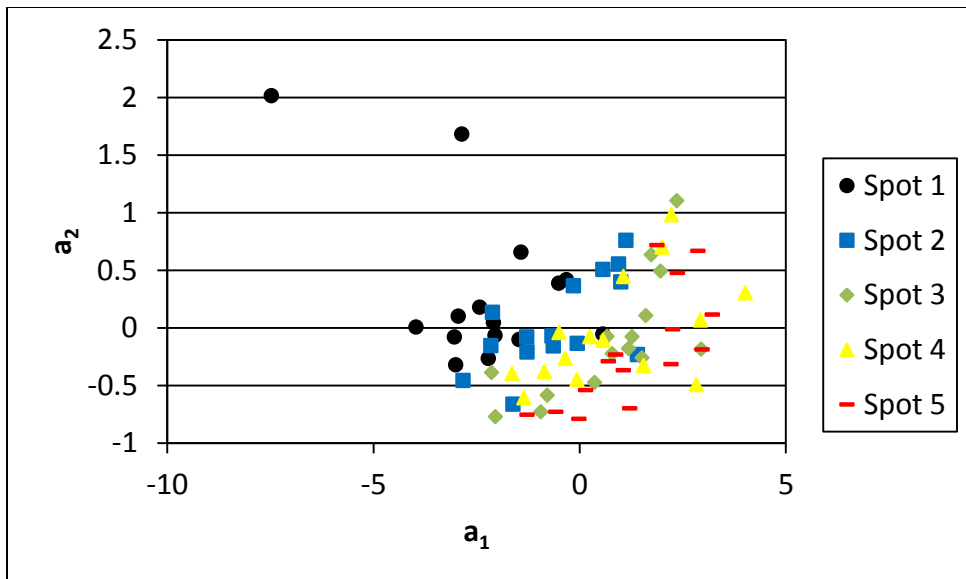


Figure 4.10: Plot of the first two coefficients for the untreated sample by spot in the $1800\text{-}1200\text{ cm}^{-1}$ band. As with the $1220\text{-}850\text{ cm}^{-1}$ band, the spots have significant overlap with no separation overall, but there is separation between spot 1 and spot 5. There is also some separation between spot 2 and spot 5 as well.

The first two coefficients for the untreated sample in the $1800\text{-}1200\text{ cm}^{-1}$ band are plotted against each other in figure 4.10. In contrast to the $1220\text{-}850\text{ cm}^{-1}$ band, this band appears to show some separation between spots 1 and 5 and 2 and 5. This would seem to indicate a chemical difference between the spots before treatment, which is again the reason that data was collected from several spots across each sample. In a field environment on an actual aircraft, there will be variability in the coating material as well as the degradation level experienced by the coating. The fact that the approach utilized during this study seems able to see through that variability, albeit in a limited sample set, and still accurately discriminate between degradation exposures demonstrates the potential for future use in the field.

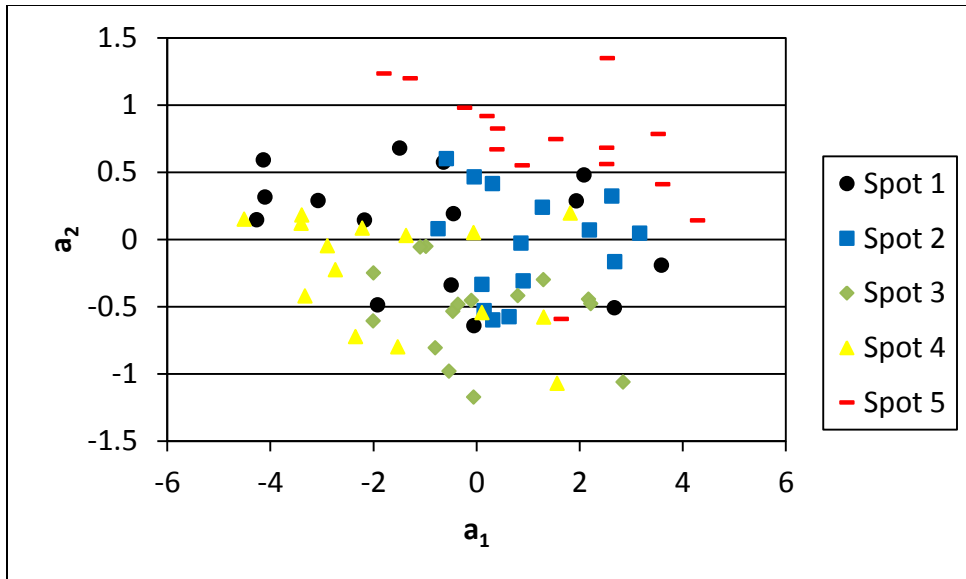


Figure 4.11: Plot of the first two coefficients for the 24 hour sample by spot in the $1220-850\text{ cm}^{-1}$ band. Unlike sample B1, this sample appears to show clustering of coefficients for spots 2-5. Qualitatively, spot 5 appears clearly separable from the rest.

Figure 4.11 is a plot of the first two coefficients for the 24 hour treatment level sample in the $1220-850\text{ cm}^{-1}$ band. While the spots are generally scattered and dispersed amongst each other, spots 2-5 are somewhat clustered together. Spot 5 is separated from the other spots, which does indicate a different level of degradation than the others. This information indicates that the coating material does not degrade evenly even though the entire sample is exposed to the same treatment conditions. It is important to remember that spots 1, 2, 4, and 5 are located in the corners of the sample and spot 3 is in the center. If the epoxy seal around the edge of the sample were not as robust in one place, it would lead to a different level of degradation being present because the heat and moisture in the autoclave could penetrate at the interface between coating and substrate.

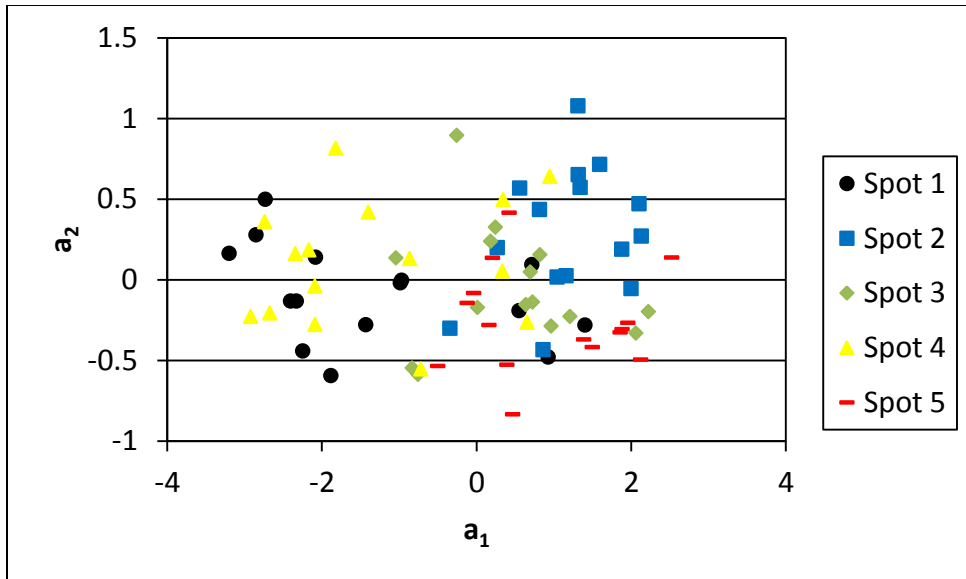


Figure 4.12: Plot of the first two coefficients for the 24 hour sample by spot in the $1800\text{-}1200\text{ cm}^{-1}$ band. This band does not appear to demonstrate the same clustering of coefficients for spots 2-5 as the $1220\text{-}850\text{ cm}^{-1}$ band. However, spots 1 and 4 seem to be separable from the rest, but not from each other.

The clustering of the first two coefficients for the 24 hour sample in the $1800\text{-}1200\text{ cm}^{-1}$ band is not as noticeable as it is in the $1220\text{-}850\text{ cm}^{-1}$ band, as shown in figure 4.12. The coefficients for spots 2, 3, and 5 would seem to indicate that this band of the spectrum cannot differentiate between them. Spots 1 and 4 are separated from the other three, but not from each other.

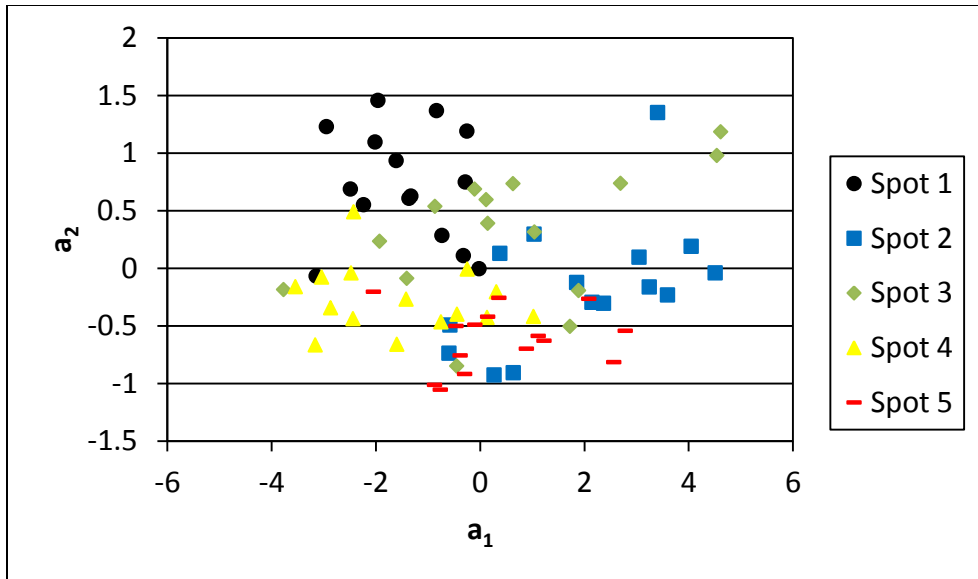


Figure 4.13: Plot of the first two coefficients for the 48 hour sample by spot in the $1220-850\text{ cm}^{-1}$ band. While there is overlap between spots, spot 1 is separable from spots 2, 4, and 5 and spot 2 is mostly distinct from spot 4.

The spots on the 48 hour sample show more clustering and separation in the $1220-850\text{ cm}^{-1}$ band than the 24 hour sample, as seen in figure 4.13. Spot 1 is distinct from spots 2, 4, and 5 but shows significant overlap with spot 3. Spots 2 and 4 are distinct from each other as well. It is interesting that spot 3, the center spot on the sample, is mixed in with all the other spots. A potential explanation of this is that the corner spots degraded at different levels from each other, but the center of the sample shows a similar level of degradation as all four corners. In other words, the four levels of degradation in the corners seem to converge at the center of the sample.

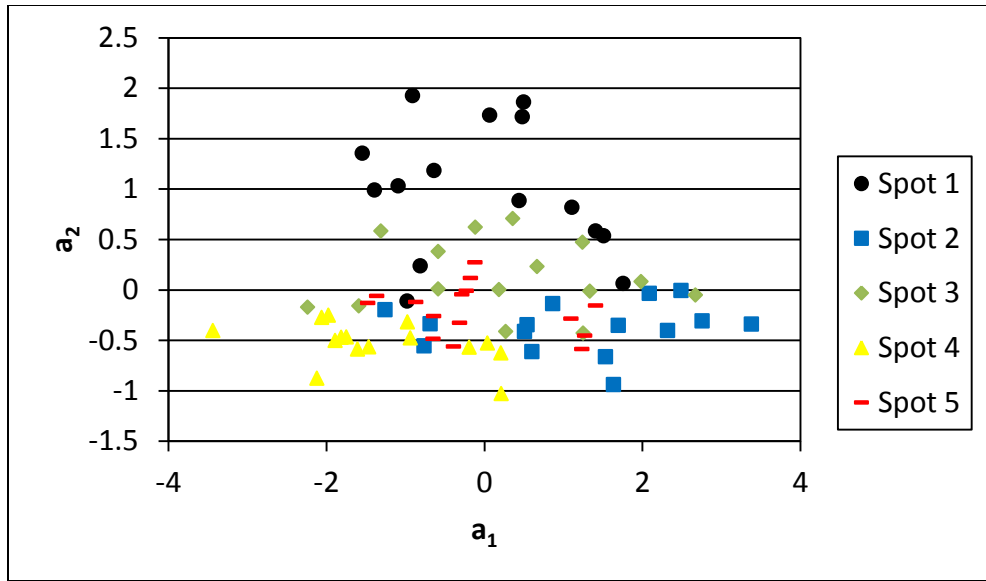


Figure 4.14: Plot of the first two coefficients for the 48 hour sample by spot in the $1800-1200\text{ cm}^{-1}$ band. This band demonstrates clustering of coefficients similar to the $1220-850\text{ cm}^{-1}$ band. The locations of the spots in the a_1 vs. a_2 plane are even similar in relationship to each other.

The plot of the first two coefficients for the 48 hour sample in the $1800-1200\text{ cm}^{-1}$ band shown in figure 4.14 also shows some separation between spots like the $1220-850\text{ cm}^{-1}$ band. Spot 1 is clearly distinct from the other spots and spot 2 is distinct from spot 4. Spots 3 and 5 are centered between spots 1, 2 and 4 which would seem to indicate similarities between them. Interestingly, when the relationship of the spots in the a_1 vs. a_2 plane in the $1800-1200\text{ cm}^{-1}$ band are compared to the same in the $1220-850\text{ cm}^{-1}$ band, there is high similarity. Spot 1 is high on the a_2 axis with spot 3 just below it while spots 4, 5, and 2 progress left to right along the a_1 axis, respectively.

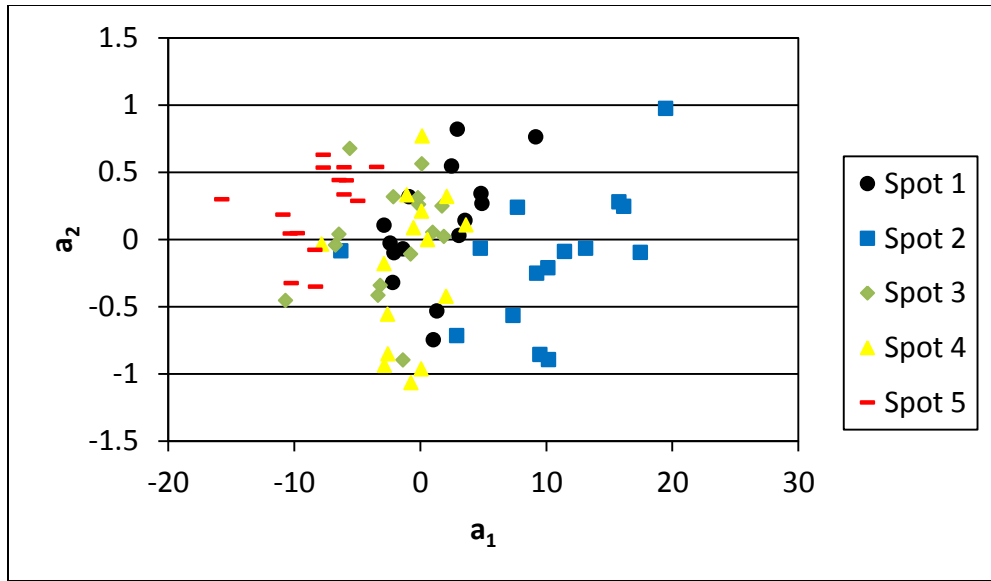


Figure 4.15: Plot of the first two coefficients for the 96 hour sample by spot in the $1220-850 \text{ cm}^{-1}$ band. Spots 2 and 5 are distinct from each other and the other spots. Spots 1, 3, and 4 show significant overlap, which indicates they experienced same treatment level.

In the $1220-850 \text{ cm}^{-1}$ band for the 96 hour sample, spots 2 and 5 are clearly different from each other and the other spots on the sample, as shown in figure 4.15. Spots 1, 3 and 4 are all on top of each other in this band, suggesting they experienced the same level of degradation during the treatment. Unlike the other samples in set B, the 96 hour sample had significant wrinkling of the coating material across its surface that originated around the edges. It is likely that the differences between the spots in this band are a result of the chemical reaction that led to the wrinkling of the coating in some places and not others.

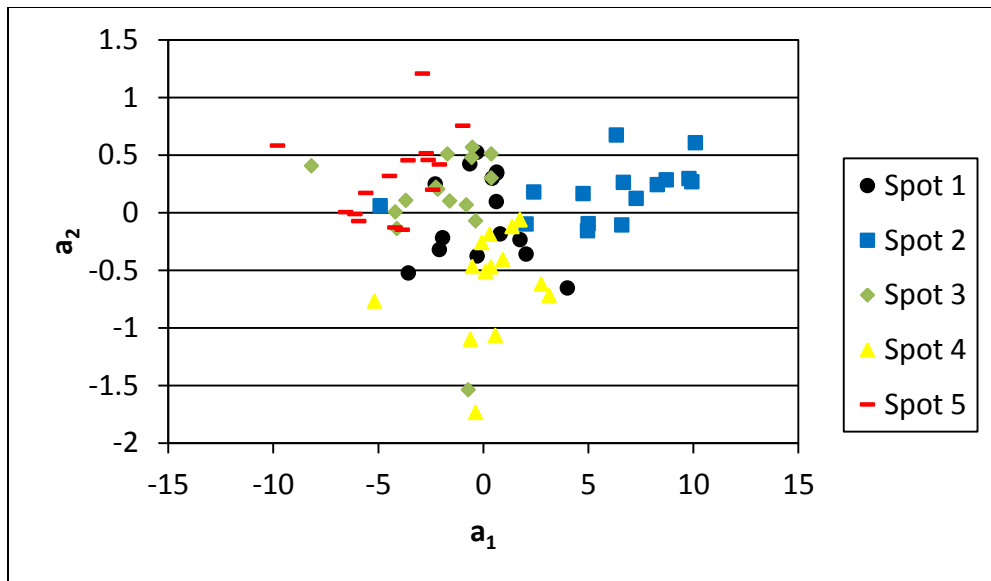


Figure 4.16: Plot of the first two coefficients for the 96 hour sample by spot in the $1800\text{-}1200\text{ cm}^{-1}$ band. While the coefficients all overlap each other, each spot appears to be distinguishable from at least one other spot.

Just like in the $1220\text{-}850\text{ cm}^{-1}$ band of the 96 hour sample, spots 2 and 5 are clearly distinct from each other while spots 1, 3, and 4 are similar to each other in the $1800\text{-}1200\text{ cm}^{-1}$ band, as shown in figure 4.16. Also, like the 48 hour sample, the relationship between the spots in the a_1 vs. a_2 plane is the same in both bands.

4.5. Time-dependent Behavior

The other investigation that was conducted on the samples using the SVD coefficients was to look into whether or not there was any time-dependent behavior to the degradation. The root cause investigation team that started this study observed that samples that were shipped from the field to the lab for examination would arrive in a mild state of visible degradation, but became severely degraded in a matter of days. This observation is what led to the decision to collect data over several weeks so that week to week data could be compared. As discussed in Chapter 2, one of the sources of

degradation in polymers is physical aging. Physical aging is a time-dependent relaxation of the polymer chains, but it is not a chemical reaction. While this makes detecting the change difficult with FTIR because the molecular combinations are not changing, it might be possible to detect changing bond structures that would lead to different vibrational modes. As in the previous section, only the plots of interest are shown here. The remaining plots are included in Appendix D for completeness. With the exception of figure 4.22, figures 4.17-4.24 are the plots of the first two coefficients in the 1800-1200 and 1220-850 cm^{-1} bands for the four samples in set B. Figure 4.22 is a plot of the first and third coefficients in the 1800-1200 cm^{-1} band for sample B3, the 48 hour treatment sample, because it does show some trending week to week. Overall, there is significant overlap of the coefficients which is an indication that there is no significant time dependent behavior in the samples. While the data is not sufficient to conclusively rule out the presence of physical aging or a continuing reaction, it does indicate the primary degradation mechanism in this sample set is the heat and moisture exposure used to artificially age the samples.

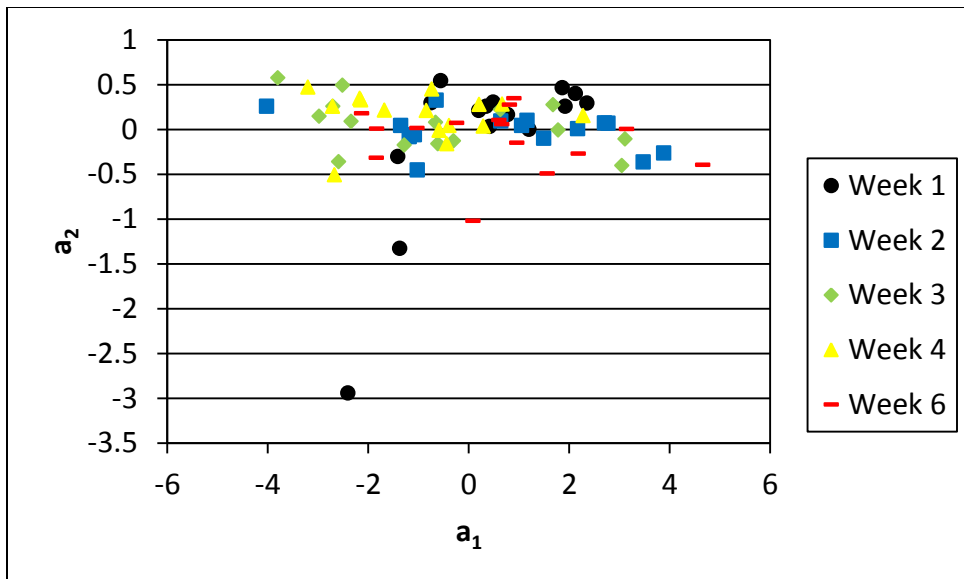


Figure 4.17: Plot of the first two coefficients comparing week to week data for the untreated sample in the $1220-850\text{ cm}^{-1}$ band. There is significant overlap with no separation between the weeks, which indicates there is little or no time dependent behavior to the degradation.

The first two coefficients plotted by week in the $1220-850\text{ cm}^{-1}$ band for the untreated sample is shown in figure 4.17. As would be expected for the untreated sample, there is no week to week trend in the data. Whatever reaction is taking place in the treated samples caused by the heat and moisture exposure was not initiated in the untreated sample, so the only potential time dependent behavior would be physical aging. Figure 4.17 indicates that either there is no time dependent behavior or FTIR is unable to detect it.

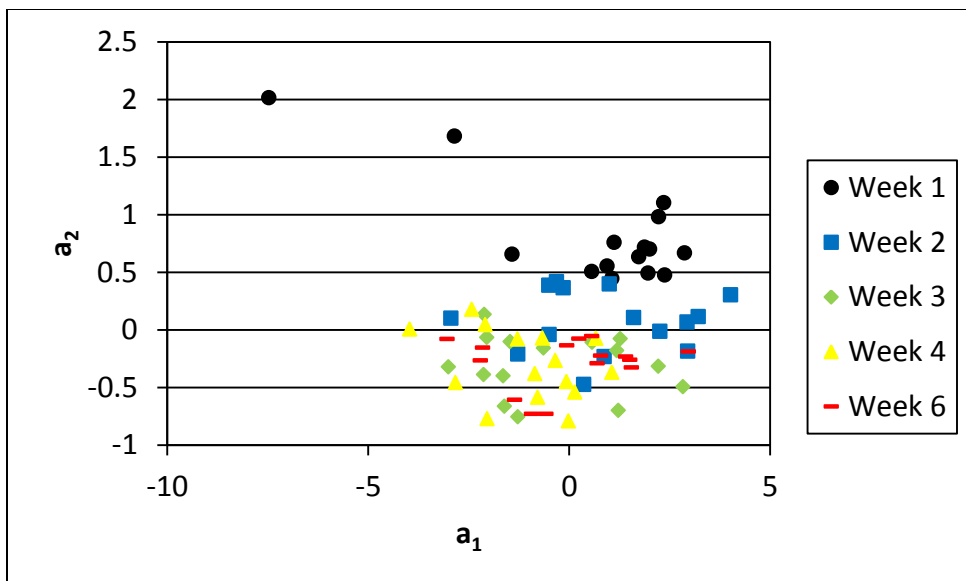


Figure 4.18: Plot of the first two coefficients comparing week to week data for the untreated sample in the $1800-1200\text{ cm}^{-1}$ band. There is some progression from week one to week two along the a_2 axis, but there remains significant overlap in weeks 3, 4, and 6.

Unlike the $1220-850\text{ cm}^{-1}$ band for the untreated sample, the $1800-1200\text{ cm}^{-1}$ band does demonstrate some progression from the first to the second week, as shown in figure 4.18. The progression is subtle, which suggests that little, if anything, has actually changed in the coating material. There is no trending from weeks three through six, which combined with the data in the $1220-850\text{ cm}^{-1}$ band, further supports the idea that nothing actually changed from week to week in the untreated sample as expected. Again, it must be noted this is not conclusive evidence one way or the other, but it is a strong indication considering the ability of the approach to discern functional differences in the material.

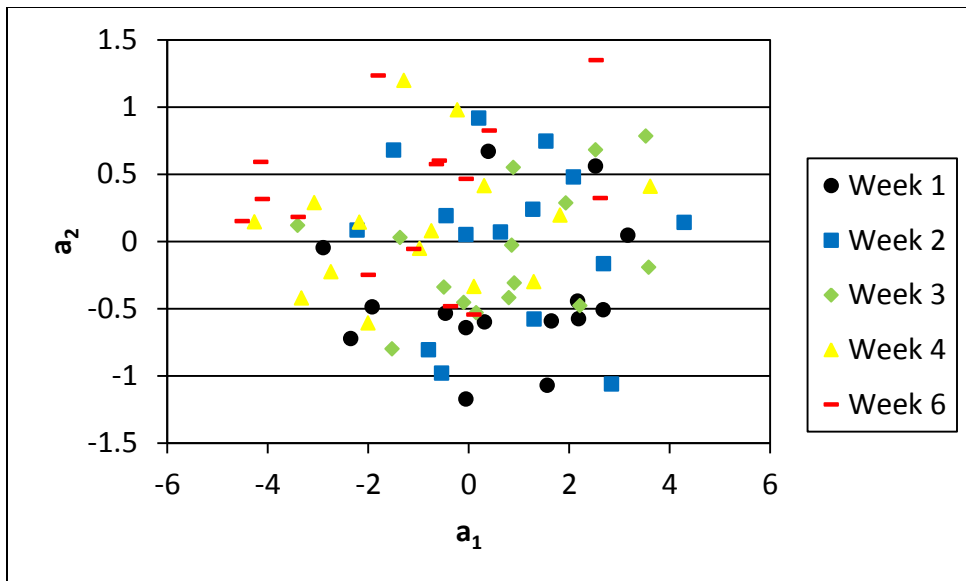


Figure 4.19: Plot of the first two coefficients comparing week to week data for the 24 hour sample in the $1220-850\text{ cm}^{-1}$ band. There is no separation or trend from week to week, again indicating no time-dependent behavior for this sample visible in this band.

A plot of the first two coefficients for the $1220-850\text{ cm}^{-1}$ band taken on the 24 hour treatment sample does not reveal any week to week trend in the coating, as shown in figure 4.19. The coefficients are scattered and evenly distributed for all weeks of sampling indicating that there is no time dependent change taking place that is detectable in this band of the spectrum. Additionally, examination of the plots of the other coefficients for the same band in Appendix D reveals an equally scattered distribution of the spectra. Taken in total, it is unlikely there is a functional change in the material taking place over time.

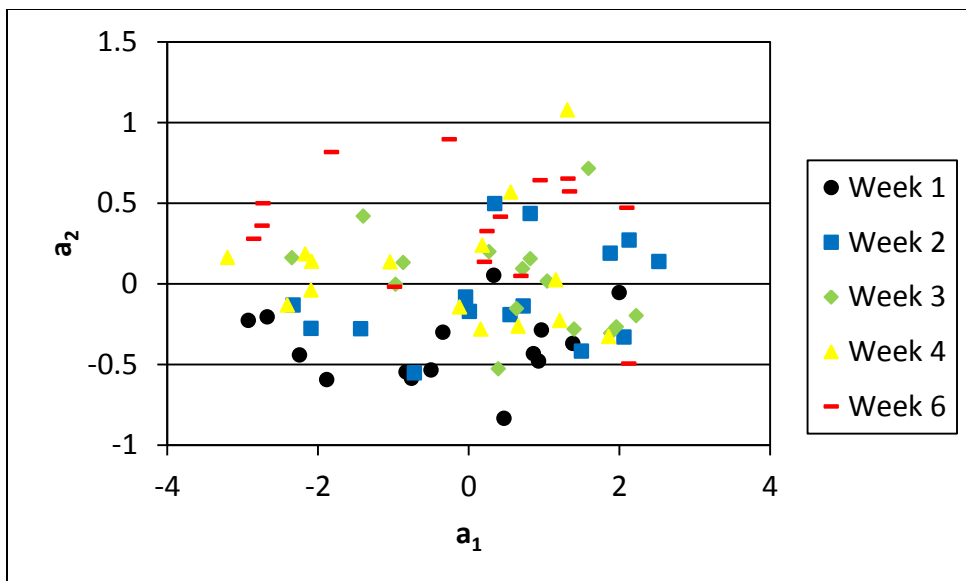


Figure 4.20: Plot of the first two coefficients comparing week to week data for the 24 hour sample in the $1800\text{-}1200\text{ cm}^{-1}$ band. Just like in the $1220\text{-}850\text{ cm}^{-1}$ band, there is no clear separation or trend from week to week. There is some separation between week one and week six, but weeks 2-4 are still mixed in with no clear trend between them.

A plot of the first two coefficients derived from the $1800\text{-}1200\text{ cm}^{-1}$ band for the 24 hour treatment also show no trending from week to week, as shown in figure 4.20. There is separation between the first and sixth week data, but the other weeks are scattered throughout with no trend connecting them. It could be that from week one to week six, something changed about the material or it could be the result of some other phenomenon that contributed to the difference. When the results of the $1220\text{-}850\text{ cm}^{-1}$ band are combined with the lack of a trend in the interim weeks, it seems that there is another explanation for the difference between weeks one and six rather than time-dependent behavior.

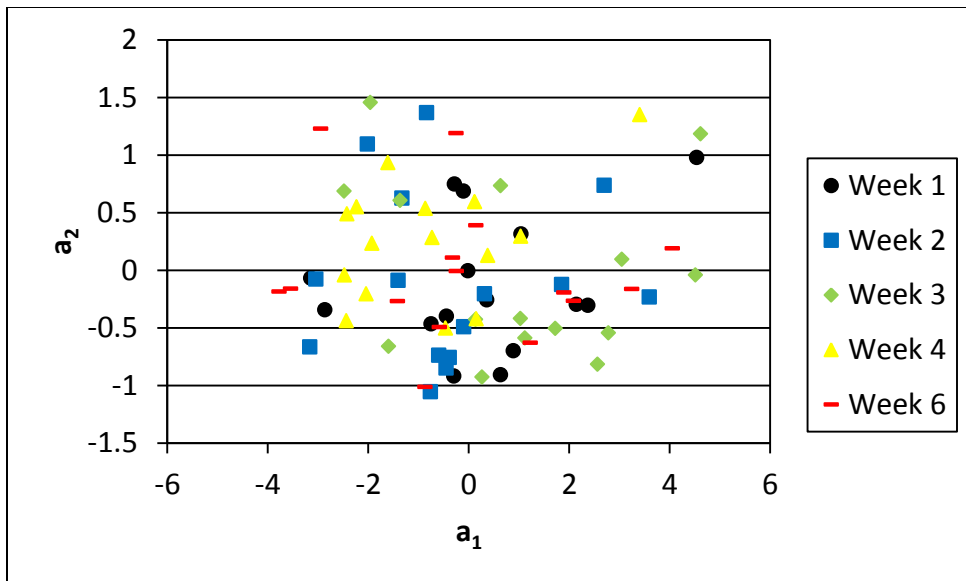


Figure 4.21: Plot of the first two coefficients comparing week to week data for the 48 hour sample in the $1220-850\text{ cm}^{-1}$ band. There is no separation or trend from week to week, again indicating no time-dependent behavior for this sample visible in this band.

Just as with the 24 hour sample, there is no pattern from week to week in the coefficients for the 48 hour sample in the $1220-850\text{ cm}^{-1}$ band in figure 4.21. The coefficients are scattered and evenly distributed amongst each other. This is more evidence against time-dependent changes in the material, but is still not conclusive. Again, there could be something that changes in the material, but it is not detectable using this approach in this band of the spectrum.

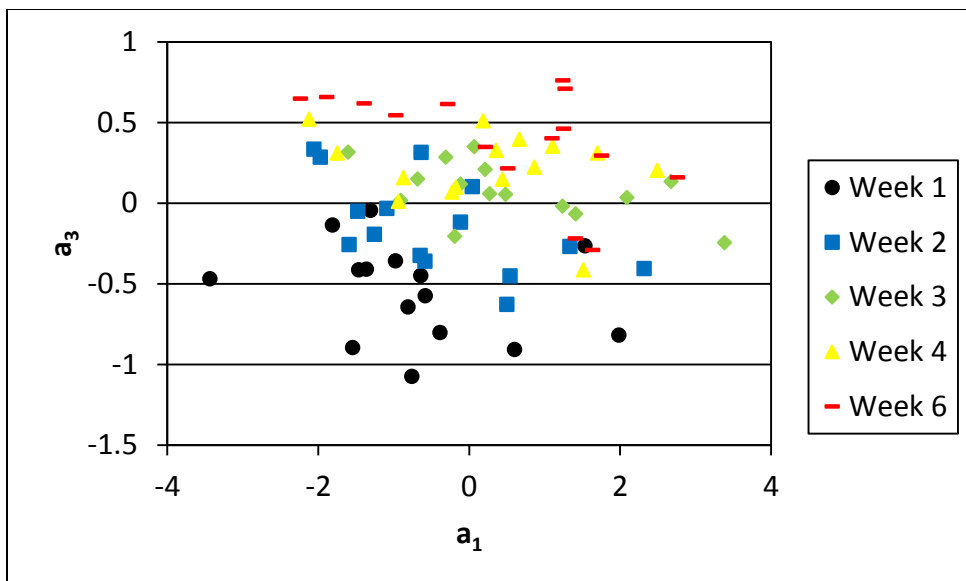


Figure 4.22: Plot of the first and third coefficients comparing week to week data for the 48 hour sample in the $1800-1200\text{ cm}^{-1}$ band. Interestingly, there is some progression from week to week in the first and third coefficients in this band. This is the only sample and band to demonstrate that behavior.

Figure 4.22 is a plot of the first and third coefficients in the $1800-1200\text{ cm}^{-1}$ band for the 48 hour sample rather than the first two coefficients. When examining the coefficient plots, this plot showed some trending from week to week where the first two coefficients showed none. The progression from week to week is subtle like the $1220-850\text{ cm}^{-1}$ band of the untreated sample, but it is visible. Week one to week two is clearly visible while the remaining weeks are less so. As explained in the discussion about the untreated sample, this could indicate a time-dependent change or not. The progression does not show up in the $1220-850\text{ cm}^{-1}$ band and is not visible in the first two coefficients, which would indicate it is not a functional change in the material. However, it is inconclusive and a different characterization technique, or combination of techniques, would have to be applied to verify whether or not something is changing.

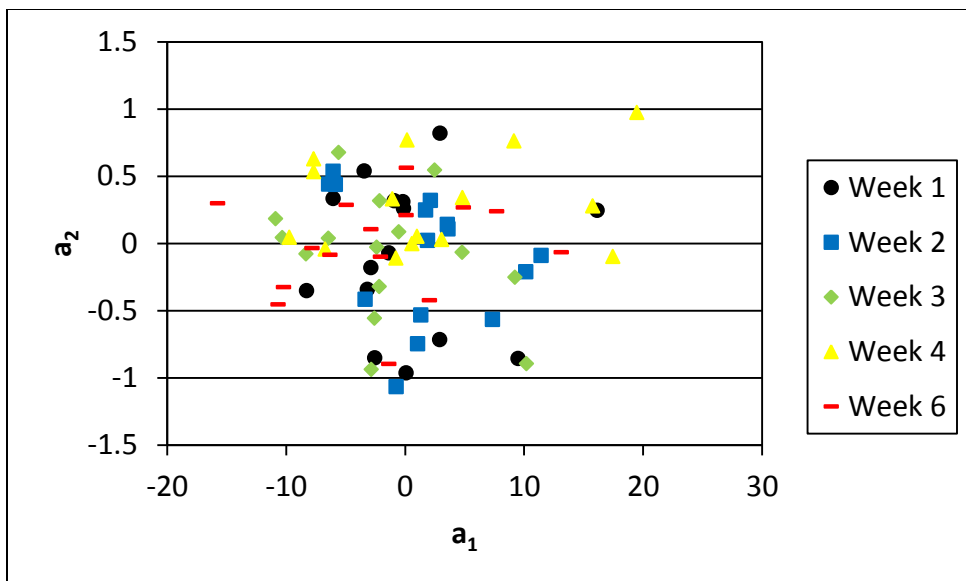


Figure 4.23: Plot of the first two coefficients comparing week to week data for the 96 hour sample in the $1220-850\text{ cm}^{-1}$ band. There is no separation or trend from week to week, again indicating no time-dependent behavior for this sample visible in this band.

Just like the other samples, a plot of the first two coefficients for the 96 hour sample in the $1220-850\text{ cm}^{-1}$ band does not reveal any week to week trends, as shown in figure 4.23. The spectra are scattered and distributed evenly amongst each other with no separation. This is more evidence to support the idea that either nothing functional changed in the sample over the six weeks of data collection or this approach is incapable of detecting it.

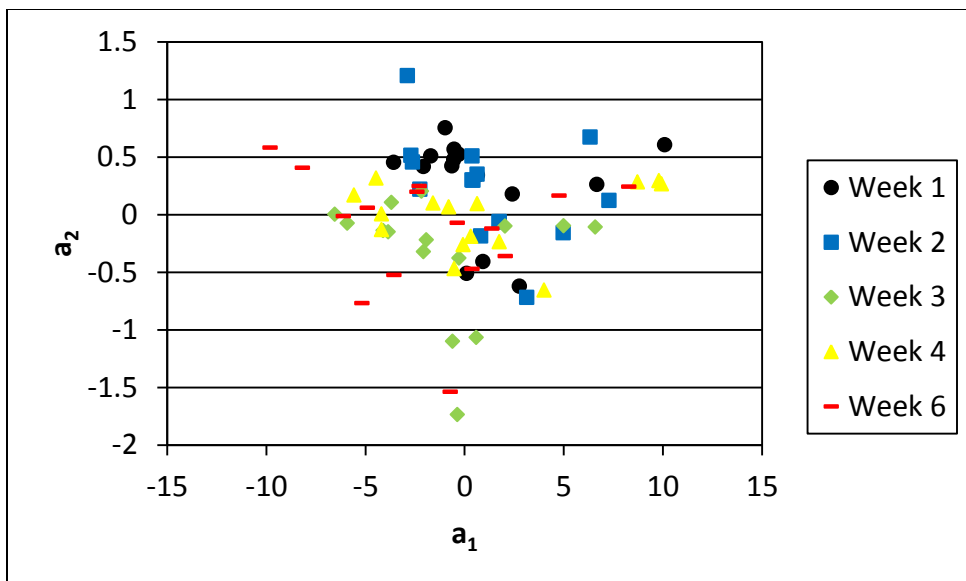


Figure 4.24: Plot of the first two coefficients comparing week to week data for the 96 hour sample in the $1800\text{-}1200\text{ cm}^{-1}$ band. There is no separation or trend from week to week, again indicating no time-dependent behavior for this sample visible in this band.

Finally, a plot of the first two coefficients for the 96 hour sample in the $1800\text{-}1200\text{ cm}^{-1}$ band also shows no trend from week to week shown in figure 4.24. The spectra are scattered and distributed just like in the $1220\text{-}850\text{ cm}^{-1}$ band and the majority of the plots for the other samples. Considering the plots of the coefficients covering both bands for all four samples in set B examined during this analysis, there are two possible explanations. As discussed earlier in this section, either there was no time-dependent change in the samples during data collection or this approach is unable to detect it. It could be that six weeks was not enough time to allow a functional change to take place, but that seems unlikely considering the observations made by the root cause team on the fielded samples. It could also be that any time-dependent change in the material is not visible to the bands of the IR spectrum that were analyzed. However, visual inspections of the samples each week did not reveal any change in appearance of the

surface of the samples. Though it cannot be stated conclusively without further testing, all indications are that there was no time-dependent change in the samples used for this study and the degradation of the material is the result of the heat and moisture treatment they were exposed to.

4.6. Classifying New Sample Data

After showing that the varying degradation levels are detectable, the final step in validating the potential of this approach is classifying new sample data correctly. Due to time and sample quantity limitations, sample set A was used for the purpose of demonstrating the ability to correctly classify new sample data. Sample set A is a different coating combination than sample set B; however, it is a fielded top coat combination. Sample set A is comprised of two untreated samples and two samples treated to a visibly degraded level. There are no intermediate levels of degradation to attempt to classify. This makes it ideal for a rudimentary test of the approach and its ability to correctly classify new samples. One untreated sample and one visibly degraded sample were used to generate the classifier and the other two samples used as new data. For the analysis of sample set B, discriminant analysis was used to quantitatively determine which band of the spectrum provided the best discrimination between samples. For sample set A, it was used to classify unknown samples. This is an important demonstration to make if the Air Force is to pursue this approach as an inspection.

The process used for this work was slightly different than what was used to analyze the samples in set B. In this case, data was only collected for two consecutive

days immediately after the samples were treated, so the sample size is smaller. Instead of performing the SVD analysis on all sample data collectively and including all sample coefficients in the development of the LDA classifier, the SVD analysis was conducted on one untreated and one treated sample as a pair to develop the new classifier. The pair of samples representing new data was analyzed separately from the training set. As with sample set B, the first step is an examination of the mean reflectance of the four samples in set A. Figure 4.25 reveals that the two untreated samples are nearly identical and the two treated samples are distinctly different from the untreated samples and each other.

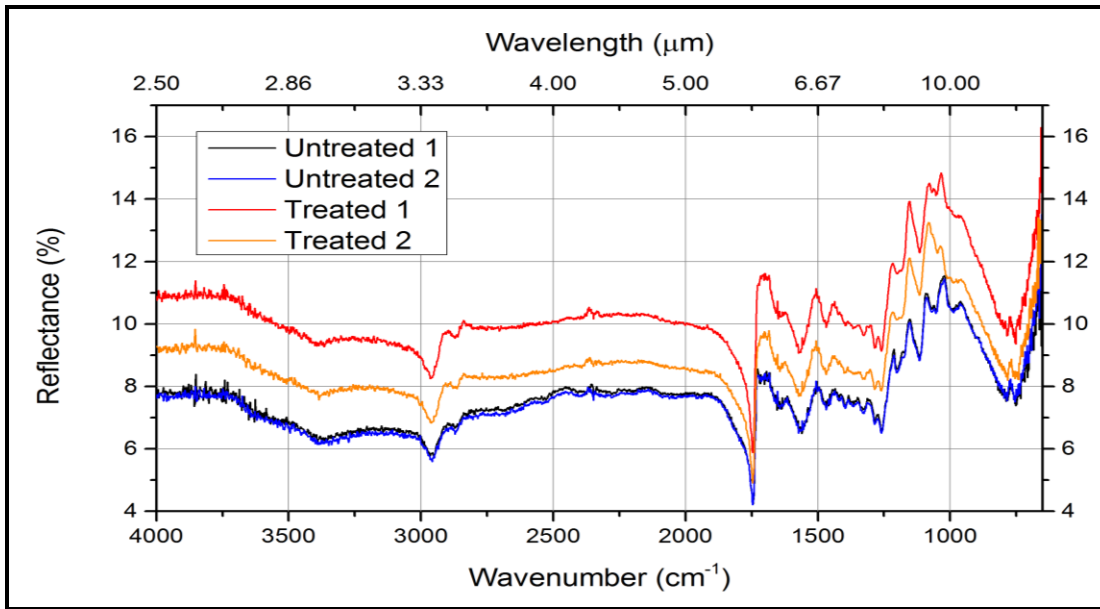


Figure 4.25: A plot of the mean reflectance of the four samples in set A collected the first day. The two untreated samples lie almost on top of each other while the treated samples have a higher mean reflectance over the entire spectrum.

The two samples used as the training set to generate the classification rule were samples A1 and A3. Samples A2 and A4 were used as new data for classification. There were four classification rules developed and compared. The first two classifiers were generated using the entire sampling spectrum. One classification rule was developed using the first two coefficients and one rule developed using the first three coefficients. The other two classifiers were generated using only the fingerprint region of the spectrum. Again, one rule was developed using the first two coefficients and one rule using the first three coefficients.

4.6.1. Classification using Entire Sampling Spectrum.

Since this is a two-class system and the reflectance spectra are so distinct, sample classification was first attempted using the entire sampling spectrum. The SVD coefficients from the training set generated very distinct clusters in the plot of the first

two coefficients, as shown in figure 4.26. Additionally, the classification line computed by the `ClassificationDiscriminant.fit` function in MATLAB is plotted in figure 4.26 in order to show how it will predict new data.

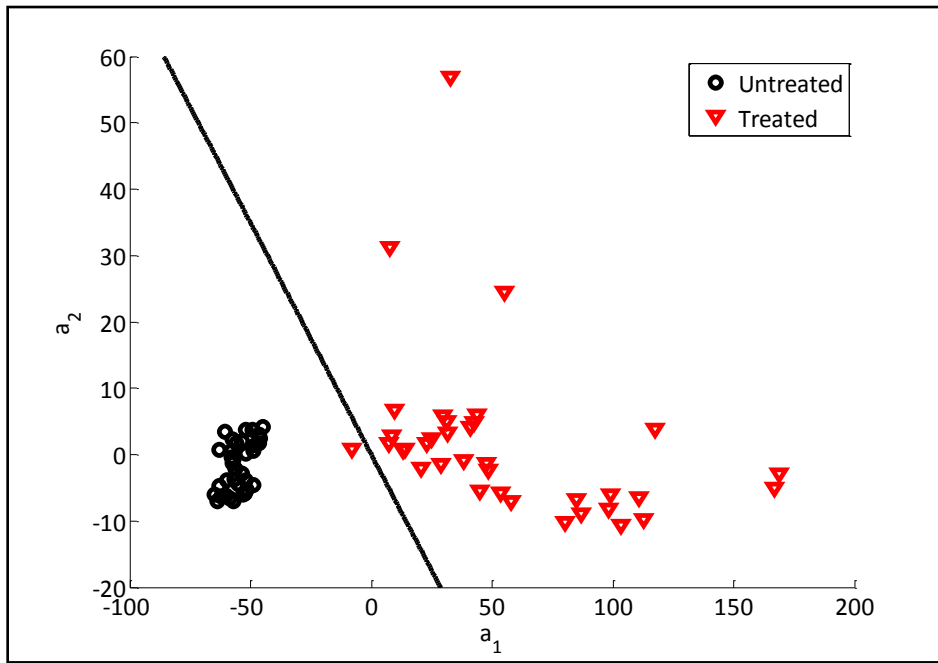


Figure 4.26: A plot of the first two SVD coefficients for the untreated and treated samples generated using the entire sampling spectrum. The classification line computed by MATLAB is also plotted to show how it will predict new data.

The new data set was then projected onto the basis generated from the training set. In order to do this, the mean of the training set was subtracted from the new data set before the SVD analysis was conducted. Figure 4.27 is a plot of where the new sample coefficients are in relation to the training set coefficients. A quick examination of figure 4.27 suggests that the classification rule will likely classify the new untreated sample 100% correctly, but misclassify many of the treated samples.

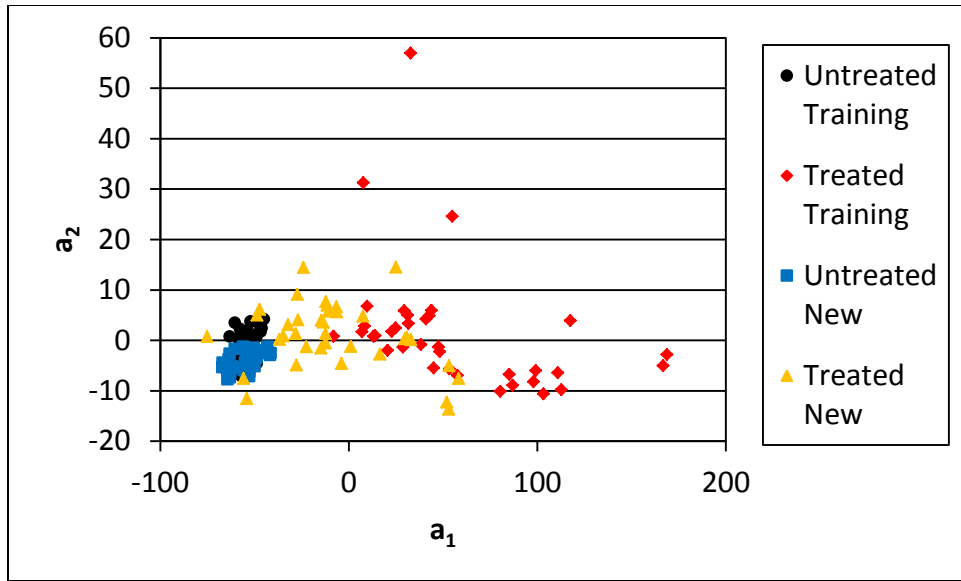


Figure 4.27: A plot of the first two SVD coefficients for both pairs of treated and untreated samples from set A using entire sampling spectrum. The black and red dots are the coefficients used to generate the classification rule and the blue and orange dots are the coefficients that the rule attempted to classify. Based on the plot, it was predicted that the rule would misclassify some of the treated samples in the lower left of the plot as untreated.

Like before, the accuracy of the classifier was examined using re-substitution error and cross-validation. Table 4.3 is a summary of the results of the re-substitution error and k-fold cross-validation of the rule. As expected, the accuracy of the classification rule is high.

Table 4.3: Confusion matrix and error rates for the classifier developed using the first two and first three SVD coefficients from one untreated sample and one treated sample in set A.

Entire Spectrum	Predict \ Truth	Untreated	Treated	Re-substitution error %	Number of Errors (#/72)	k-fold Error (10 fold) %
2 Coefficients	Untreated	36	0	1.39	1	1.39
	Treated	1	35			
3 Coefficients	Untreated	36	0	0	0	0
	Treated	0	36			

When the SVD coefficients generated from the new sample data are input into the classification rule for prediction, the classifier performs as expected from figure 4.27.

When only the first two coefficients are used for classification, the classifier correctly assigns all 36 untreated new samples, but only 12 of the new treated samples for an accuracy of 33%. The performance of the classifier is improved slightly when using the first three coefficients. Again, the classifier correctly assigns all 36 untreated samples. The classifier correctly assigns 17 of the new treated samples for an accuracy of 47%.

4.6.2. Classification using the Fingerprint Region.

After the classification of new sample data using the entire sampling spectrum generated unacceptably high error rates, classification was attempted using only the fingerprint region of the spectrum. As discussed in Chapter 2 and shown with sample set B, the fingerprint region produces the most discrimination between samples. Figure 4.28 is a plot of the first two SVD coefficients of the training set generated from the fingerprint region along with the classification line computed by MATLAB using the ClassificationDiscriminant.fit command.

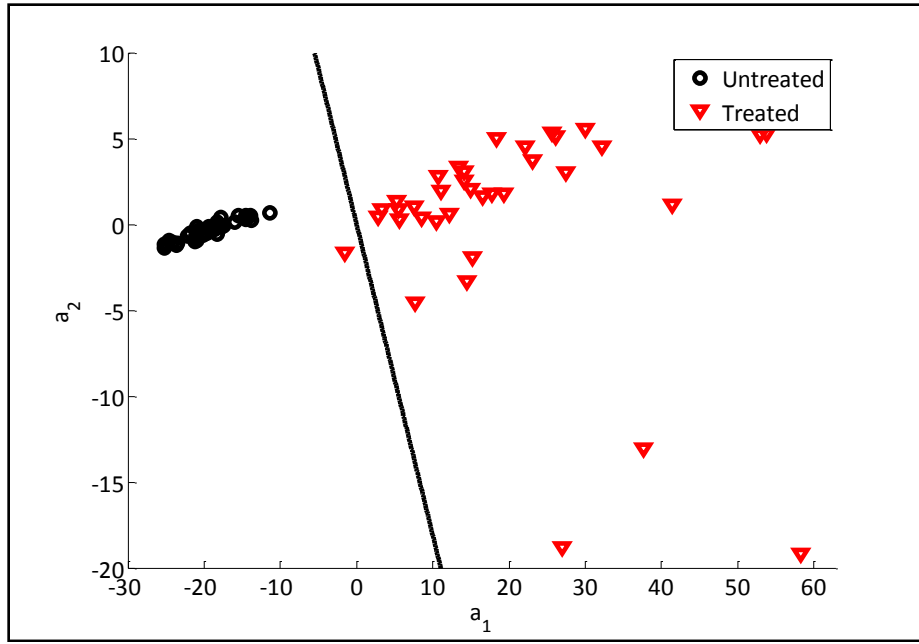


Figure 4.28: A plot of the first two coefficients for the untreated and treated samples used to generate the classification rule in the fingerprint region. The classification line computed by MATLAB is also included to show how it will predict new data.

The two samples are clearly distinct and would be expected to generate a highly accurate classifier. When the first two coefficients of the new sample data are plotted with the training data in figure 4.29, it appears that the fingerprint region will again be highly accurate at classifying the new sample data as shown with sample set B. The new untreated sample is on top of the untreated sample used for training and the new treated sample is clearly distinct from the untreated samples.

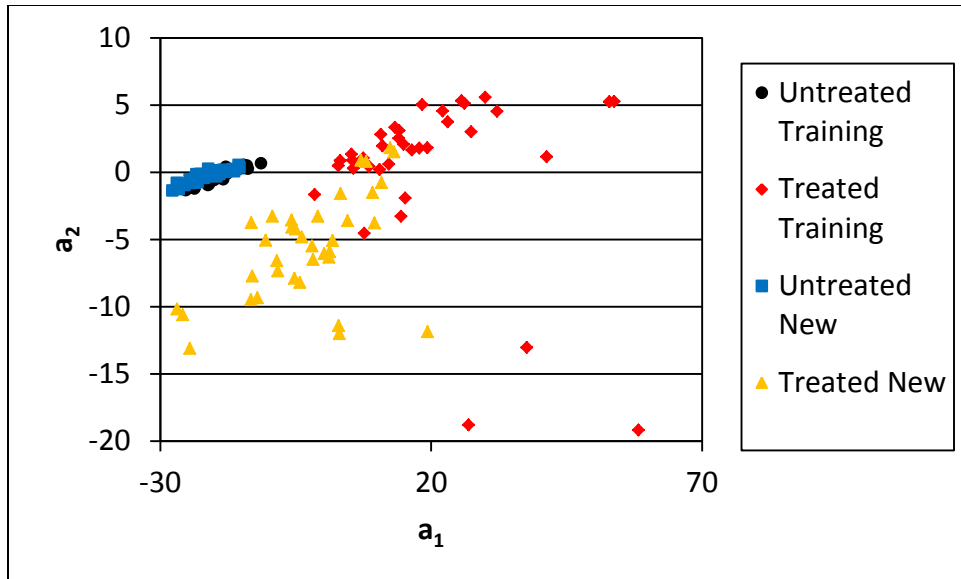


Figure 4.29: A plot of the first two coefficients generated from the fingerprint region for both the training set and the new data set for prediction. The new untreated sample is on top of the untreated sample used for training and the treated sample is clearly distinct from the untreated samples.

As before, two classification rules were generated using both the first two and first three coefficients. Table 4.4 is the confusion matrix and error rates of the re-substitution error and cross-validation error analyses for the classification rule. As expected from figure 4.28, both rules are highly accurate.

Table 4.4: Confusion matrix and error summary of the classification rules generated for the fingerprint region using the first two and first three coefficients. As expected, both classifiers are highly accurate.

Fingerprint Region	Predict Truth \	Untreated	Treated	Re-substitution Error %	Number of Errors (#/72)	k-fold Error (10 fold) %
2 Coefficients	Untreated	36	0	1.39	1	1.39
	Treated	1	35			
3 Coefficients	Untreated	36	0	0	0	0
	Treated	0	36			

When the coefficients from the new data set were input into the classification rule for prediction, the misclassification rate was unexpectedly high. Using the first two coefficients for classification, the rule still correctly assigned all 36 untreated samples. However, only 10 of the treated samples were correctly classified for an accuracy of 28%. When the first three coefficients were input for classification, the rule again correctly assigns all 36 untreated samples, but only correctly assigned one treated sample. It was shown with sample set B that using the first three coefficients generally increases the accuracy of the model, so it was expected to do the same here. An examination of figure 4.30 gives some insight into a possible explanation of this apparent contradiction. Figure 4.30 is a plot of the second and third coefficients, with the second coefficient on the vertical axis and the third coefficient on the horizontal axis for a direct comparison with figure 4.29.

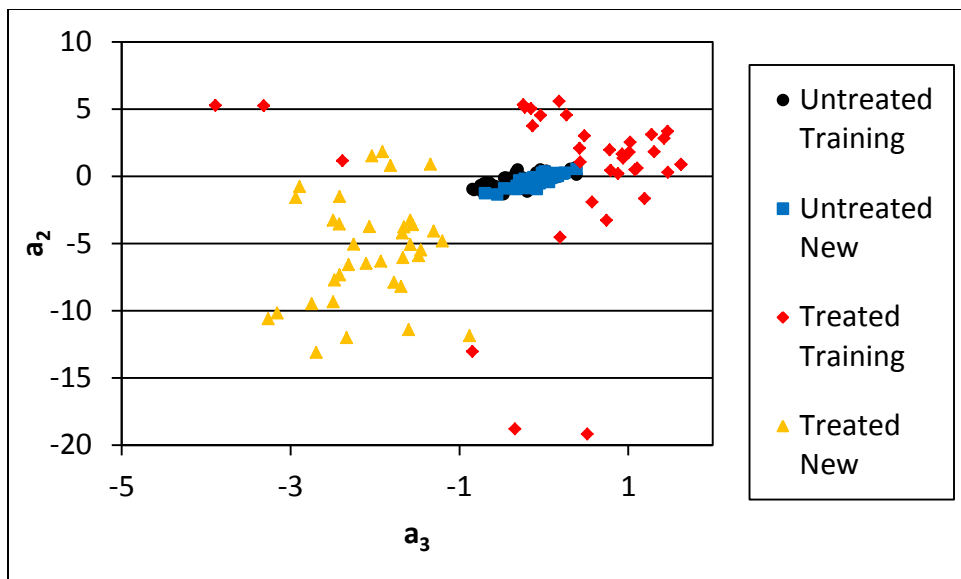


Figure 4.30: A plot of the second and third coefficients generated from the fingerprint region for sample set A. The treated samples are on opposite sides of the untreated sample along the a_3 axis leading to high misclassification rates when all three coefficients are used.

The two treated samples are on opposite sides of the untreated samples along the third coefficient axis. Since this is a two class system, the classification rule draws a line in two dimensions, or a plane in three dimensions, between the two classes. Any new data points that fall on one side or the other of the rule, is classified accordingly. Using three coefficients in the fingerprint region of this sample set actually worsens the prediction rate of the classification rule. Going back to the decision rule generated using only the first two coefficients in the fingerprint region, it still did not perform as well as expected. There are two ways to improve the accuracy of a linear discriminant. One is to adjust the prior probabilities of the training set. In this case, that is not helpful because the default is 50% prior probability in MATLAB and that is what is seen in the sample set distribution anyway. The other way to improve the accuracy is to adjust the cost of misclassification. If it is determined that the cost of misclassifying one category

as another is higher than the alternative, it can be input into classification rule calculation and it will reduce misclassification in that direction. The tradeoff is that the classification rule will misclassify in the other direction. In this case, if the cost of misclassifying a treated sample as untreated is higher than vice versa, the line shifts towards the untreated sample cluster to classify more treated samples as treated, as shown in figure 4.31. If the line shifts too far, it will misclassify untreated samples as treated. This was done with the two coefficient classifier to improve the accuracy.

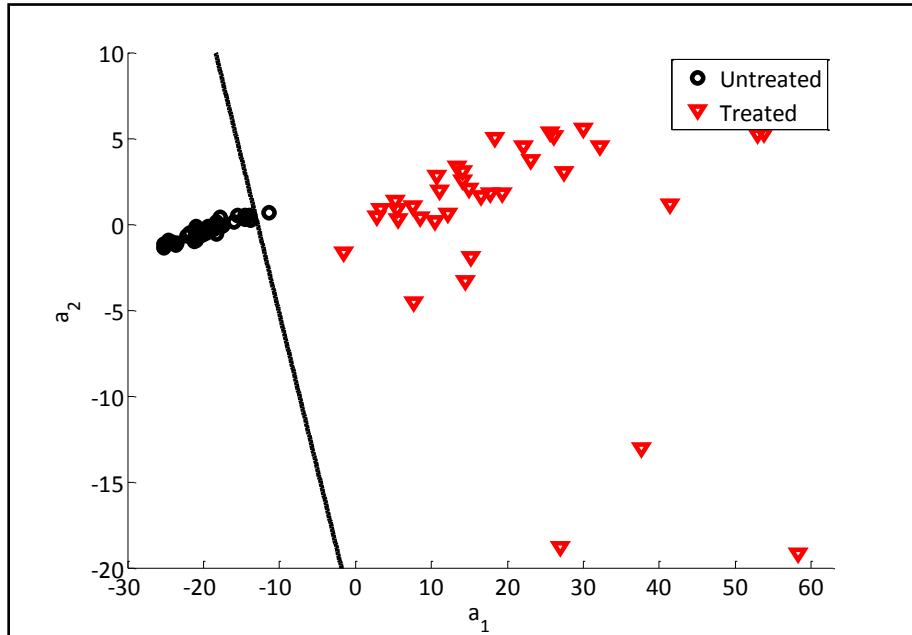


Figure 4.31: Plot of the first two coefficients of the training set along with the classification line after the cost of misclassification was adjusted to improve classification rates of the treated sample. Note how the classification line has the same slope, it has just shifted towards the untreated samples to include more treated samples on the treated side of the line.

The cost was set to 100 and the results did improve. The adjusted classification rule still correctly assigned all 36 untreated samples, but now correctly assigns 28 of the new treated samples for an accuracy of 78%. This is much improved over the 28% accuracy

before adjusting the cost; however, the classifier still does not achieve 100% accuracy as expected from an examination of figure 4.29.

This demonstration of new sample classification has highlighted several interesting points. First is the weakness of two-class classification with a small sample set. With a limited sample size, any deviation of the new data from the training data will lead to high misclassification as seen when trying to predict the new treated sample. Related to that point is the need for a substantial amount of training data if this approach is used to develop an inspection for the field. A high number of samples in many degradation levels need to be used to generate the classification rule so that the variations in fielded coatings can be accurately captured. Finally, any samples used to generate the classification rule will need to be in the correct layer configuration. A classification rule based on the configuration used in sample set B could not be expected to accurately score the samples in set A and vice versa. These are only two of the many fielded configurations of coating layers and a scoring system would have to be established for each one.

V. Conclusions

5.1. Accomplishments

The primary objective of this research was to investigate whether or not a handheld FTIR device, taking diffuse reflectance measurements, could detect and differentiate between varying levels of degradation in polyurethane aircraft coating materials. To that end, several samples were generated using the same materials in the same layer configuration as are applied to fielded aircraft. The samples were subjected to heat and moisture in an autoclave for different lengths of time to generate samples with varying levels of degradation. A commercial handheld FTIR device was used to collect IR spectra on those samples over several weeks. A pattern recognition technique utilizing singular value decomposition was applied to the sample data to reveal whether or not the varying degradation levels were evident. After showing that SVD revealed the existence of sample clusters, discriminant analysis was applied to determine which bands of the electromagnetic spectrum were the most accurate classifiers of the degradation levels with statistical significance. Tangential questions about the existence of time-dependent behavior in and the uniformity of the degradation across the coating material were investigated using the same approach. Finally, a sample set consisting of two untreated samples and two visibly degraded samples were used to demonstrate the success and difficulties of the approach to accurately classifying new sample data.

The results of this study show that there is strong evidence to support the further investigation of diffuse reflectance infrared Fourier Transform spectroscopy (DRIFTS) for use as a nondestructive inspection tool for aircraft coating characterization. The data analysis and subsequent classification technique showed that several bands of the IR spectrum are capable of clearly revealing the existence of coating degradation and distinguishing between them. Specifically, the fingerprint region of the IR spectrum showed great potential to discern degraded material from non-degraded material as well as distinguish intermediate levels of degradation. The data showed that the samples provided could be correctly classified with 98% accuracy. Unfortunately, this work was conducted on one sample set prepared from the same material batch and prepared in a laboratory environment. While the samples that were provided for study were representative of fielded aircraft coatings, they were not actual samples of fielded coatings. Real aircraft coatings are often four or five layers deep and each layer is made of a different material depending on the function of the layer. Furthermore, when the approach was applied to classify new sample data, the classification rule generated from the fingerprint region was only 28% accurate at classifying the treated sample. The classification rule was adjusted to improve the accuracy to 78%, but still far below the 98% accuracy achieved with a multi-class system. Potential explanations and solutions for the poor performance were discussed. Primarily, the sample set was a two-class system with a limited number of samples. Increasing the number of samples and the levels of degradation in the training set is likely to improve the prediction accuracy of the classification rule. While initially discouraging, there is substantial evidence that

further investigation could lead to a highly accurate tool for detecting coating degradation in the field.

The tangential questions about time-dependent behavior and uniformity of the degradation could not be answered conclusively using this approach. Evidence was presented that suggests that little, if any, of the degradation experienced by the coating material is time-dependent. However, the existence of time-dependent behavior cannot be ruled out conclusively without further testing. It should be noted that the combination of SVD and discriminant analysis was clearly able to discern the different levels of degradation caused by exposure to heat and moisture, but was unable to reveal any time-dependent pattern. Additionally, some evidence of non-uniformity of the degradation of the coating material was detected. In particular, it appeared that the corners of the samples were chemically different from each other and different than the center of the sample, suggesting differing levels of degradation. However, without a known root cause and corresponding characteristic chemical signature of the degradation, it would be difficult to conclusively determine if that was due to differing levels of degradation or some other chemical reaction taking place with the sealant around the edges. Further testing is required to answer these questions conclusively.

When the problem statement and evidence presented here are considered together, it is clear that the Air Force should pursue this effort further. In a relatively short period of time, it was demonstrated that aircraft coating degradation is detectable using FTIR. Handheld FTIR devices are commercially available from several manufacturers and practical for use by maintainers in the field. When the data these

devices collect is combined with pattern recognition algorithms, any subjectivity from a visual inspection is eliminated. The coating can be quantitatively and objectively characterized. The time required to acquire the devices and develop an inspection based on FTIR would be short compared to the time required to research, develop, test, and acquire other nondestructive techniques. Considering aircraft coatings are failing in the field today and are unlikely to be replaced by a more reliable material anytime soon, it is recommended the this research continue.

5.2. Future Work

In order to prove conclusively that the approach laid out in this work is capable of accurately characterizing aircraft coatings, and subsequently predicting remaining service life, more testing is required. The additional testing is primarily an extension of what was already accomplished. It was mentioned repeatedly that the sample set investigated during the course of this work was limited in size and material composition. The next step is to get numerous sets of samples prepared from different batches of coating material and in more intermediate levels of treatment. Ideally, each sample set prepared from the same material batch would contain six to eight samples degraded from untreated to beyond visibly degraded in regular intervals. This would truly test the ability of the proposed approach to detect the degradation before it becomes visible. It would also test the ability of the classification rule to discriminate between very similar levels of degradation.

If the proposed method still proves successful with increased sample variability, the next step is to examine other coating materials. It was shown that the classification

method does not perform the same from one layer configuration to another. Samples should be generated in many, if not all, of the fielded coating configurations so that the validity of the approach can be tested on all of them. The materials sampled during this research were two of the top coat and rain erosion coat materials, but there are other coating materials that need to be investigated. Furthermore, samples removed from fielded aircraft panels should be examined to test the ability to handle variable conditions such as dirty panels and dye in the coatings.

The final step in establishing the validity of the approach would be to correlate the accelerated degradation on the lab samples to real on-aircraft degradation for the purposes of predicting remaining service life. One approach to developing that correlation is to conduct a mass-loss experiment on the coating samples. After collecting the FTIR data on treated samples, small coupons are removed and the masses recorded. Then the coupons are washed in acetone to remove any loose material and massed again. A correlation between the accelerated degradation and on-aircraft degradation can be established in this way.

Eventually, a database of truth data would need to be generated for the purposes of classifying new data. This is the primary limitation of the proposed classification method. Discriminant analysis can only be used to predict new data after the classification rule is generated from known truth data. This introduces what is likely the area of greatest potential for further study. The data analysis methods applied during this work are not the only mathematical techniques that are capable of pattern recognition and data classification. In fact, there are many more techniques that could

potentially produce more accurate and elegant solutions to classification and prediction.

Examples of other classification methods include bootstrapping, principal component analysis, cluster analysis, and regression analysis. This is not an exhaustive list, but are a few of the more common techniques used to classify experimental data.

As shown briefly during the discussion about sample surface uniformity, long wave infrared hyperspectral imaging is also a potential area of future study. The handheld FTIR device and corresponding analysis is an improvement over a visual inspection with respect to quantitative and objective data, but it is still a point by point inspection that would be tedious and time-consuming. Passive imaging of panels, or even the entire aircraft, using a hyperspectral camera would allow large areas to be inspected, thus greatly reducing the time required to inspect an aircraft. Work in this area would include determining the appropriate resolution required in the camera to detect the degradation as well as determining whether or not passive imaging is even a possibility. Active imaging would require heating the panels above room temperature and that could conceivably eliminate hyperspectral imaging as a possibility due to potential damage to the coating materials.

Appendix A. Device Calibration Data

A.1. Repeated Recalibration

Figures A.1-A.3 are plots of the mean, mean subtraction, and standard deviation as a percent of the mean for the reflectance of the gold reference standard used during calibration, respectively.

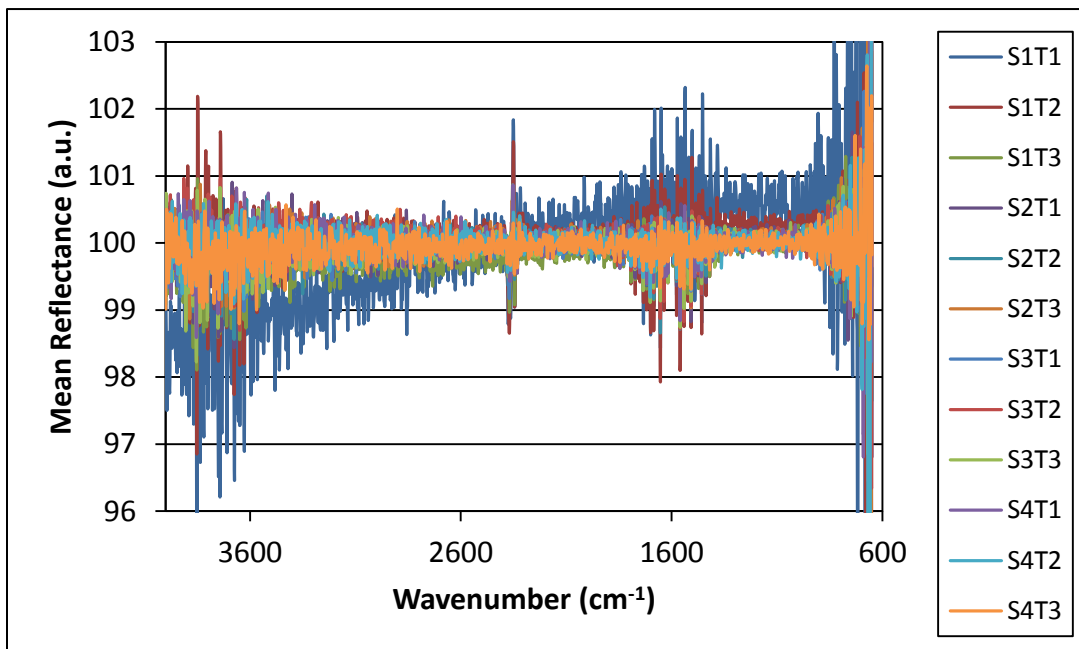


Figure A.1: Mean reflectance of the gold reference standard used for device calibration with recalibration between trials. The expected value of the mean reflectance is 100%. The first trial shows the greatest deviation from the expected value. The naming convention is sample number, trial number (e.g. sample 1, trial 1 is S1T1).

The data was collected just as it was on the samples in set B where five “spots” were sampled per “trial” and three “trials” conducted per “sample”. The device was recalibrated between trials. As discussed in Chapter 3, the detector in the device is a pyroelectric detector that operates by converting a change in temperature to a voltage.

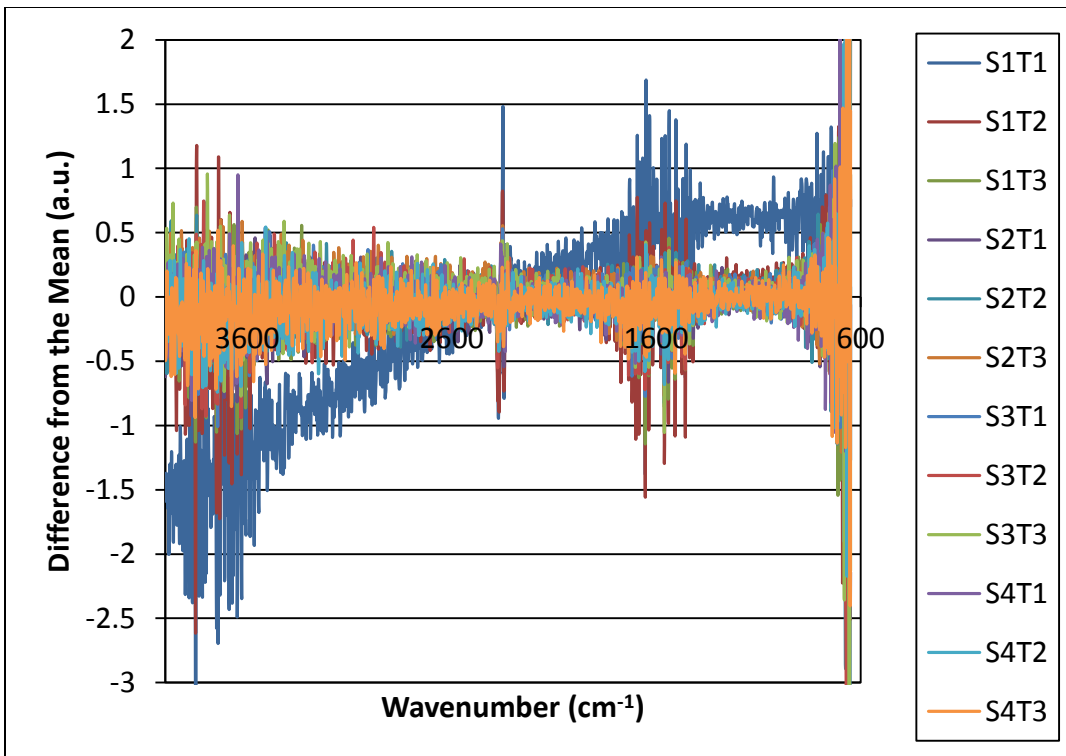


Figure A.2: Mean subtraction of the reflectance collected on the gold reference standard used for device calibration with recalibration between trials. The first trial conducted shows the greatest deviation from the mean. The naming convention is sample number and trial number (e.g. sample 1, trial 1 is S1T1).

The reflectance data collected during the first trial demonstrates this behavior by having the greatest deviation from the mean and highest standard deviation as a percent of the mean reflectance as shown in figures A.2 and A.3. This is due to the fact that the device is still warming up from room temperature while it is collecting data. The increasing temperature of the device is detected as well as the incoming photons being reflected back off the sample surface. As shown in Chapter 3 and again here, repeated recalibration minimizes deviation from the mean and the standard deviation. This maintains a high signal to noise ratio in the data and minimizes device inputs into the sample data.

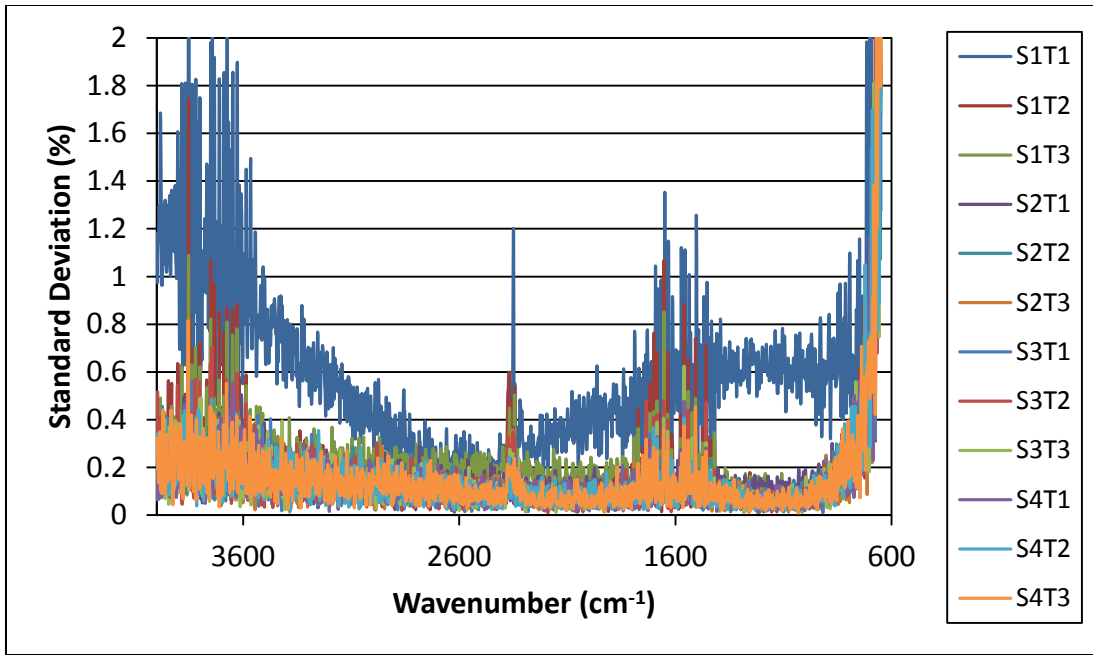


Figure A.3: Standard deviation as a percent of the mean reflectance for data collected on the gold reference standard used for device calibration with recalibration between trials. As already shown, the first trial demonstrates the highest deviation. The naming convention is sample number, trial number (e.g. sample 1, trial 1 is S1T1).

Even though the first trial shows a high deviation from the mean compared to the other trials, the standard deviation remains below 2% of the mean reflectance over the spectral range used for sample analysis. This is a relatively high signal to noise ratio and shows that the device is capable of collecting accurate and reliable data.

A.2. Initial Calibration Only

Figures A.4-A.6 are the mean, mean subtraction, and standard deviation as a percent of the mean for reflectance data collected on the gold reference standard used for device calibration, respectively. Section A.1 shows how the device performs with repeated recalibration during the course of data collection. For comparison, this section

shows how the device performs when it is only calibrated once at the start of the data collection and then not recalibrated again.

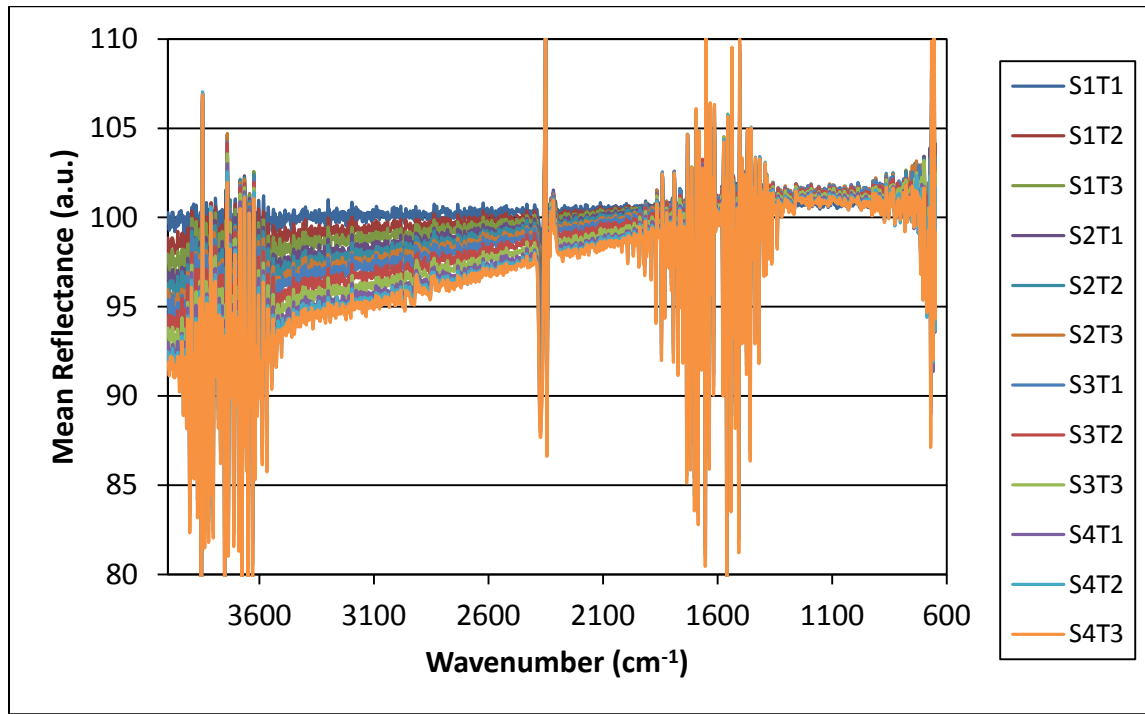


Figure A.4: Mean reflectance of the gold reference standard used for device calibration without recalibration between trials. When not recalibrated regularly, the device drifts to lower reflectance values. Naming convention is sample number, trial number (e.g. sample 1, trial 1 is S1T1).

Even though the device was not recalibrated between “trials”, the data was categorized the same way as in section A.1 in order to draw a comparison between regular calibration intervals and no recalibration. It is obvious in figure A.4 that the device drifts to lower reflectance values over the course of data collection. A comparison between figures A.1 and A.4 shows that regular recalibration during the course of data collection eliminates the device drift and prevents device inputs into the sample data.

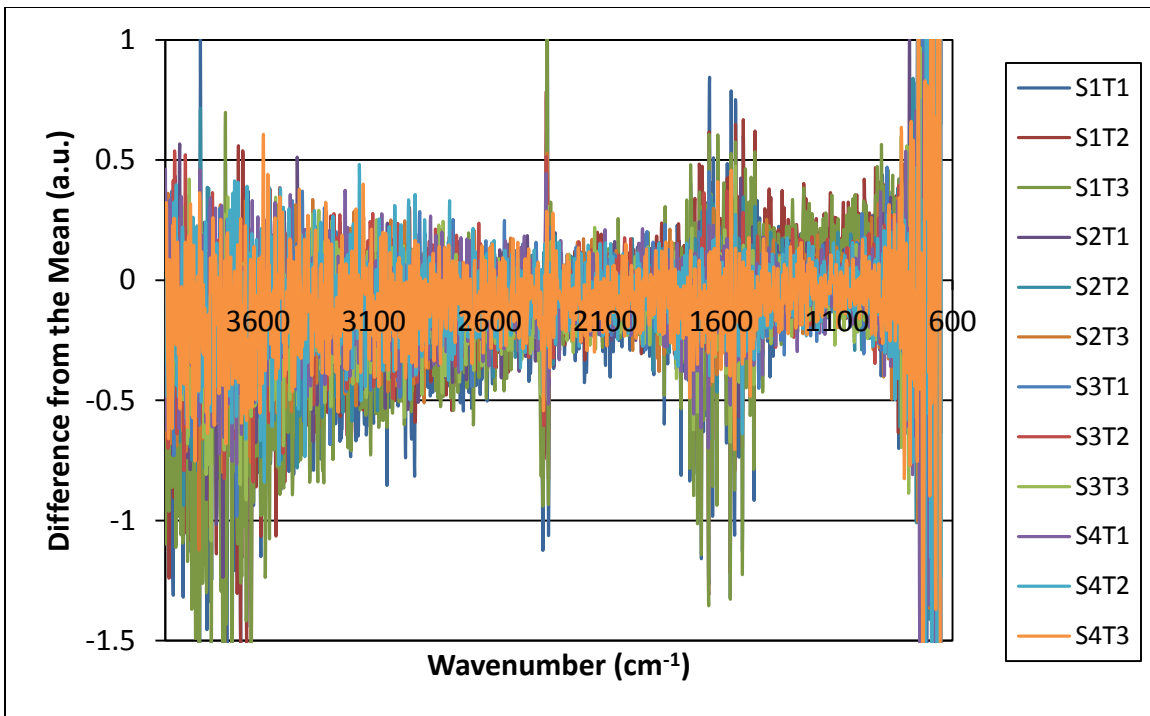


Figure A.5: Mean subtraction of the reflectance collected on the gold reference standard used for device calibration without recalibration between trials. The difference from the mean should be centered at zero, but is slightly negative. The naming convention is sample number, trial number (e.g. sample 1, trial 1 is S1T1).

The mean subtraction should be centered at zero, but figure A.5 shows that the zero mean is actually slightly negative without regular recalibration. When compared to figure A.2, this is further evidence that regular recalibration during data collection was able to minimize device inputs to the sample data.

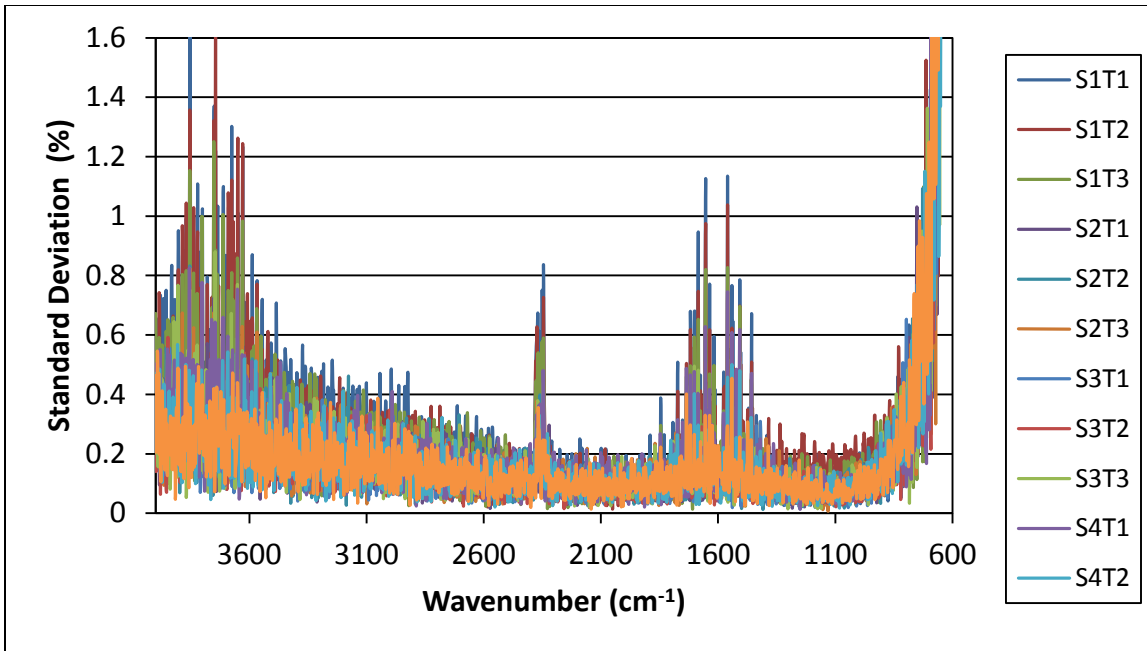


Figure A.6: Standard deviation as a percent of the mean reflectance for the gold reference standard used for device calibration without regular recalibration. Overall, the signal to noise ratio remains high without regular recalibration, but the standard deviation is still higher without it. The naming convention is sample number, trial number (e.g. sample 1, trial 1 is S1T1).

Even without regular recalibration intervals, the standard deviation as a percent of the mean still remains largely below 2%, as shown in figure A.6. However, the noise in the signal remains higher during the course of the data collection period than when the device is recalibrated regularly. The discussion in Chapter 3 illustrates this point better than what can be discerned from figures A.3 and A.6, but it is still evident when comparing the two.

Appendix B. Paint Sample Orientation Diagram

B.1. Paint Sample Orientation Diagram: Sample set A

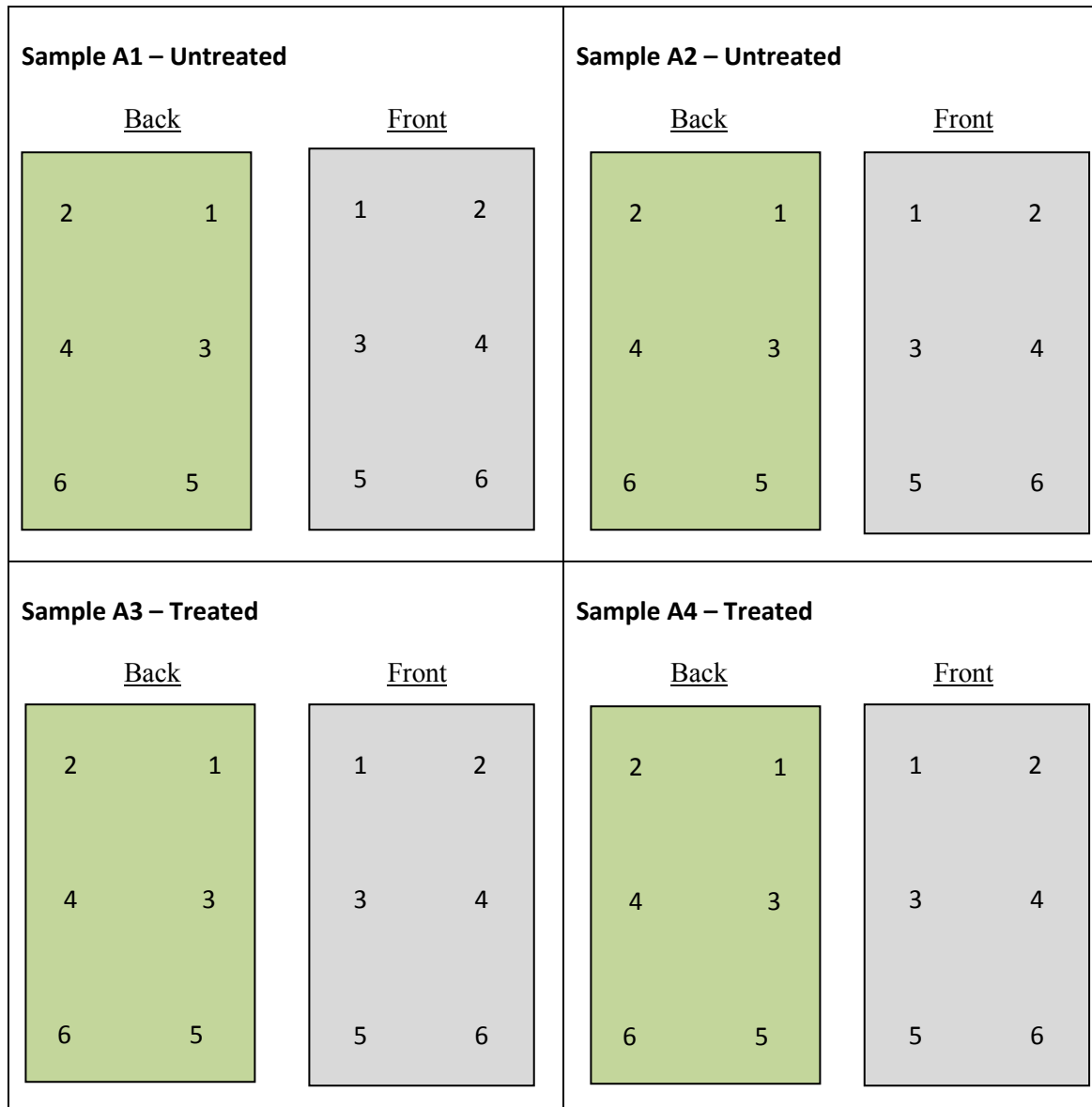


Figure B.1: Sample diagram for sample set A.

B.2. Paint Sample Orientation Diagram: Sample set B

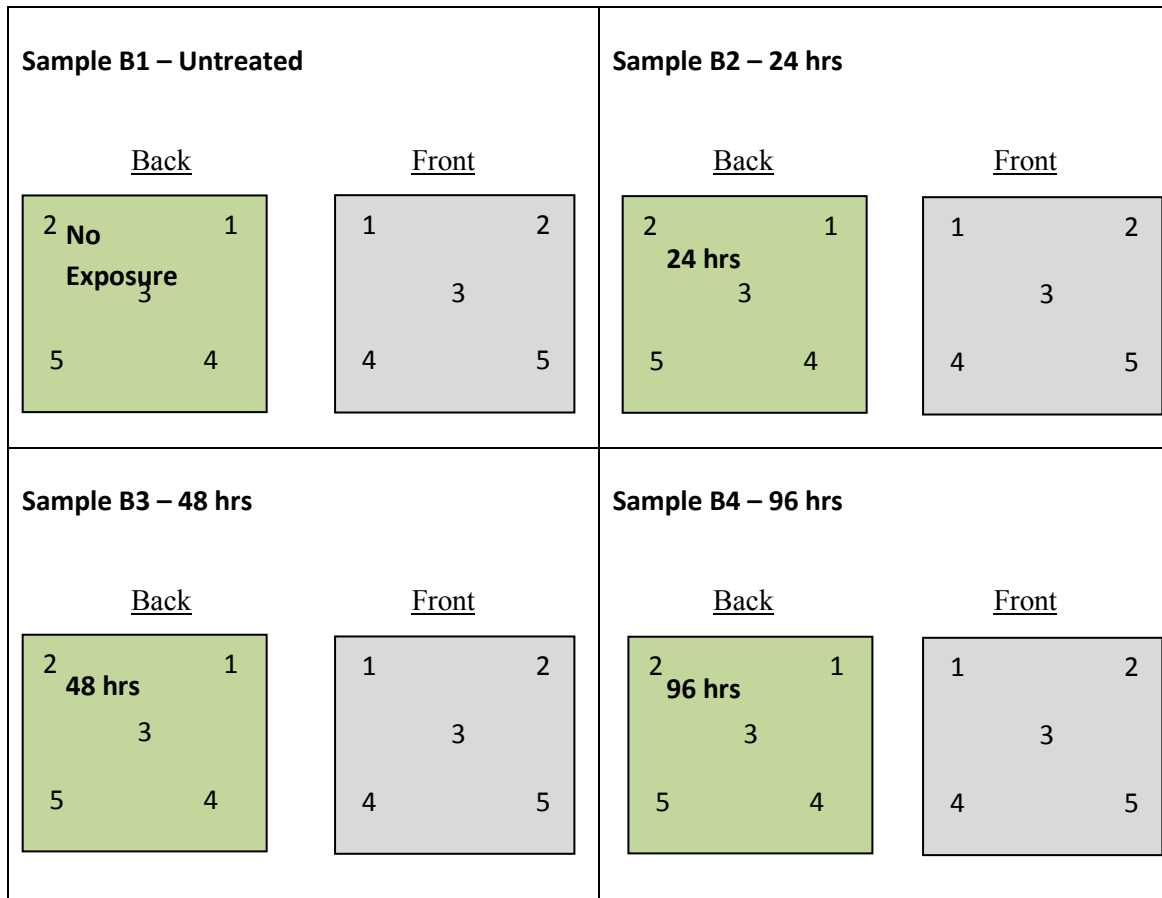


Figure B.2: Sample diagram for sample set B.

Appendix C. MATLAB Code

C.1. Discriminant Analysis by Band for Sample Set B

```
clear all; clc;
%Define the sample categories for the classifier
Y=xlsread('Coefficients for LDA.xlsx','Coefficients','A:A');

%Analyze the 975-875 cm-1 band
%Define the range in the Excel spreadsheet containing the 3 SVD
coefficients %as the measurement criteria for the 975-875 cm-1 band
A=xlsread('Coefficients for LDA.xlsx','Coefficients','B:D');
%Generate the classifier
clsA=ClassificationDiscriminant.fit(A,Y);
%Calculate the resubstitution error of the classifier
resuberrorA=resubLoss(clsA)
%Generate the confusion matrix
RA=confusionmat(clsA.Y,resubPredict(clsA))
%Create a cross-validation model using k-fold analysis with 10 folds
cvmodelA=crossval(clsA,'kfold',10);
%Calculate the k-fold error of the classifier
cverrorA=kfoldLoss(cvmodelA)

%Classify 1150-850 cm-1 band%
%Define the range in the Excel spreadsheet containing the 3 SVD
coefficients %as the measurement criteria for the 1150-850 cm-1 band
B=xlsread('Coefficients for LDA.xlsx','Coefficients','E:G');
%Generate the classifier
clsB=ClassificationDiscriminant.fit(B,Y);
%Calculate the resubstitution error of the classifier
resuberrorB=resubLoss(clsB)
%Generate the confusion matrix
RB=confusionmat(clsB.Y,resubPredict(clsB))
%Create a cross-validation model using k-fold analysis with 10 folds
cvmodelB=crossval(clsB,'kfold',10);
%Calculate the k-fold error of the classifier
cverrorB=kfoldLoss(cvmodelB)

%Classify 1150-1050 cm-1 band%
%Define the range in the Excel spreadsheet containing the 3 SVD
coefficients %as the measurement criteria for the 1150-1050 cm-1 band
C=xlsread('Coefficients for LDA.xlsx','Coefficients','H:J');
%Generate the classifier
clsC=ClassificationDiscriminant.fit(C,Y);
%Calculate the resubstitution error of the classifier
resuberrorC=resubLoss(clsC)
%Generate the confusion matrix
RC=confusionmat(clsC.Y,resubPredict(clsC))
%Create a cross-validation model using k-fold analysis with 10 folds
cvmodelC=crossval(clsC,'kfold',10);
```

```

%Calculate the k-fold error of the classifier
cverrorC=kfoldLoss(cvmodelC)

%Classify 1200-800 cm-1 band%
%Define the range in the Excel spreadsheet containing the 3 SVD
coefficients %as the measurement criteria for the 1200-800 cm-1 band
D=xlsread('Coefficients for LDA.xlsx','Coefficients','K:M');
%Generate the classifier
clsD=ClassificationDiscriminant.fit(D,Y);
%Calculate the resubstitution error of the classifier
resuberrorD=resubLoss(clsD)
%Generate the confusion matrix
RD=confusionmat(clsD.Y,resubPredict(clsD))
%Create a cross-validation model using k-fold analysis with 10 folds
cvmodelD=crossval(clsD,'kfold',10);
%Calculate the k-fold error of the classifier
cverrorD=kfoldLoss(cvmodelD)

%Classify 1220-850 cm-1 band%
%Define the range in the Excel spreadsheet containing the 3 SVD
coefficients %as the measurement criteria for the 1220-850 cm-1 band
E=xlsread('Coefficients for LDA.xlsx','Coefficients','N:P');
%Generate the classifier
clsE=ClassificationDiscriminant.fit(E,Y);
%Calculate the resubstitution error of the classifier
resuberrorE=resubLoss(clsE)
%Generate the confusion matrix
RE=confusionmat(clsE.Y,resubPredict(clsE))
%Create a cross-validation model using k-fold analysis with 10 folds
cvmodelE=crossval(clsE,'kfold',10);
%Calculate the k-fold error of the classifier
cverrorE=kfoldLoss(cvmodelE)

%Classify 1800-800 cm-1 band%
%Define the range in the Excel spreadsheet containing the 3 SVD
coefficients %as the measurement criteria for the 1800-800 cm-1 band
F=xlsread('Coefficients for LDA.xlsx','Coefficients','Q:S');
%Generate the classifier
clsF=ClassificationDiscriminant.fit(F,Y);
%Calculate the resubstitution error of the classifier
resuberrorF=resubLoss(clsF)
%Generate the confusion matrix
RF=confusionmat(clsF.Y,resubPredict(clsF))
%Create a cross-validation model using k-fold analysis with 10 folds
cvmodelF=crossval(clsF,'kfold',10);
%Calculate the k-fold error of the classifier
cverrorF=kfoldLoss(cvmodelF)

%Classify 1800-1200 cm-1 band%
%Define the range in the Excel spreadsheet containing the 3 SVD
coefficients %as the measurement criteria for the 1800-1200 cm-1 band
G=xlsread('Coefficients for LDA.xlsx','Coefficients','T:V');
%Generate the classifier
clsG=ClassificationDiscriminant.fit(G,Y);
%Calculate the resubstitution error of the classifier

```

```

resuberrorG=resubLoss(clsG)
%Generate the confusion matrix
RG=confusionmat(clsG.Y,resubPredict(clsG))
%Create a cross-validation model using k-fold analysis with 10 folds
cvmodelG=crossval(clsG,'kfold',10);
%Calculate the k-fold error of the classifier
cverrorG=kfoldLoss(cvmodelG)

%Classify 1800-1450 cm-1 band%
%Define the range in the Excel spreadsheet containing the 3 SVD
coefficients %as the measurement criteria for the 1800-1450 cm-1 band
H=xlsread('Coefficients for LDA.xlsx','Coefficients','W:Y');
%Generate the classifier
clsH=ClassificationDiscriminant.fit(H,Y);
%Calculate the resubstitution error of the classifier
resuberrorH=resubLoss(clsH)
RH=confusionmat(clsH.Y,resubPredict(clsH))
%Create a cross-validation model using k-fold analysis with 10 folds
cvmodelH=crossval(clsH,'kfold',10);
%Calculate the k-fold error of the classifier
cverrorH=kfoldLoss(cvmodelH)

%Classify 1800-1650 cm-1 band%
%Define the range in the Excel spreadsheet containing the 3 SVD
coefficients %as the measurement criteria for the 1800-1650 cm-1 band
I=xlsread('Coefficients for LDA.xlsx','Coefficients','Z:AB');
%Generate the classifier
clsI=ClassificationDiscriminant.fit(I,Y);
%Calculate the resubstitution error of the classifier
resuberrorI=resubLoss(clsI)
%Generate the confusion matrix
RI=confusionmat(clsI.Y,resubPredict(clsI))
%Create a cross-validation model using k-fold analysis with 10 folds
cvmodelI=crossval(clsI,'kfold',10);
%Calculate the k-fold error of the classifier
cverrorI=kfoldLoss(cvmodelI)

%Classify 1800-800 minus 1500-1200 cm-1 band%
%Define the range in the Excel spreadsheet containing the 3 SVD
coefficients %as the measurement criteria for the 1800-800 minus 1500-
1200 cm-1 band
J=xlsread('Coefficients for LDA.xlsx','Coefficients','AC:AE');
%Generate the classifier
clsJ=ClassificationDiscriminant.fit(J,Y);
%Calculate the resubstitution error of the classifier
resuberrorJ=resubLoss(clsJ)
%Generate the confusion matrix
RJ=confusionmat(clsJ.Y,resubPredict(clsJ))
%Create a cross-validation model using k-fold analysis with 10 folds
cvmodelJ=crossval(clsJ,'kfold',10);
%Calculate the k-fold error of the classifier
cverrorJ=kfoldLoss(cvmodelJ)

```

C.2. SVD Analysis and LDA Sample Set A (Entire Spectrum)

```
clear all; clc;
%After conducting the mean subtraction of the training set in Excel,
%define the mean subtracted data matrix to execute the SVD on
D=xlsread('Sample Set A.xlsx','Mean Sub Training Set','B1:BU1797');
%Transpose the mean subtracted matrix for the matrix operations
d=D.';
%Define the output matrices from the SVD
[U,S,V]=svd(d);
%Calculate the coefficient matrix using one of the Eigenfunction
%matrices, U or V. U and V are the new bases of the data set
C=d*V;
%Cutoff the coefficient matrix for the training set to the first two
%coefficients
c2=C(:,1:2);

%Begin LDA Analysis after verifying that SVD worked
%Define the Categorical Variables for LDA
Y=xlsread('SVD_Set_A_Entire_Spectrum.xlsx','Training Set
Coeff','A2:A73');
%Define the classification criteria as the first two coefficients
%Develop the classifier using one untreated and one treated sample
cls2=ClassificationDiscriminant.fit(c2,Y);
%Calculate the resubstitution error to see how the classifier performs
resuberror2=resubLoss(cls2)
%Generate the confusion matrix of the classification rule to see where
the
%misclassifications are
R2=confusionmat(cls2.Y,resubPredict(cls2))
%Generate a cross-validation model to further check the accuracy of the
%model
cvmodel2=crossval(cls2,'kfold',10);
%Check the error rates generated from the cross-validation model
cverror2=kfoldLoss(cvmodel2)
%Plot the coefficients and classification boundaries to see how the
model will work
a1=C(:,1);
a2=C(:,2);
h1=gscatter(a1,a2,Y,'kr','ov',[],'off');
set(h1,'LineWidth',2)
legend('Untreated','Treated')
hold on
K=cls2.Coeffs(1,2).Const;
L=cls2.Coeffs(1,2).Linear;
% Plot the curve K + [x1,x2]*L = 0:
f=@(x1,x2) K + L(1)*x1 + L(2)*x2;
h2=ezplot(f,[-100 200 -20 60]);
set(h2,'Color','k','LineWidth',2)
xlabel('a_1')
ylabel('a_2')
hold off

%After subtracting the training set mean from the new data set,
```

```

%define the mean subtracted data matrix for classification
P=xlsread('Sample Set A.xlsx','Mean Sub New Set','B1:BU1797');
%Transpose the mean subtracted matrix for the matrix operations
p=P.';
%Calculate the coefficient matrix using one of the Eigenfunction
%matrices, U or V. U and V are the new bases of the data set
K=p*V;
%Cutoff the new coefficient matrix to the first two coefficients
k2=K(:,1:2);
%Predict the classification of the new sample data
Sample2=predict(cls2,k2);
%Output the predicted classification into the excel file containing the
SVD
%coefficients for the new samples
xlswrite('SVD_Set_A_Entire_Spectrum.xlsx',Sample2,'New Set
Coeff','E3');

%Cutoff the coefficient matrix for the training set to the first three
%coefficients
c3=C(:,1:3);
%Export the coefficients to Excel for examination and plotting
xlswrite('SVD_Set_A_Entire_Spectrum.xlsx',c3,'Training Set
Coeff','B2');

%Develop a new classifier the first 3 coefficients using the same pair
%of
%treated and untreated samples as above
cls3=ClassificationDiscriminant.fit(c3,Y);
%Calculate the resubstitution error to see how the classifier performs
resuberror3=resubLoss(cls3)
%Generate the confusion matrix of the classification rule to see where
%the
%misclassifications are
R3=confusionmat(cls3.Y,resubPredict(cls3))
%Generate a cross-validation model to further check the accuracy of the
%model
cvmodel3=crossval(cls3,'kfold',10);
%Check the error rates generated from the cross-validation model
cverror3=kfoldLoss(cvmodel3)

%Cutoff the coefficient matrix to the first three coefficients
k3=K(:,1:3);
%Export the coefficients to Excel for examination and plotting
xlswrite('SVD_Set_A_Entire_Spectrum.xlsx',k3,'New Set Coeff','B3');
%Predict the classification of the new sample data
Sample3=predict(cls3,k3);
%Output the predicted classification into the excel file containing the
SVD
%coefficients for the new samples for comparison to the two coefficient
%prediction
xlswrite('SVD_Set_A_Entire_Spectrum.xlsx',Sample3,'New Set
Coeff','F3');

```

C.3. SVD Analysis and LDA Sample Set A (Fingerprint Region)

```
clear all; clc;
%After conducting the mean subtraction of the training set in Excel,
%define the mean subtracted data matrix to execute the SVD on
D=xlsread('Sample Set A.xlsx','Mean Sub Training Set','B1491:BU1689');
%Transpose the mean subtracted matrix for the matrix operations
d=D.';
%Define the output matrices from the SVD
[U,S,V]=svd(d);
%Calculate the coefficient matrix using one of the Eigenfunction
%matrices, U or V. U and V are the new bases of the data set
C=d*V;
%Cutoff the coefficient matrix for the training set to the first two
%coefficients
c2=C(:,1:2);

%Begin LDA Analysis after verifying that SVD worked
%Define the Categorical Variables for LDA
Y=xlsread('SVD_Set_A_Fingerprint.xlsx','Training Set Coeff','A2:A73');
%Define the classification criteria as the first two coefficients
%Develop the classifier using one untreated and one treated sample
cls2=ClassificationDiscriminant.fit(c2,Y);
%Calculate the resubstitution error to see how the classifier performs
resuberror2=resubLoss(cls2)
%Generate the confusion matrix of the classification rule to see where
%the
%misclassifications are
R2=confusionmat(cls2.Y,resubPredict(cls2))
%Generate a cross-validation model to further check the accuracy of the
%model
cvmodel2=crossval(cls2,'kfold',10);
%Check the error rates generated from the cross-validation model
cverror2=kfoldLoss(cvmodel2)
%Plot the coefficients and classification boundaries to see how the
model will work
a1=C(:,1);
a2=C(:,2);
h1=gscatter(a1,a2,Y,'kr','ov',[],'off');
set(h1,'LineWidth',2)
legend('Untreated','Treated')
hold on
K=cls2.Coeffs(1,2).Const;
L=cls2.Coeffs(1,2).Linear;
% Plot the curve K + [x1,x2]*L = 0:
f=@(x1,x2) K + L(1)*x1 + L(2)*x2;
h2=ezplot(f,[-30 60 -20 10]);
set(h2,'Color','k','LineWidth',2)
xlabel('a_1')
ylabel('a_2')
hold off

%After subtracting the training set mean from the new data set,
%define the mean subtracted data matrix for classification
```

```

P=xlsread('Sample Set A.xlsx','Mean Sub New Set','B1491:BU1689');
%Transpose the mean subtracted matrix for the matrix operations
p=P.';
%Calculate the coefficient matrix using one of the Eigenfunction
%matrices, U or V. U and V are the new bases of the data set
K=p*V;
%Cutoff the new coefficient matrix to the first two coefficients
k2=K(:,1:2);
%Predict the classification of the new sample data
Sample2a=predict(cls2,k2);
%Output the predicted classification into the excel file containing the
SVD
%coefficients for the new samples
xlswrite('SVD_Set_A_Fingerprint.xlsx',Sample2a,'New Set Coeff','E3');
%Change the cost of misclassification of treated as untreated to
improve
%the prediction rate
cls2.Cost(2,1)=100;
%Re-predict the classification of the new sample data
Sample2b=predict(cls2,k2);
%Output the new predicted classification into the excel file containing
the
%SVD coefficients for the new samples
xlswrite('SVD_Set_A_Fingerprint.xlsx',Sample2b,'New Set Coeff','G3');
%Plot the new classification rule with the adjusted cost
figure
h3=gscatter(a1,a2,Y,'kr','ov',[],'off');
set(h3,'LineWidth',2)
legend('Untreated','Treated')
hold on
K1=cls2.Coeffs(1,2).Const;
L1=cls2.Coeffs(1,2).Linear;
% Plot the curve K + [x1,x2]*L = 0:
f2=@(x1,x2) K1 + L1(1)*x1 + L1(2)*x2;
h4=ezplot(f2,[-30 60 -20 10]);
set(h4,'Color','k','LineWidth',2)
xlabel('a_1')
ylabel('a_2')
hold off

%Cutoff the coefficient matrix for the training set to the first three
%coefficients
c3=C(:,1:3);
%Export the coefficients to Excel for examination and plotting
xlswrite('SVD_Set_A_Fingerprint.xlsx',c3,'Training Set Coeff','B2');

%Develop a new classifier the first 3 coefficients using the same pair
%of
%treated and untreated samples as above
cls3=ClassificationDiscriminant.fit(c3,Y);
%Calculate the resubstitution error to see how the classifier performs
resuberror3=resubLoss(cls3)
%Generate the confusion matrix of the classification rule to see where
the
%misclassifications are

```

```

R3=confusionmat(cls3.Y,resubPredict(cls3))
%Generate a cross-validation model to further check the accuracy of the
%model
cvmodel3=crossval(cls3,'kfold',10);
%Check the error rates generated from the cross-validation model
cverror3=kfoldLoss(cvmodel3)

%Cutoff the coefficient matrix to the first three coefficients
k3=K(:,1:3);
%Export the coefficients to Excel for examination and plotting
xlswrite('SVD_Set_A_Fingerprint.xlsx',k3,'New Set Coeff','B3');
%Predict the classification of the new sample data
Sample3=predict(cls3,k3);
%Output the predicted classification into the excel file containing the
SVD
%coefficients for the new samples for comparison to the two coefficient
%prediction
xlswrite('SVD_Set_A_Fingerprint.xlsx',Sample3,'New Set Coeff','F3');

```

Appendix D. SVD Coefficient Plots

D.1. SVD Coefficient Plots by Band for Sample Set B

Figures D.1-D.24 are the SVD coefficient plots by band for the bands that were not discussed in detail in Chapter 4. All the bands show some clustering and separation between the samples, but the inclusion of the plots in the discussion would have been redundant. They are included here for completeness.

D.1.1. $1150-850 \text{ cm}^{-1}$ (8.7-11.8 μm).

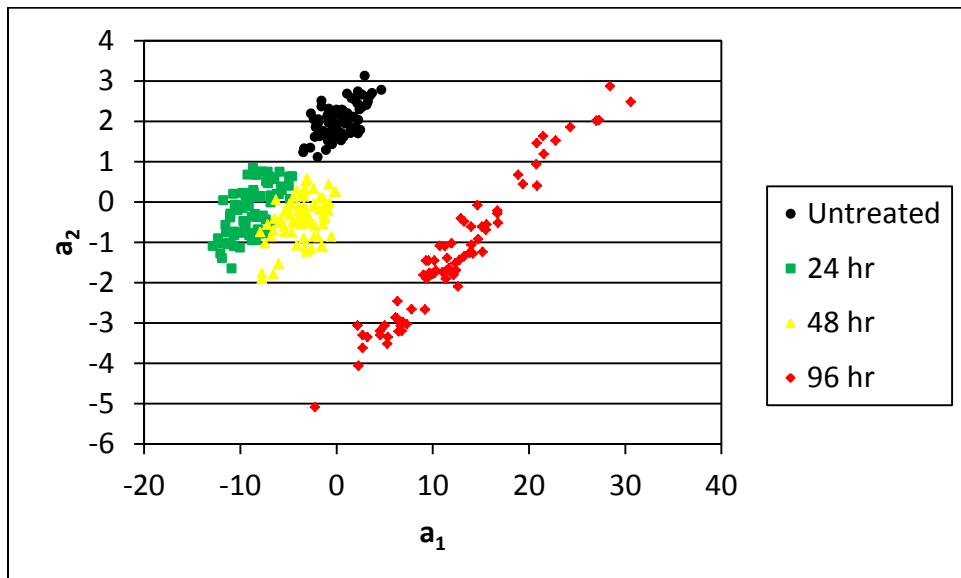


Figure D.1: Plot of the first two coefficients in the $1150-850 \text{ cm}^{-1}$ band for sample set B. There is good sample clustering and separation in this band.

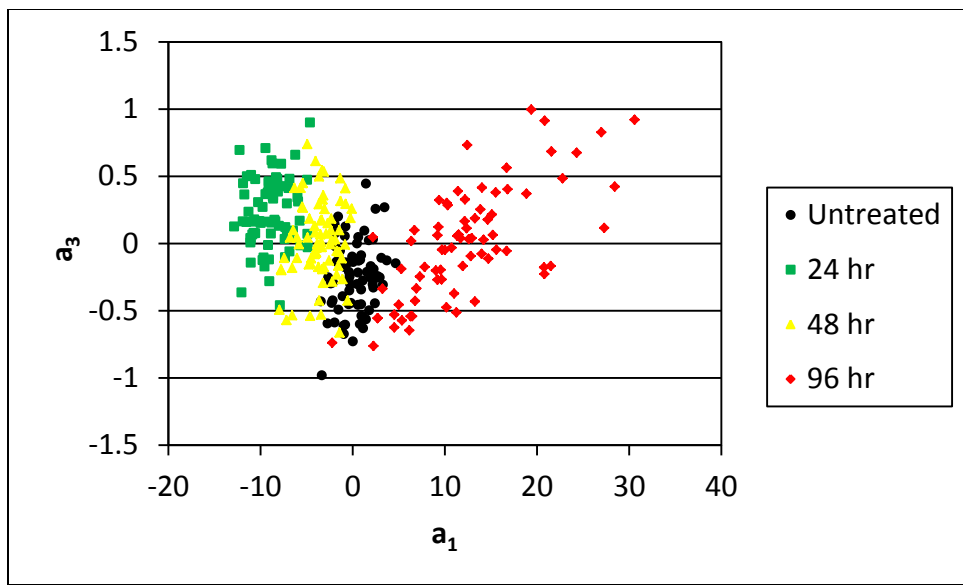


Figure D.2: Plot of the first and third coefficients in the $1150-850 \text{ cm}^{-1}$ band for sample set B. There is some clustering of the samples, but the third coefficient does not contribute much to the ability to classify samples.

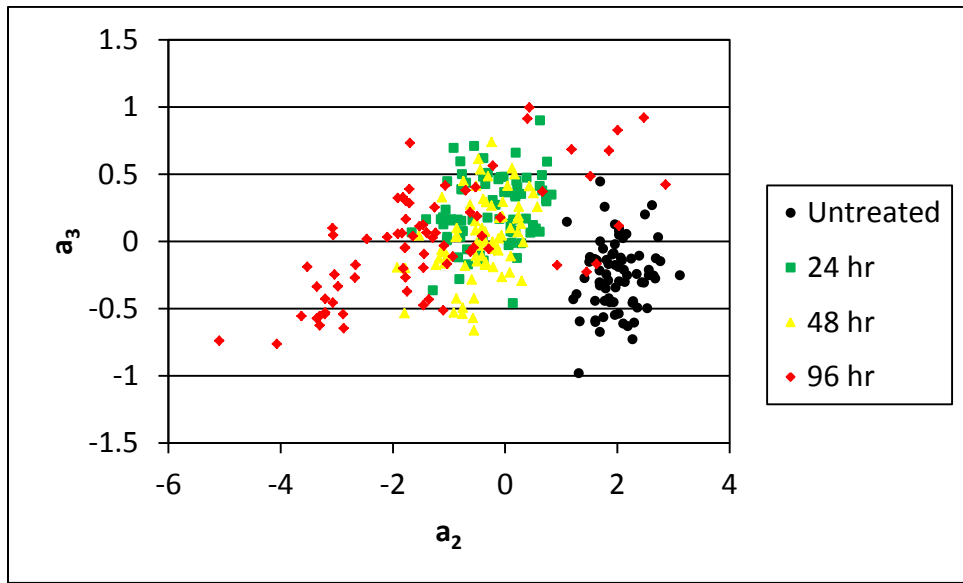


Figure D.3: Plot of the second and third coefficients in the $1150-850 \text{ cm}^{-1}$ band for sample set B. The untreated sample is separated from the other three along the second coefficient, but as shown with the other bands, the second and third coefficients do contribute much to classifying the samples.

D.1.2. 1150-1050 cm^{-1} (8.7-9.5 μm).

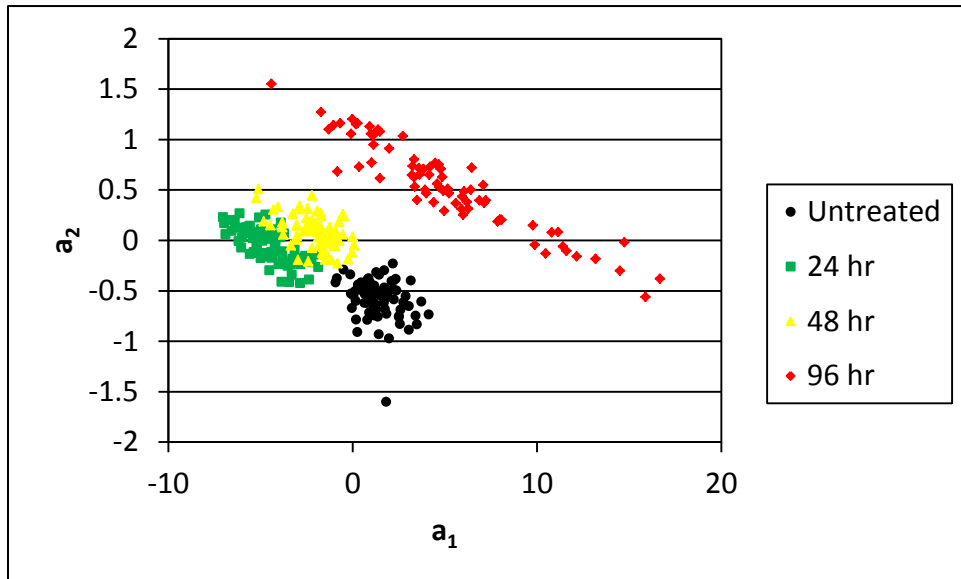


Figure D.4: Plot of the first two coefficients in the 1150-1050 cm^{-1} band for sample set B. Like most of the bands, there is good sample clustering and separation in this band.

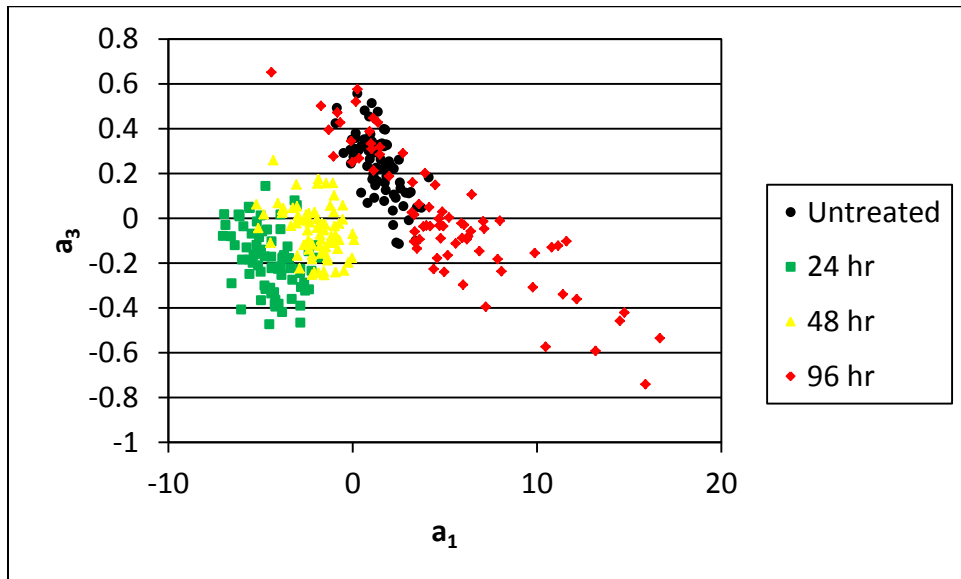


Figure D.5: Plot of the first and third coefficients in the 1150-1050 cm^{-1} band for sample set B. There is some clustering of the samples, but the third coefficient does not contribute much.

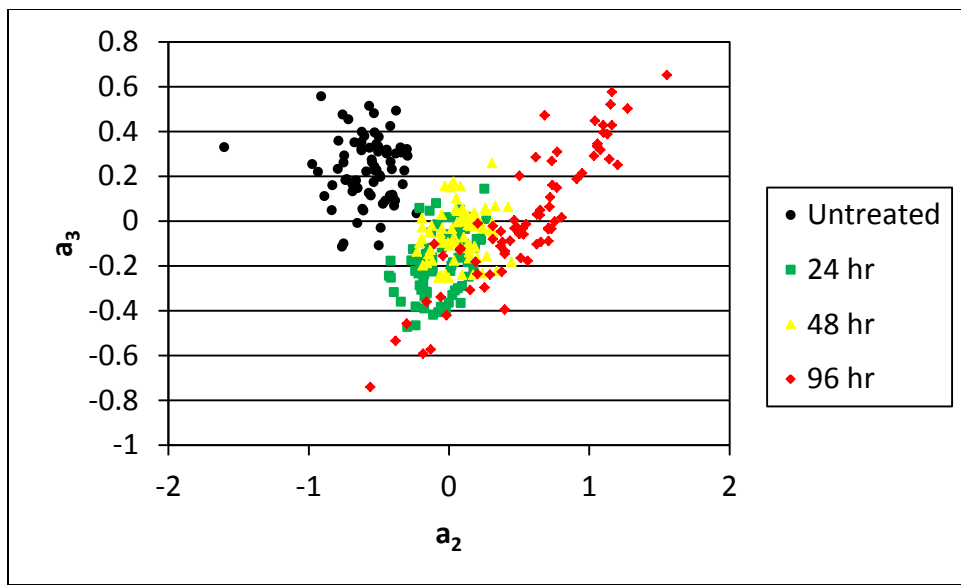


Figure D.6: Plot of the second and third coefficients in the $1150\text{-}1050\text{ cm}^{-1}$ band for sample set B. The untreated sample is separated from the other three along the second coefficient, but as shown with the other bands, the second and third coefficients do contribute much to classifying the samples.

D.1.3. $1200\text{-}800\text{ cm}^{-1}$ (8.3-12.5 μm).

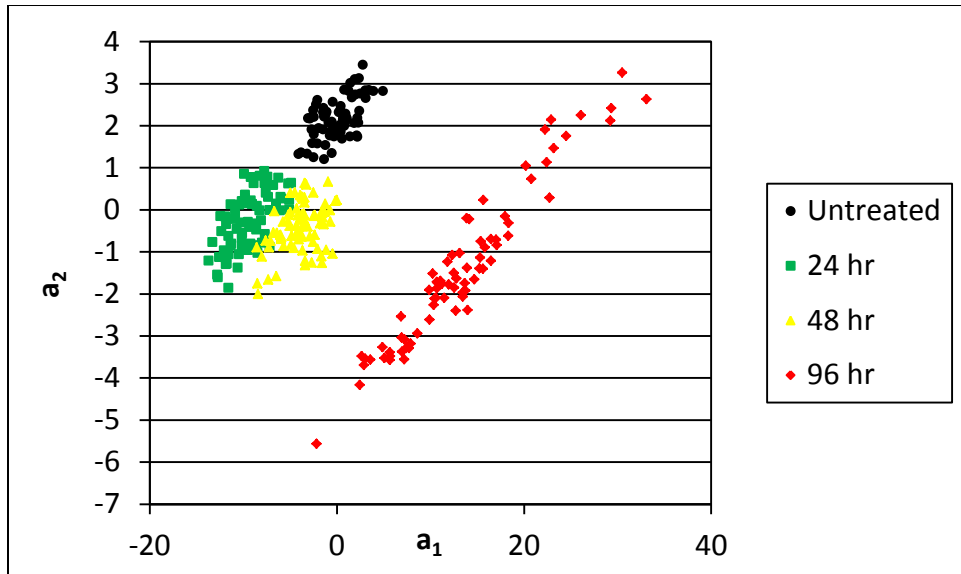


Figure D.7: Plot of the first two coefficients in the $1200\text{-}800\text{ cm}^{-1}$ band for sample set B. Like most of the bands, there is good sample clustering and separation in this band.

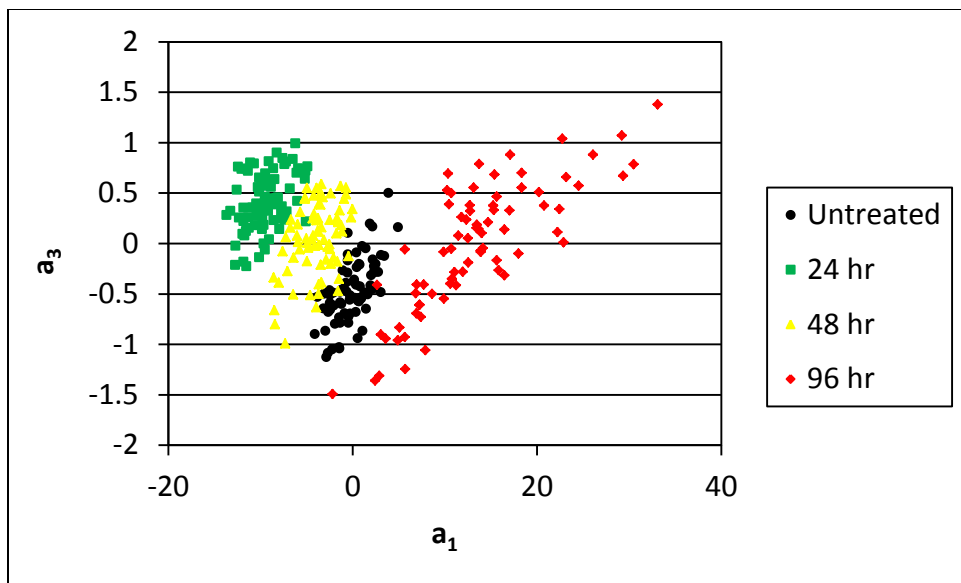


Figure D.8: Plot of the first and third coefficients in the $1200-800\text{ cm}^{-1}$ band for sample set B. There is some clustering of the samples, but the third coefficient does not contribute much like most of the bands.

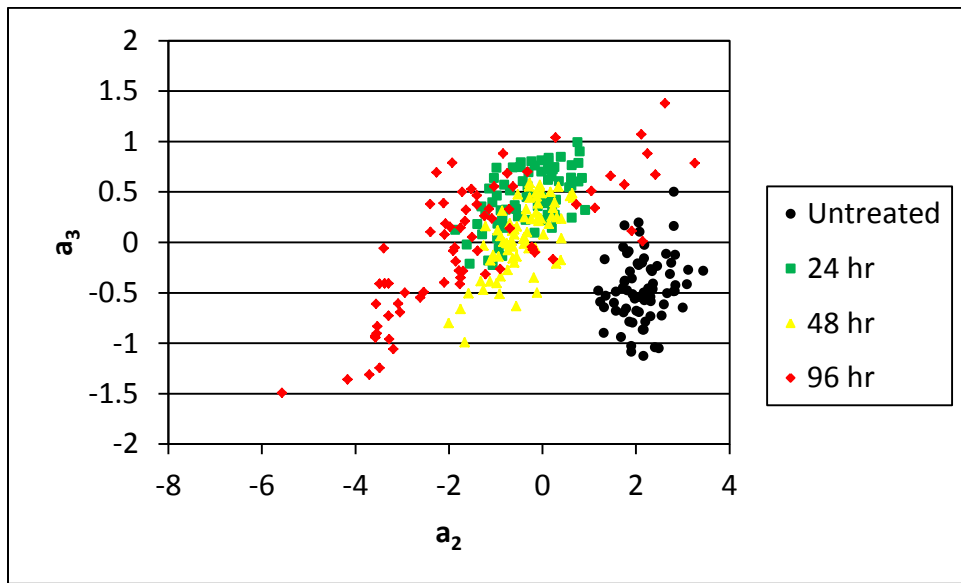


Figure D.9: Plot of the second and third coefficients in the $1200-800\text{ cm}^{-1}$ band for sample set B. The untreated sample is separated from the other three along the second coefficient, but as shown with the other bands, the second and third coefficients do contribute much to classifying the samples.

D.1.4. $1800-800 \text{ cm}^{-1}$ (5.6-12.5 μm).

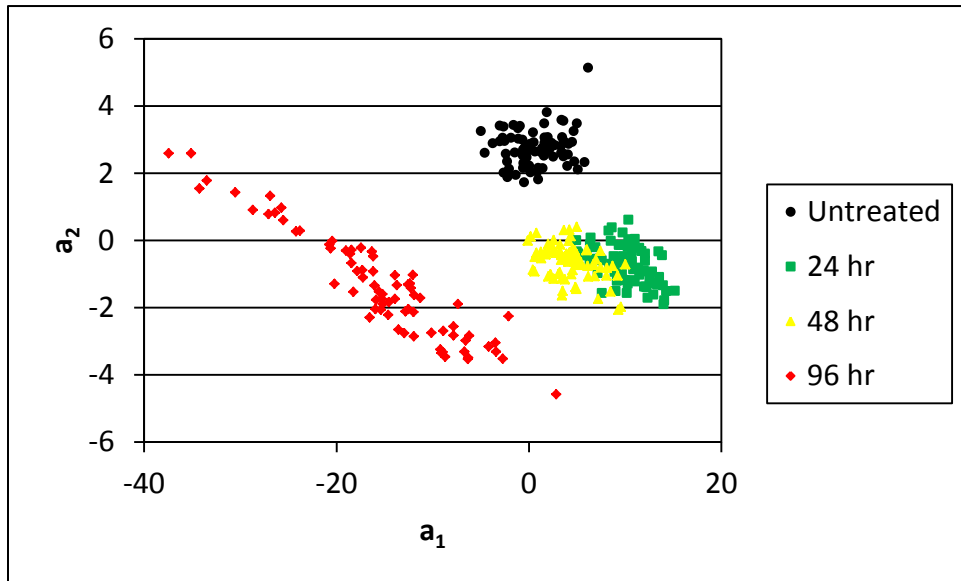


Figure D.10: Plot of the first two coefficients in the $1800-800 \text{ cm}^{-1}$ band for sample set B. Like most of the bands, there is good sample clustering and separation in this band.

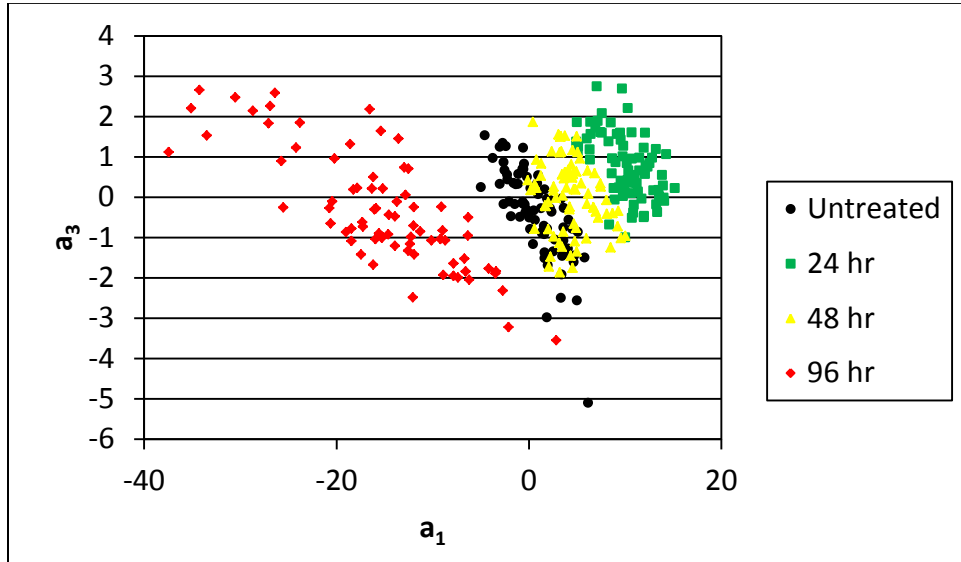


Figure D.11: Plot of the first and third coefficients in the $1800-800 \text{ cm}^{-1}$ band for sample set B. There is some clustering of the samples, but the third coefficient does not contribute much like most of the bands.

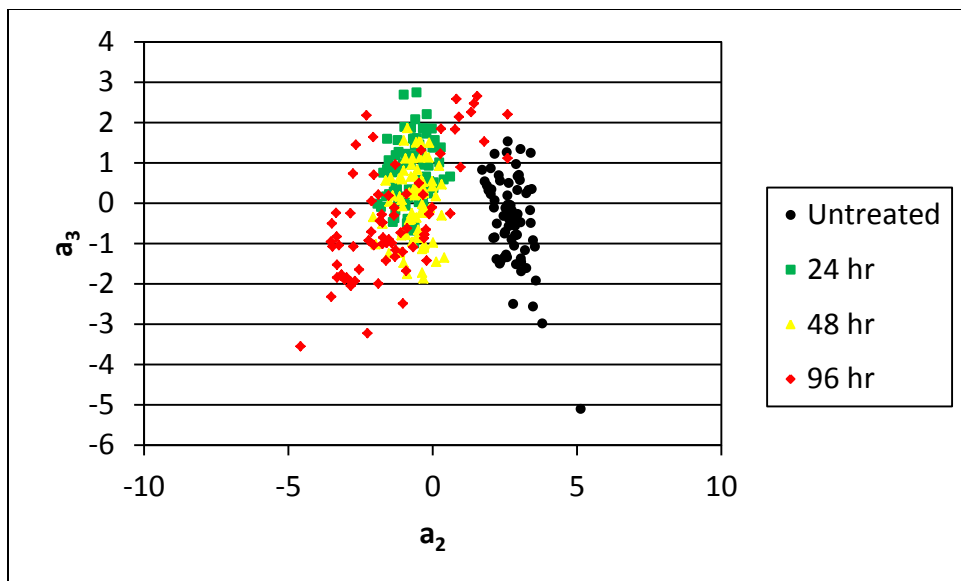


Figure D.12: Plot of the second and third coefficients in the $1800-800\text{ cm}^{-1}$ band for sample set B. The untreated sample is separated from the other three along the second coefficient, but as shown with the other bands, the second and third coefficients do contribute much to classifying the samples.

D.1.5. $1800-1200\text{ cm}^{-1}$ (5.6-8.3 μm).

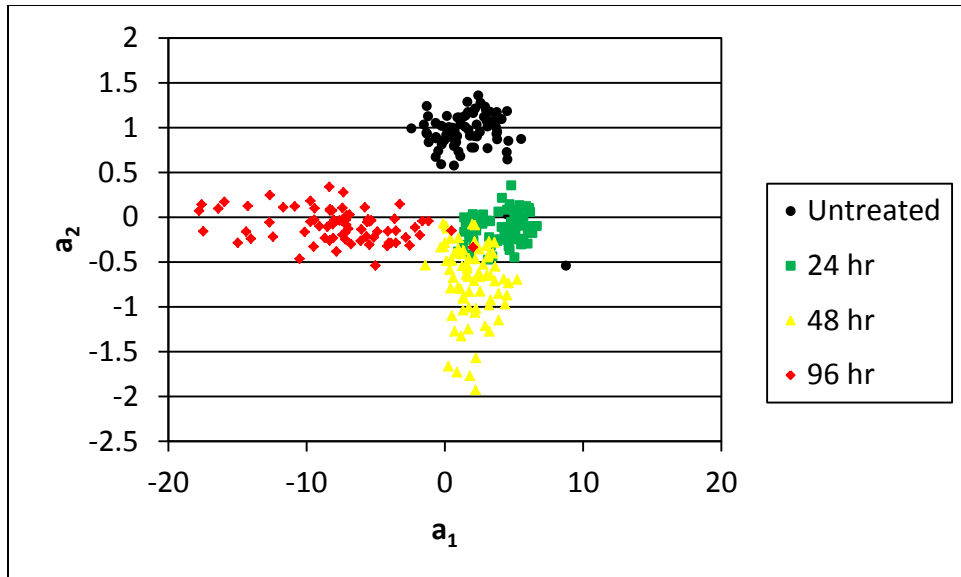


Figure D.13: Plot of the first two coefficients in the $1800-1200\text{ cm}^{-1}$ band for sample set B. Like most of the bands, there is good sample clustering and separation in this band. However, the general relationship between the samples is drastically different than the other bands. The clusters fall almost entirely along either the first or second coefficient axis.

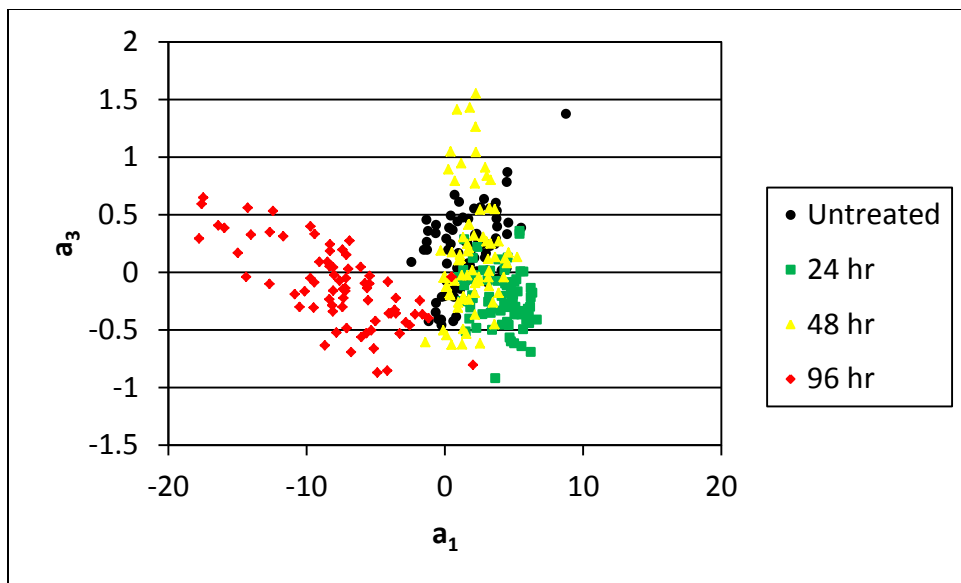


Figure D.14: Plot of the first and third coefficients in the $1800-1200\text{ cm}^{-1}$ band for sample set B. The 96 hour sample is separated from the others while the untreated, 24 hour, and 48 hour samples are on top of each other.

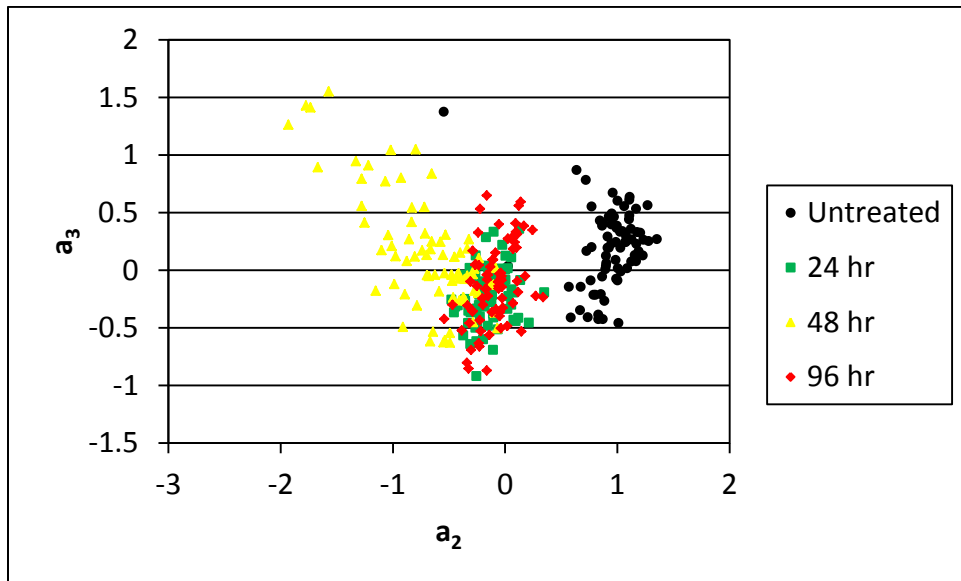


Figure D.15: Plot of the second and third coefficients in the $1800-1200\text{ cm}^{-1}$ band for sample set B. Unlike previous bands, the untreated and 48 hour samples are separated from the other two along the second coefficient. However, the second and third coefficients still do not contribute much to ability to classify the samples.

D.1.6. $1800-1450 \text{ cm}^{-1}$ (5.6-6.9 μm).

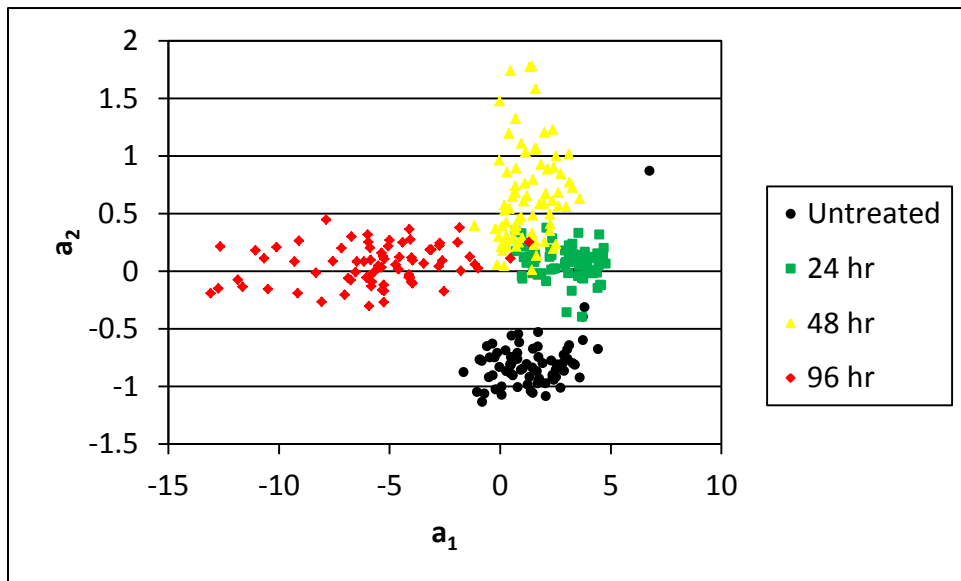


Figure D.16: Plot of the first two coefficients in the $1800-1450 \text{ cm}^{-1}$ band for sample set B. The general relationship between the samples is the same as in the $1800-1200 \text{ cm}^{-1}$ band, with the clusters lying almost entirely along either the first or second coefficient axis.

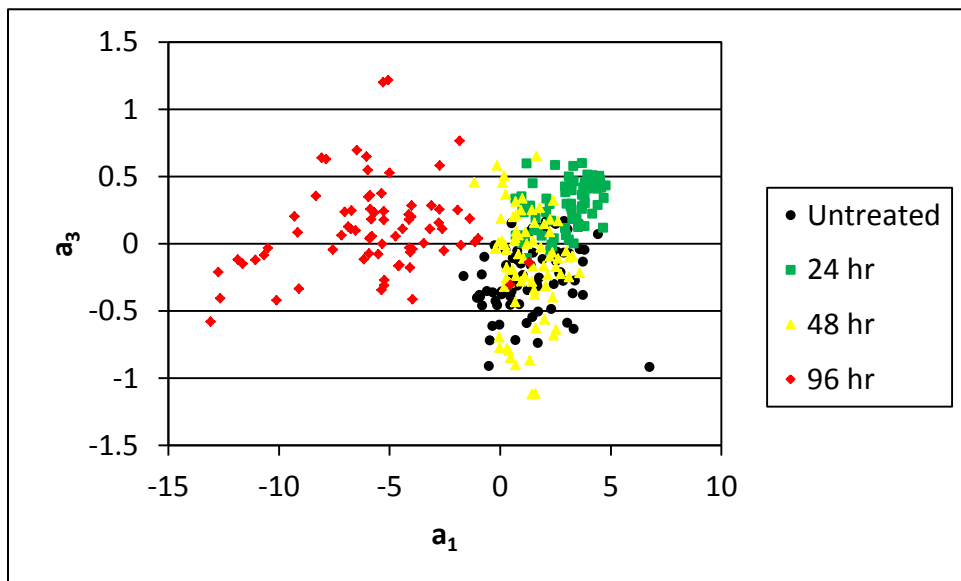


Figure D.17: Plot of the first and third coefficients in the $1800-1450 \text{ cm}^{-1}$ band for sample set B. The 96 hour sample is separated from the others while the untreated, 24 hour, and 48 hour samples are on top of each other.

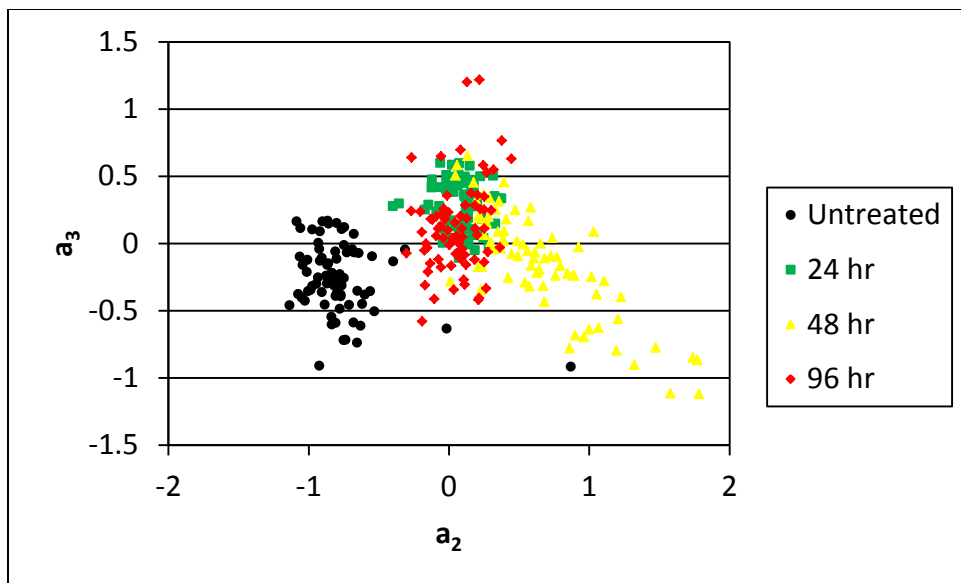


Figure D.18: Plot of the second and third coefficients in the $1800-1450\text{ cm}^{-1}$ band for sample set B. Like the $1800-1200\text{ cm}^{-1}$ band, the untreated and 48 hour samples are separated from the other two along the second coefficient. However, the second and third coefficients still do not contribute much to ability to classify the samples.

D.1.7. $1800-1650\text{ cm}^{-1}$ (5.6-6.1 μm).

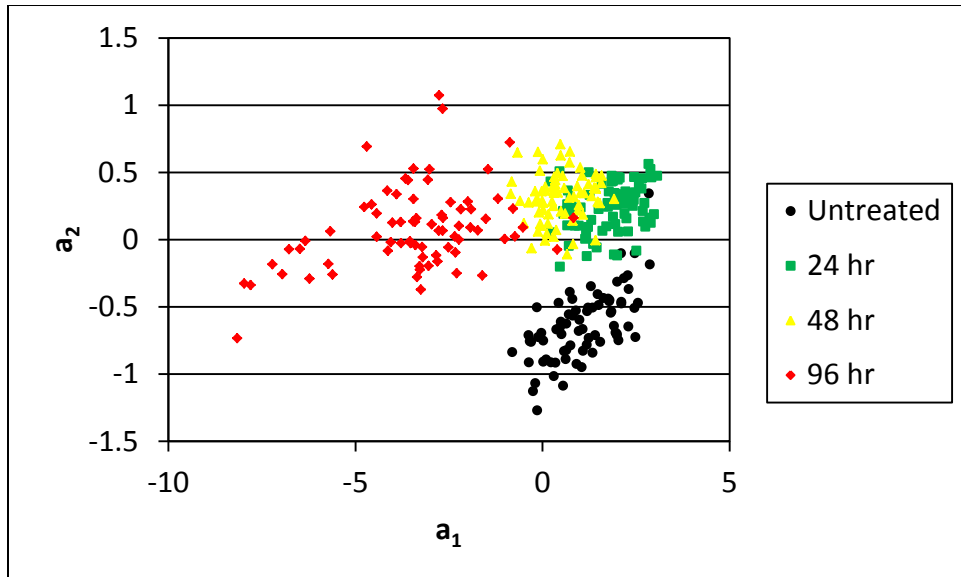


Figure D.19: Plot of the first two coefficients in the $1800-1650\text{ cm}^{-1}$ band for sample set B. This band shows relatively poor separation between the samples when compared to the other bands.

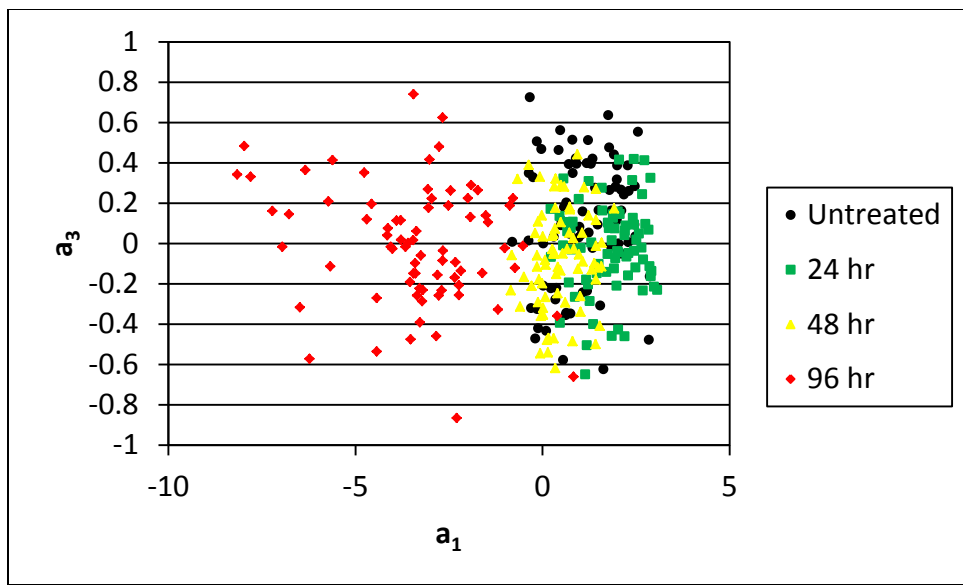


Figure D.20: Plot of the first and third coefficients in the $1800-1650\text{ cm}^{-1}$ band for sample set B. While the 96 hour sample is separated from the others, it is not clustered very tightly and the untreated, 24 hour, and 48 hour samples are on top of each other.

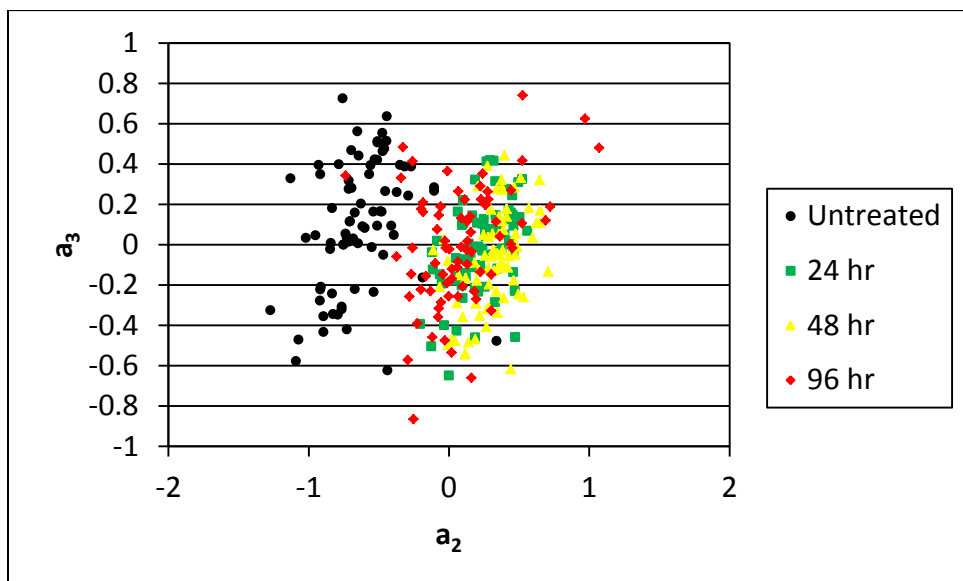


Figure D.21: Plot of the second and third coefficients in the $1800-1650\text{ cm}^{-1}$ band for sample set B. The untreated sample is separated from the others, but the second and third coefficients still do not contribute much to ability to classify the samples.

D.1.8. $1800-800$ minus $1500-1200$ cm^{-1} .

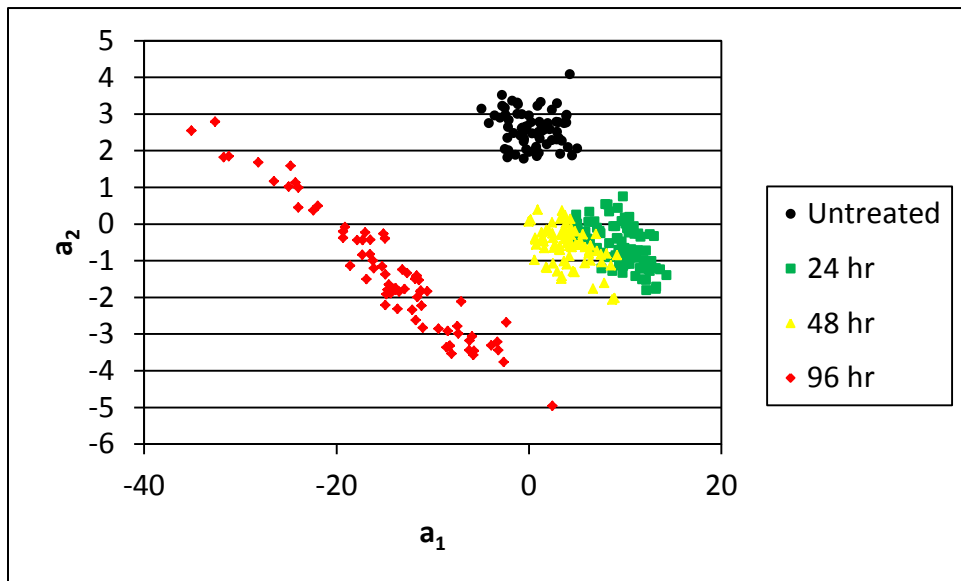


Figure D.22: Plot of the first two coefficients in the $1800-800$ minus $1500-1200$ cm^{-1} band for sample set B. The $1500-1200$ cm^{-1} band was subtracted from $1800-800$ cm^{-1} band to see if it improved the clustering and separation between samples. Looking at figure D.10, the subtraction of the band did not noticeably improve the clustering or separation.

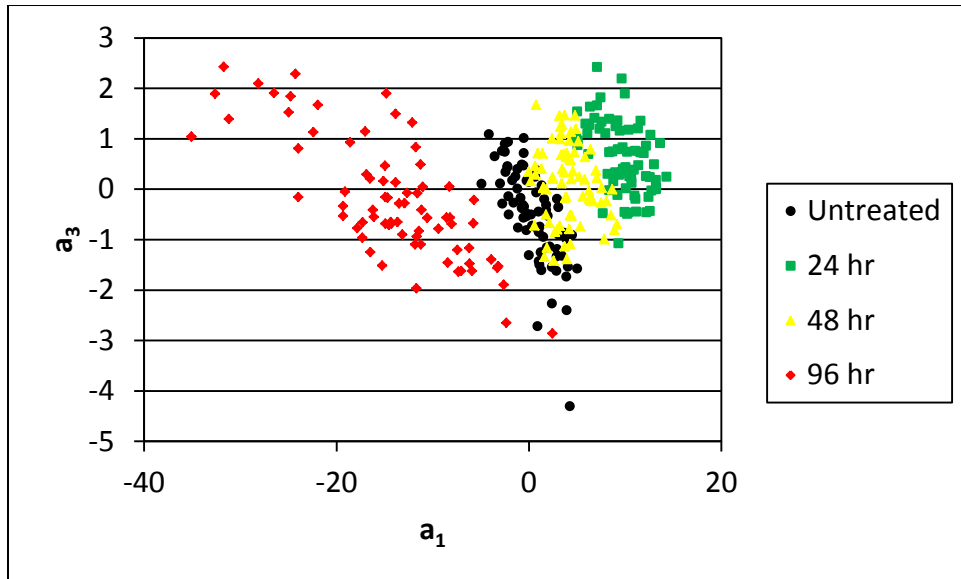


Figure D.23: Plot of the first and third coefficients in the $1800-800$ minus $1500-1200$ cm^{-1} band for sample set B. There is some clustering of the samples, but the third coefficient does not contribute much like most of the bands.

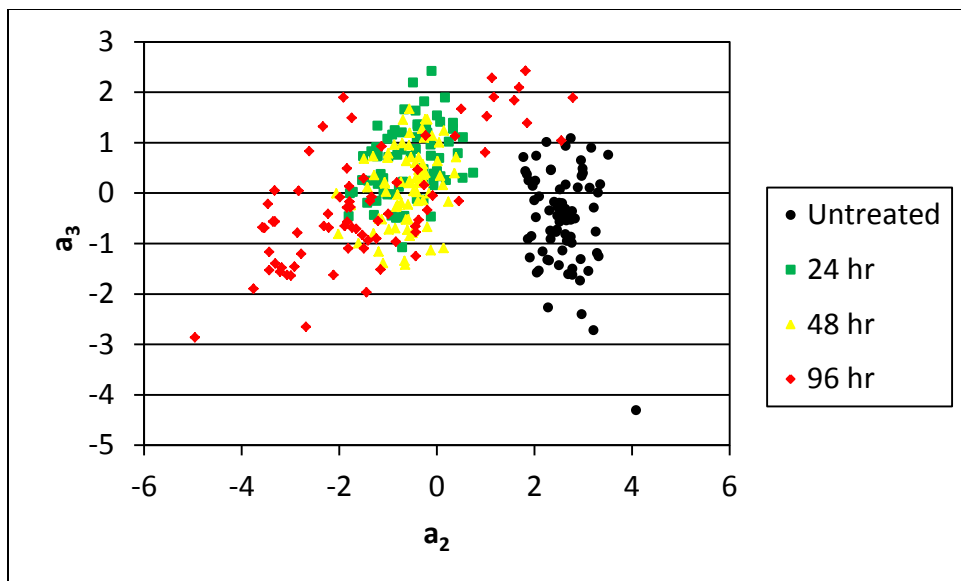


Figure D.24: Plot of the second and third coefficients in the 1800-800 minus 1500-1200 cm^{-1} band for sample set B. The untreated sample is separated from the other three along the second coefficient, but as shown with the other bands, the second and third coefficients do contribute much to classifying the samples.

D.2. Spot to Spot Variation

Figures D.25-D.40 are plots of the a_1 vs. a_3 and a_2 vs. a_3 coefficients for samples B1-B4 in the $1220-850 \text{ cm}^{-1}$ (8.2-11.8 μm) and $1800-1200 \text{ cm}^{-1}$ (5.6-8.3 μm) bands. The main discussion about sample surface uniformity can be found in Chapter 4. These figures are included here for completeness.

D.2.1. Untreated Sample (B1).

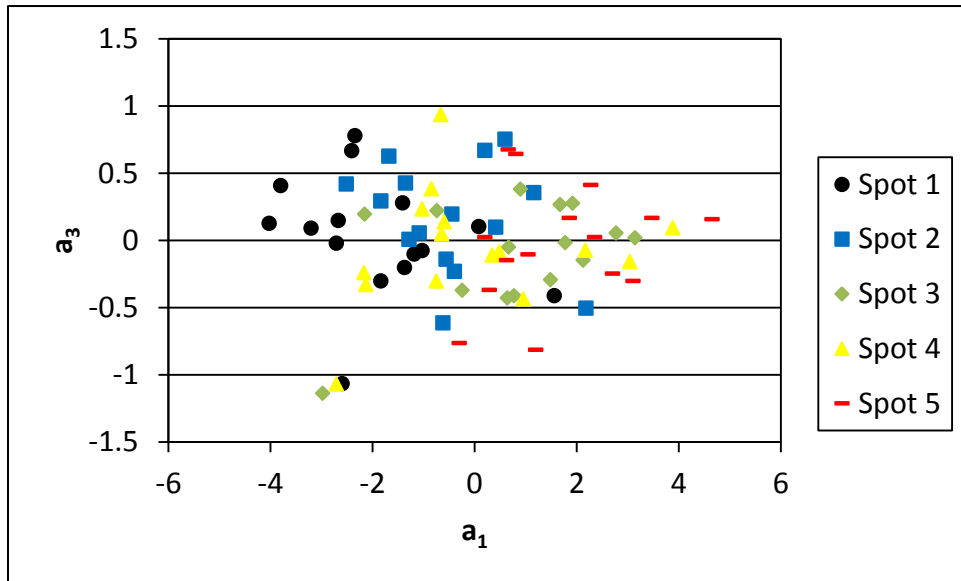


Figure D.25: A plot of the first and third coefficients by spot for sample B1 in the $1220-850\text{ cm}^{-1}$ band. There is some separation in the first coefficient between spots 1 and 5, but there is no separation in the third coefficient.

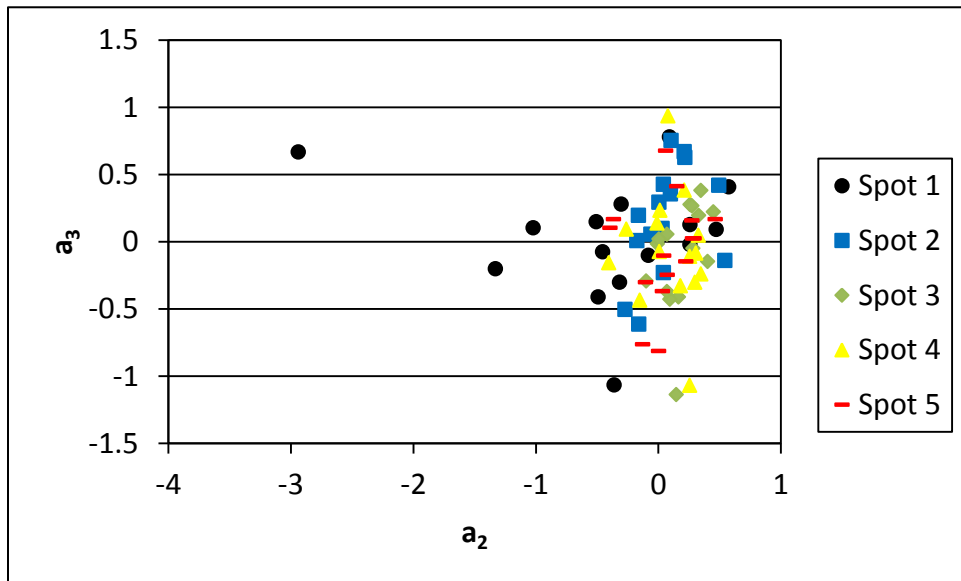


Figure D.26: A plot of the second and third coefficients by spot for sample B1 in the $1220-850\text{ cm}^{-1}$ band. While there are some outliers in the second coefficient for spot 1, there is no separation between the spots in the second or third coefficients.

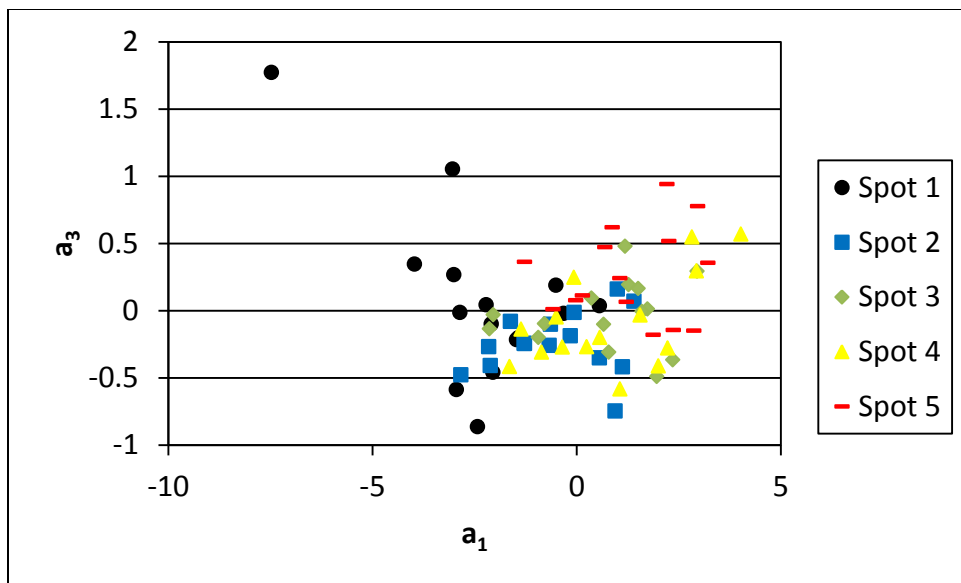


Figure D.27: A plot of the first and third coefficients by spot for sample B1 in the $1800\text{-}1200\text{ cm}^{-1}$ band. As with the $1220\text{-}850\text{ cm}^{-1}$ band, there is some separation in the first coefficient between spots 1 and 5, but there is no separation in the third coefficient.

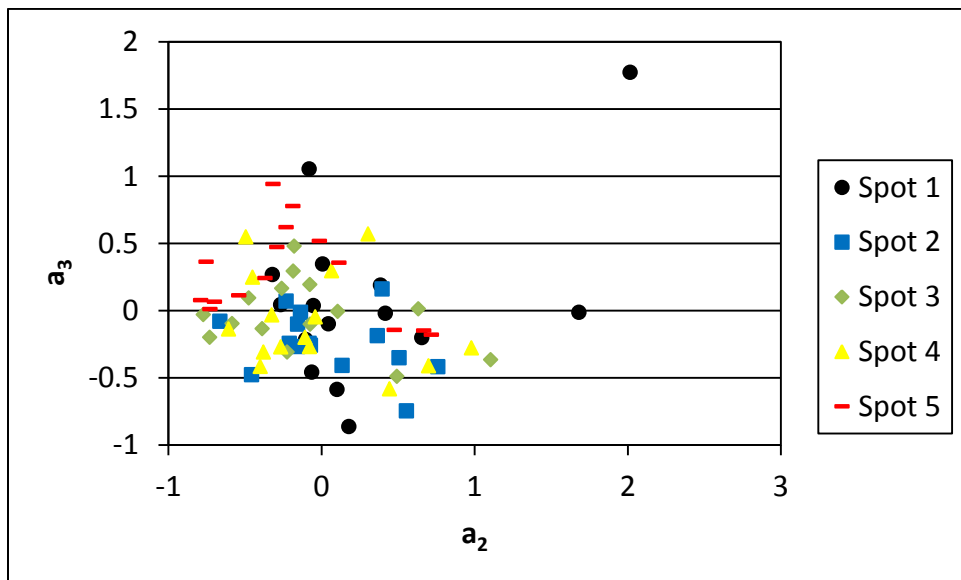


Figure D.28: A plot of the second and third coefficients by spot for sample B1 in the $1800\text{-}1200\text{ cm}^{-1}$ band. While there are some outliers in the second coefficient for spot 1, there is no separation between the spots in the second or third coefficients.

D.2.2. 24 Hour Treatment (B2).

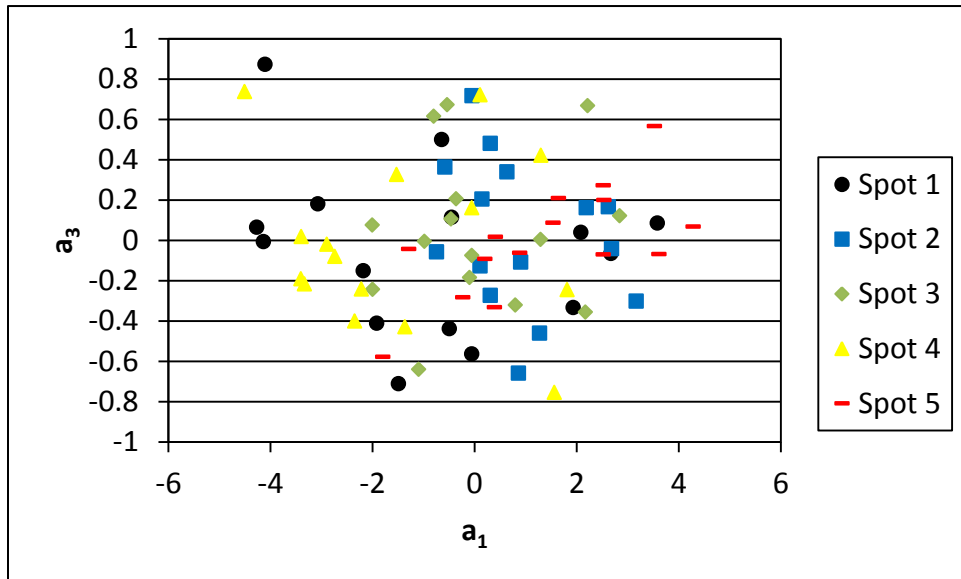


Figure D.29: A plot of the first and third coefficients by spot for sample B2 in the $1220-850\text{ cm}^{-1}$ band. There is no separation between spots in either the first or third coefficient for this band.

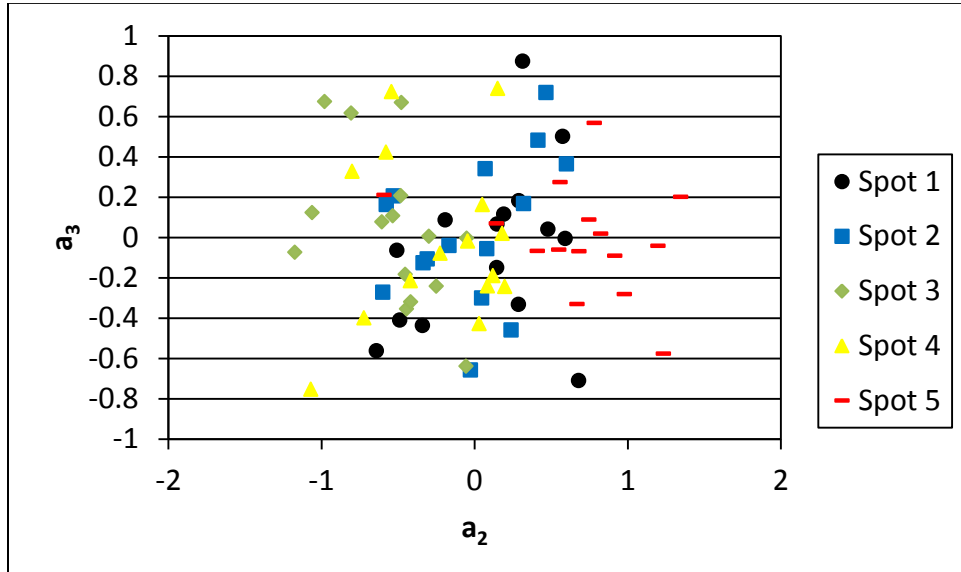


Figure D.30: A plot of the second and third coefficients by spot for sample B2 in the $1220-850\text{ cm}^{-1}$ band. There is some separation between spots 3 and 5 and spots 4 and 5 in the second coefficient for this band, but no separation in the third coefficient.

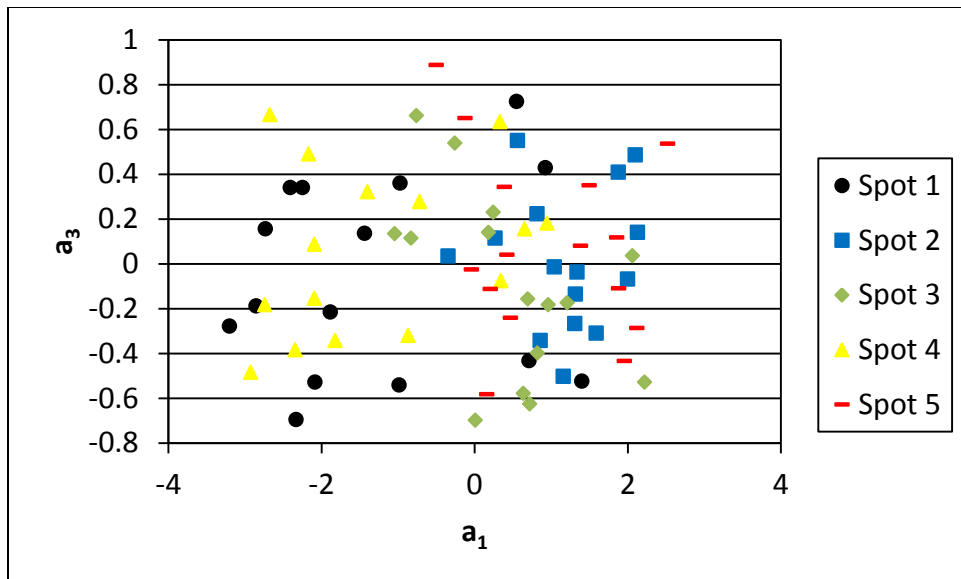


Figure D.31: A plot of the first and third coefficients by spot for sample B2 in the $1800-1200\text{ cm}^{-1}$ band. The majority of the spectra collected for spots 1 and 4 seem to be separated from the rest of the spots in the first coefficient, but there is still significant overlap between the spots. There is no separation in the third coefficient.

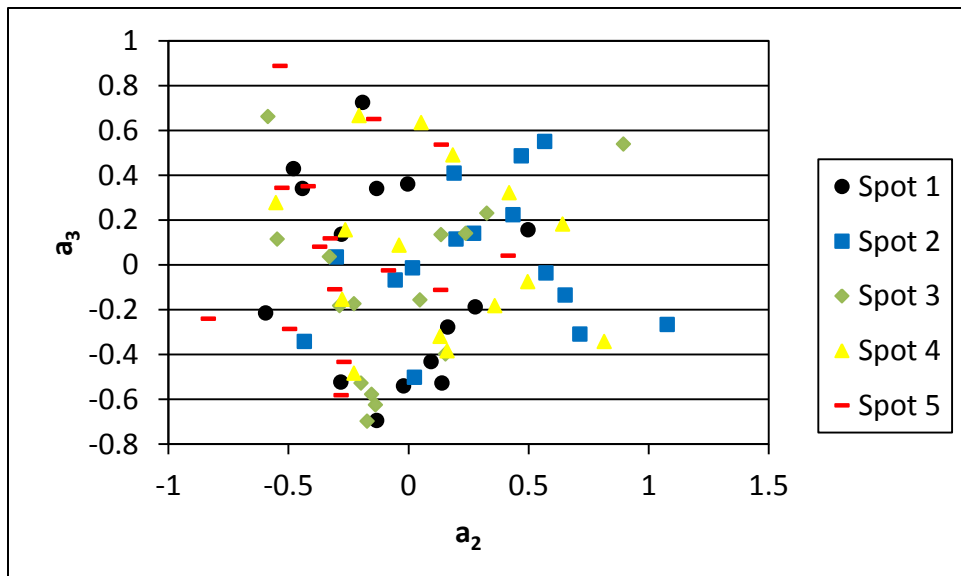


Figure D.32: A plot of the second and third coefficients by spot for sample B2 in the $1800-1200\text{ cm}^{-1}$ band. There is no distinguishability between the spots in the second or third coefficients in this band.

D.2.3. 48 Hour Treatment (B3).

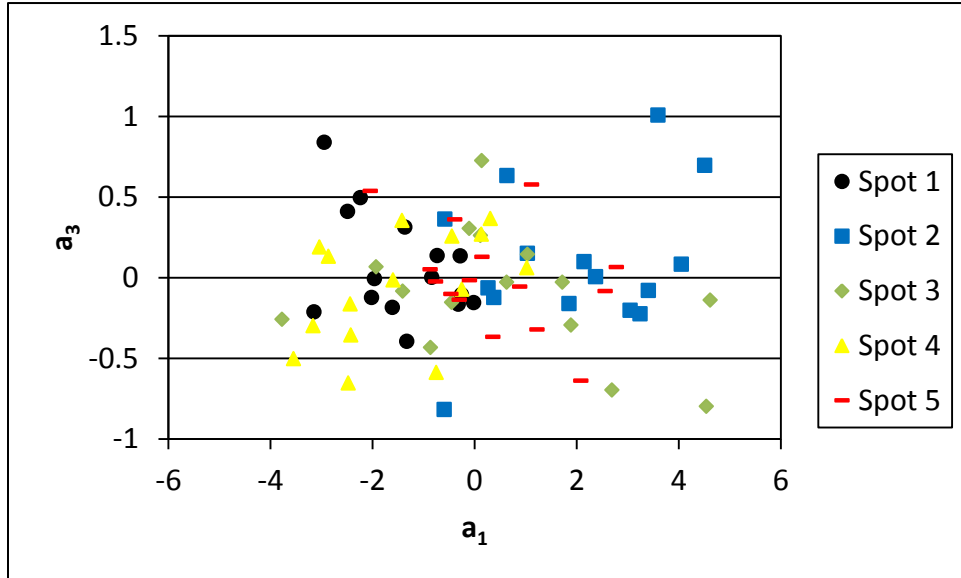


Figure D.33: A plot of the first and third coefficients by spot for sample B3 in the $1220-850\text{ cm}^{-1}$ band. Spots 1 and 2 have some separation in the first coefficient, but there is no separation in the third coefficient between the spots in this band.

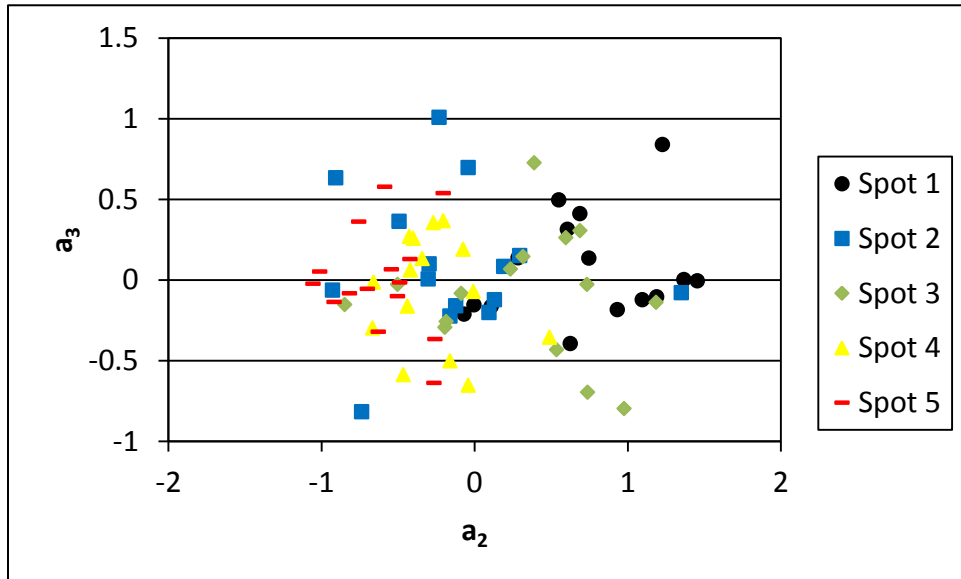


Figure D.34: A plot of the second and third coefficients by spot for sample B3 in the $1220-850\text{ cm}^{-1}$ band. The majority of the spectra for spots 1 and 3 are separated from the rest of the spots in the second coefficient, but there is no separation between the remainder of the spots. The third coefficient has no distinguishability.

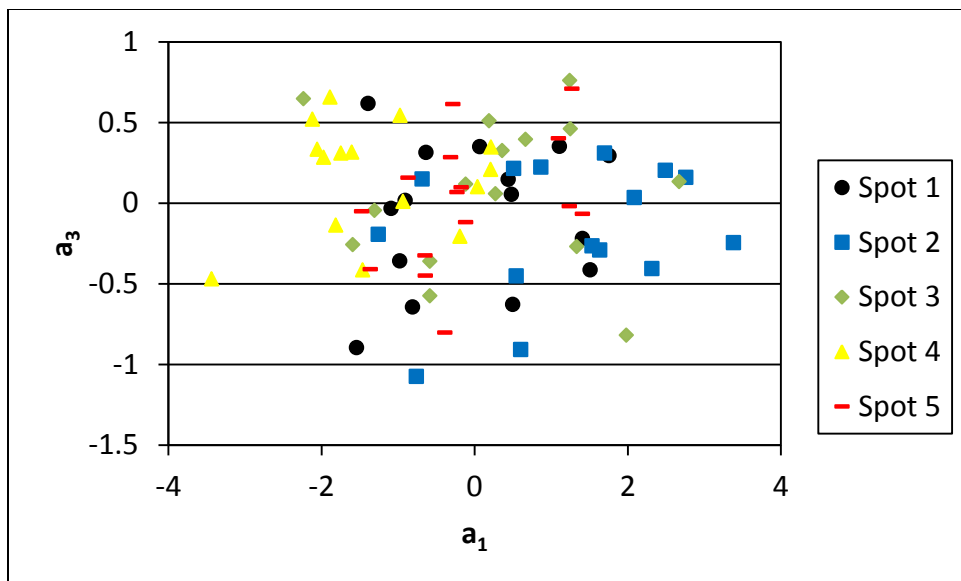


Figure D.35: A plot of the first and third coefficients by spot for sample B3 in the $1800\text{-}1200\text{ cm}^{-1}$ band. There is significant overlap of all the spots in this band in both coefficients.

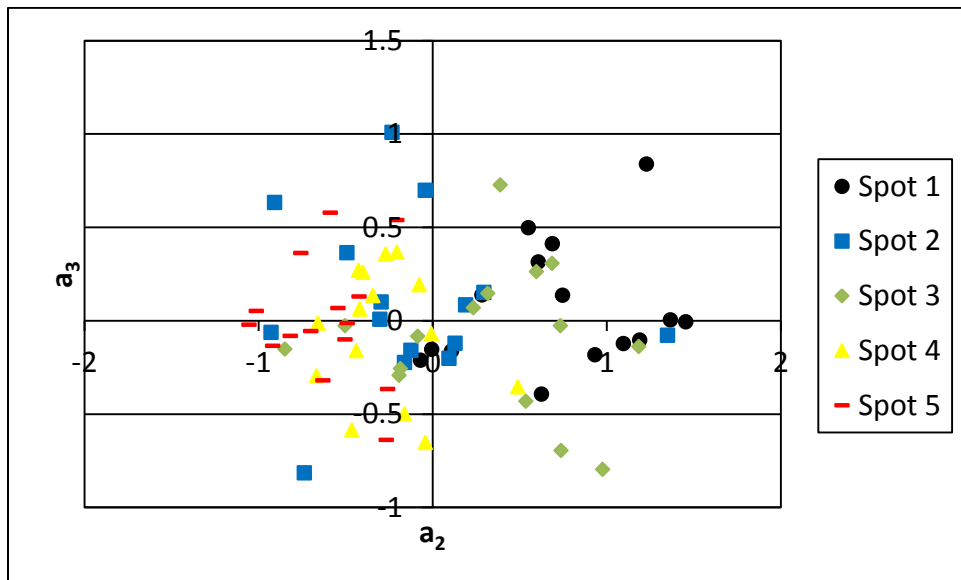


Figure D.36: A plot of the second and third coefficients by spot for sample B3 in the $1800\text{-}1200\text{ cm}^{-1}$ band. Spots 1 and 3 appear separable from the other spots in the second coefficient, but there is no distinguishability between the spots in the third coefficient in this band.

D.2.4. 96 Hour Treatment (B4).

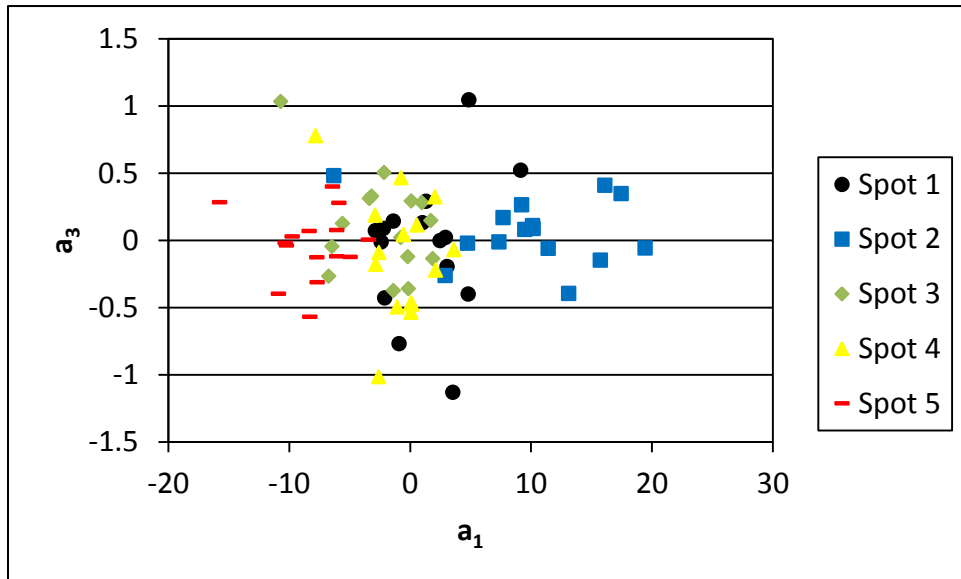


Figure D.37: A plot of the first and third coefficients by spot for sample B4 in the $1220-850\text{ cm}^{-1}$ band. Spots 2, 4 and 5 are clearly separable in the first coefficient, but there is no separation in the third coefficient between the spots in this band.

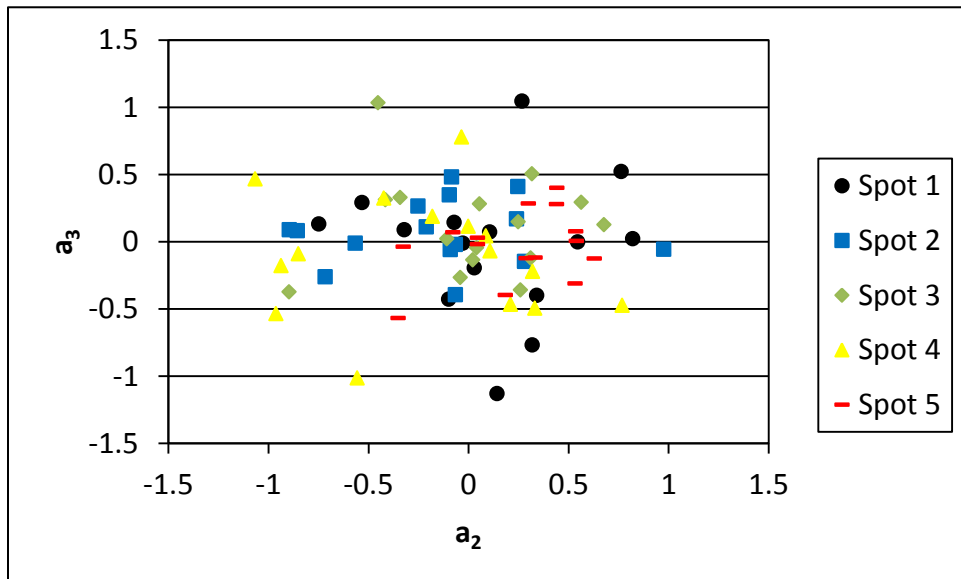


Figure D.38: A plot of the second and third coefficients by spot for sample B4 in the $1220-850\text{ cm}^{-1}$ band. There is no separation between the spots in either coefficient in this band.

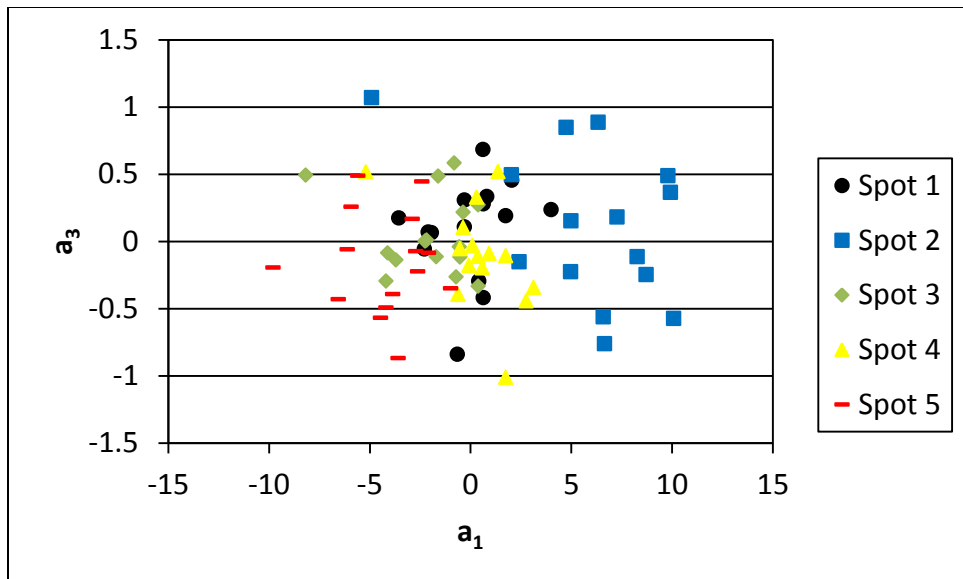


Figure D.39: A plot of the first and third coefficients by spot for sample B4 in the $1800\text{-}1200\text{ cm}^{-1}$ band. As with the $1220\text{-}850\text{ cm}^{-1}$ band, there is separation in the first coefficient between spots 2, 4, and 5. There is no separation in the third coefficient in this band.

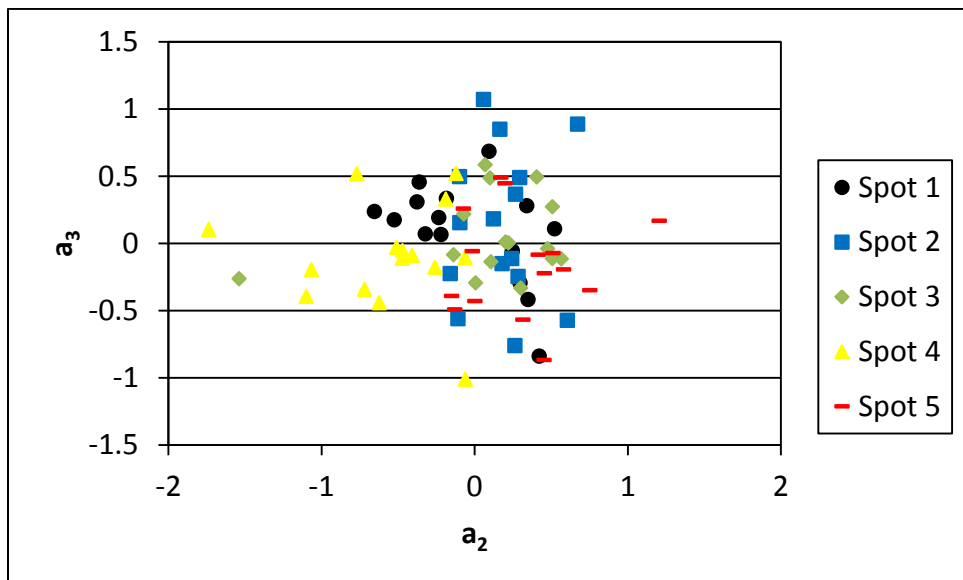


Figure D.40: A plot of the second and third coefficients by spot for sample B4 in the $1800\text{-}1200\text{ cm}^{-1}$ band. Spots 4 and 5 are separable in the second coefficient, but there is no distinguishability between the remainder of the spots. There is no separation in the third coefficient in this band.

D.3. Time-Dependent Behavior

Figures D.41-D.56 are plots of the a_1 vs. a_3 and a_2 vs. a_3 coefficients for samples B1-B4 in the $1220-850\text{ cm}^{-1}$ ($8.2-11.8\text{ }\mu\text{m}$) and $1800-1200\text{ cm}^{-1}$ ($5.6-8.3\text{ }\mu\text{m}$) bands. The main discussion about investigating the existence of time-dependent behavior in the coating material can be found in Chapter 4. These figures are included here for completeness.

D.3.1. Untreated Sample (B1).

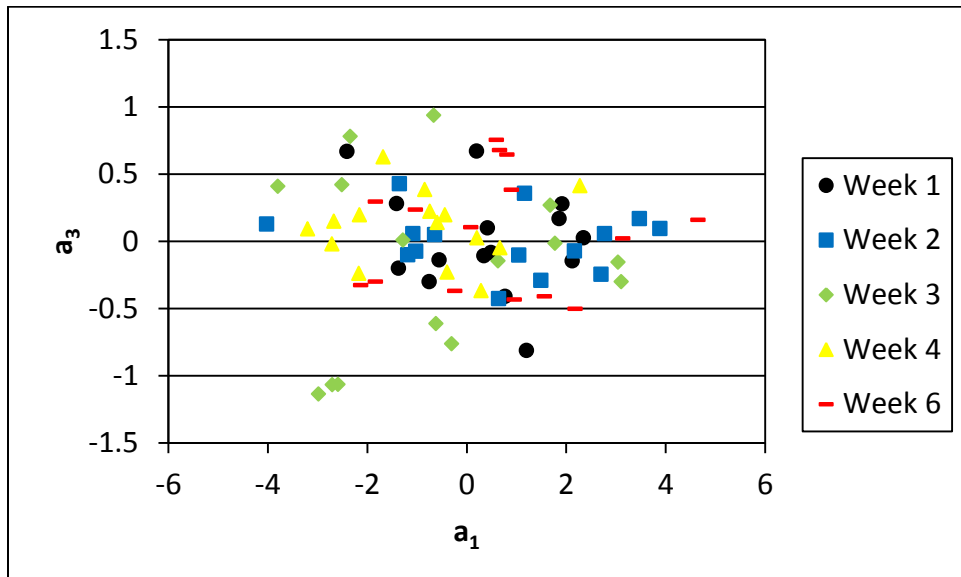


Figure D.41: Plot of the first and third coefficients by week in the $1220-850\text{ cm}^{-1}$ band for sample B1. There is no apparent week to week trend.

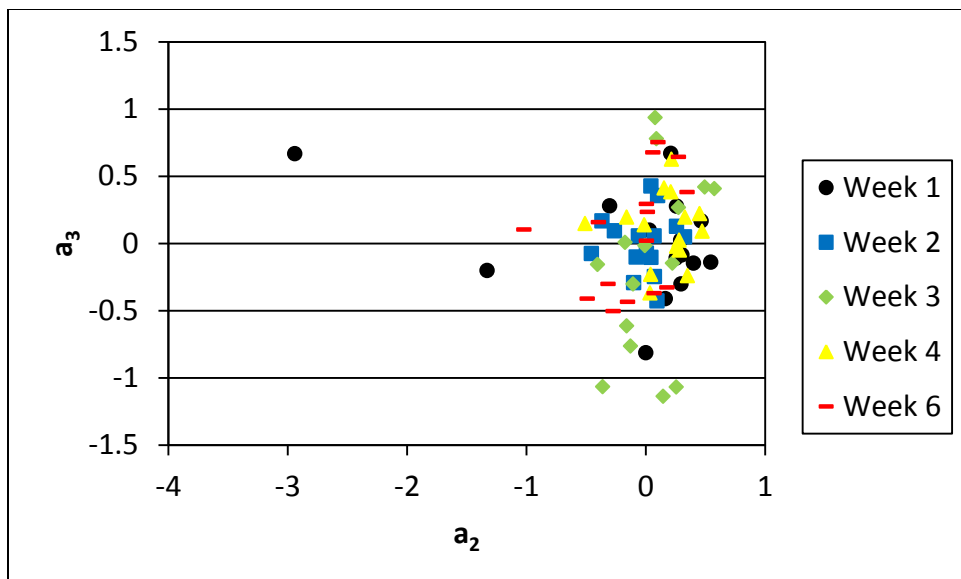


Figure D.42: A plot of the second and third coefficients by week in the $1220\text{-}850\text{ cm}^{-1}$ band for sample B1. There is no week to week trend in the second and third coefficients either.

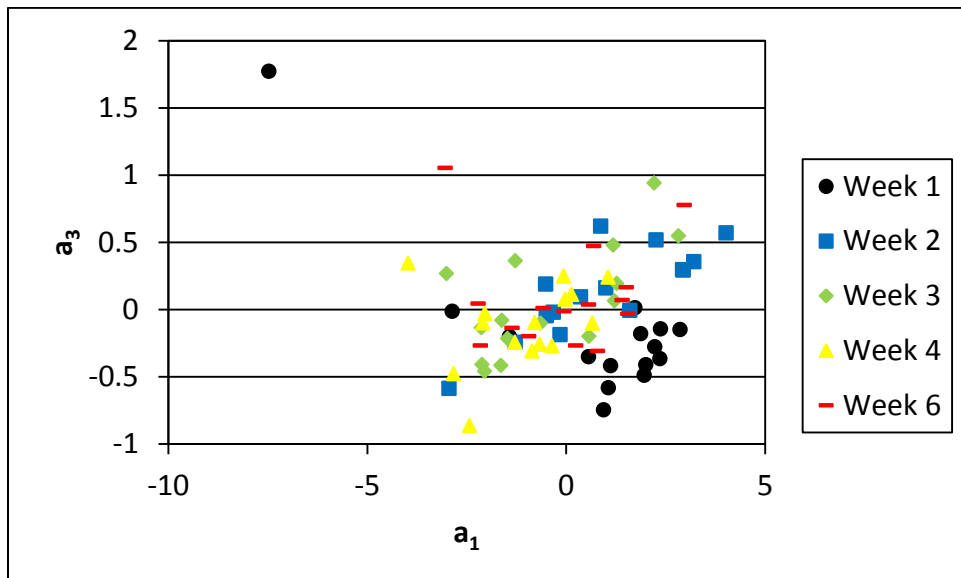


Figure D.43: A plot of the first and third coefficients by week in the $1800\text{-}1200\text{ cm}^{-1}$ band for sample B1. There is no apparent week to week trend in this band either.

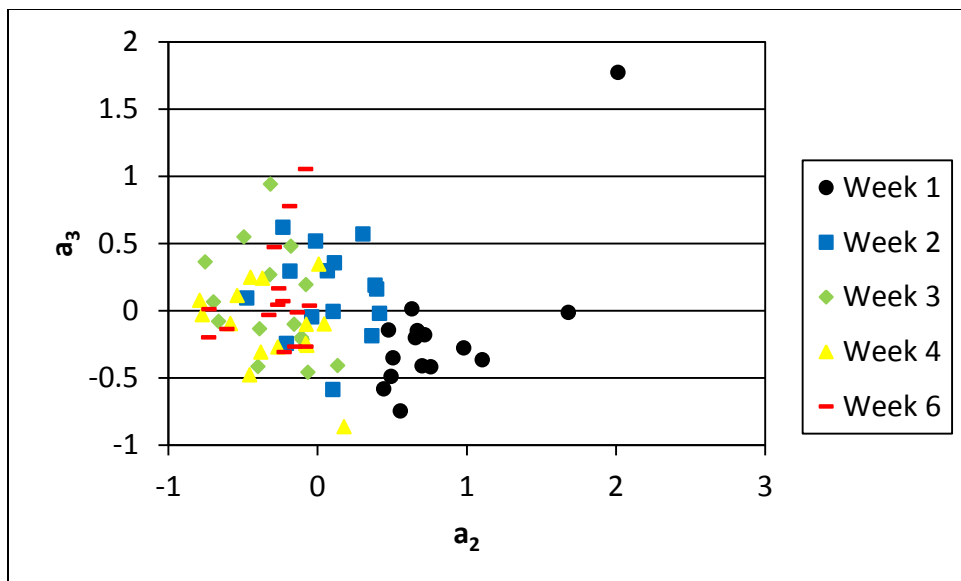


Figure D.44: A plot of the second and third coefficients by week in the $1800\text{-}1200\text{ cm}^{-1}$ band for sample B1. Week 1 is distinguishable from the other weeks, but there is no clear trend for weeks 2-6.

D.3.2. 24 Hour Treatment (B2).

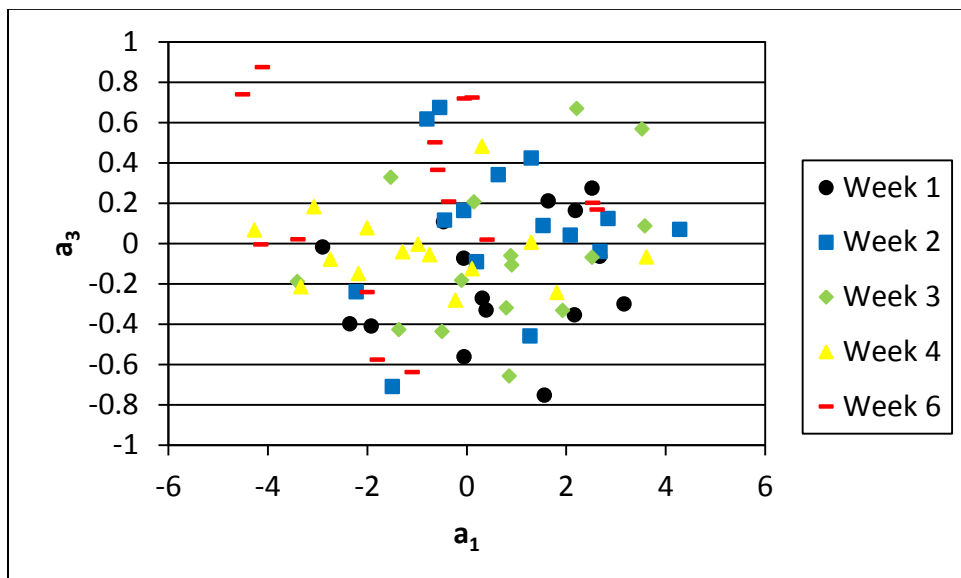


Figure D.45: Plot of the first and third coefficients by week in the $1220\text{-}850\text{ cm}^{-1}$ band for sample B2. There is no apparent week to week trend as there is significant overlap between all the weeks.

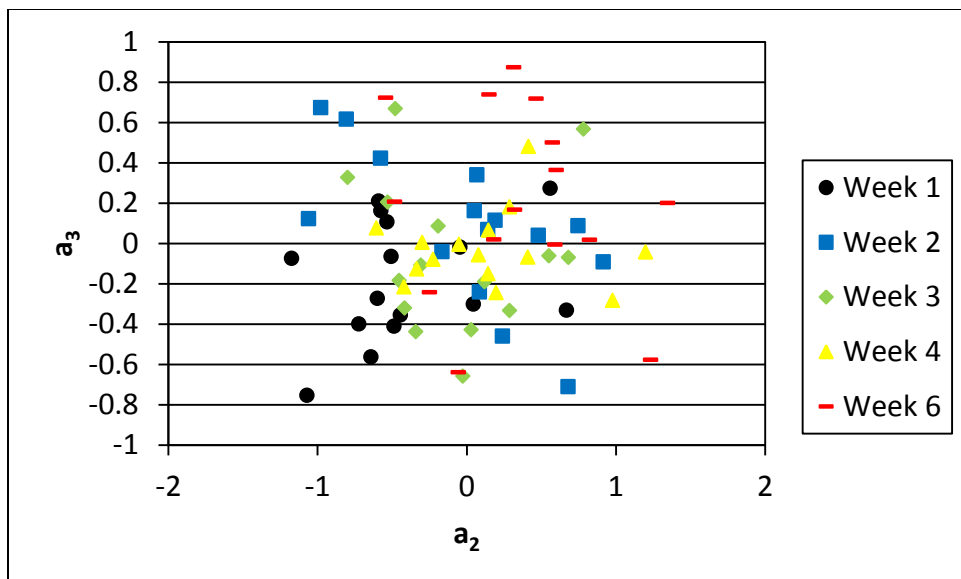


Figure D.46: A plot of the second and third coefficients by week in the $1220\text{-}850\text{ cm}^{-1}$ band for sample B2. There is no week to week trend in the second and third coefficients either.

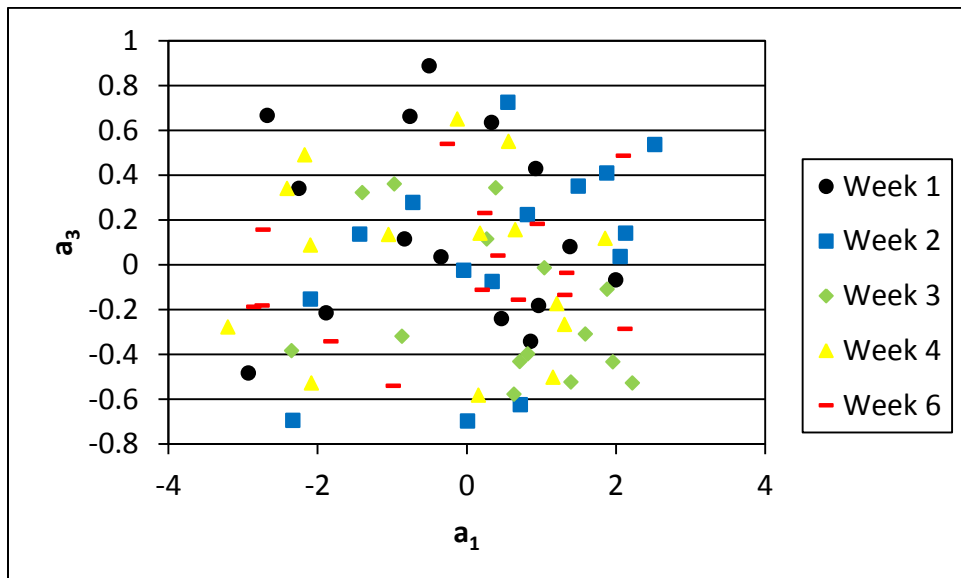


Figure D.47: A plot of the first and third coefficients by week in the $1800\text{-}1200\text{ cm}^{-1}$ band for sample B2. There is no apparent week to week trend in this band either.

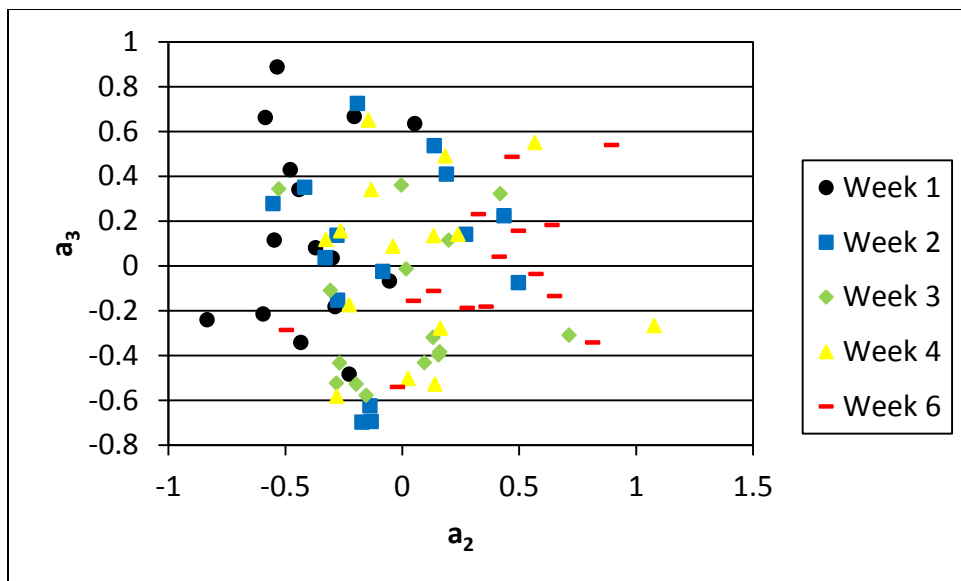


Figure D.48: A plot of the second and third coefficients by week in the $1800\text{-}1200\text{ cm}^{-1}$ band for sample B2. Again, there is no week to week trend in the second and third coefficients in this band.

D.3.3. 48 Hour Treatment (B3).

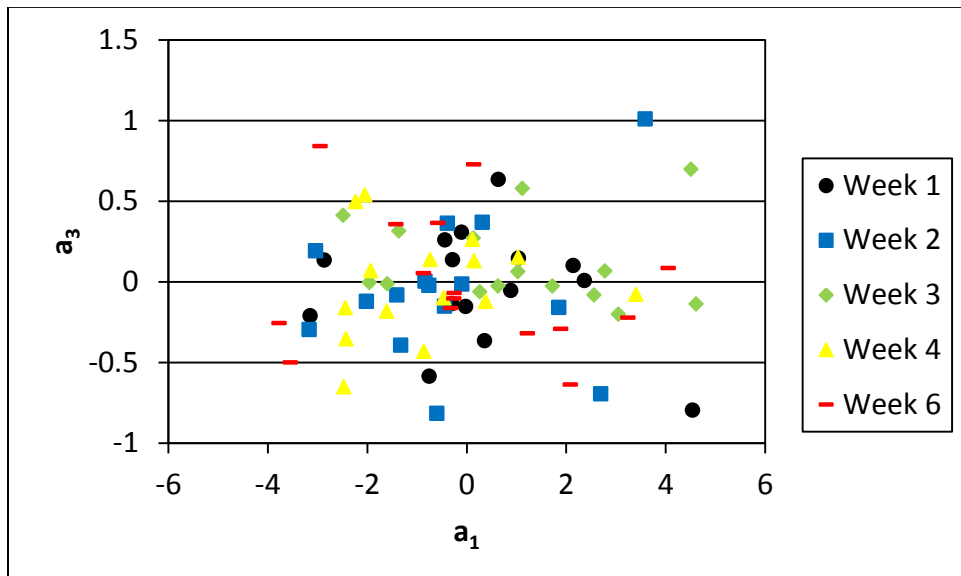


Figure D.49: Plot of the first and third coefficients by week in the $1220\text{-}850\text{ cm}^{-1}$ band for sample B3. There is no apparent week to week trend as there is significant overlap between all the weeks.

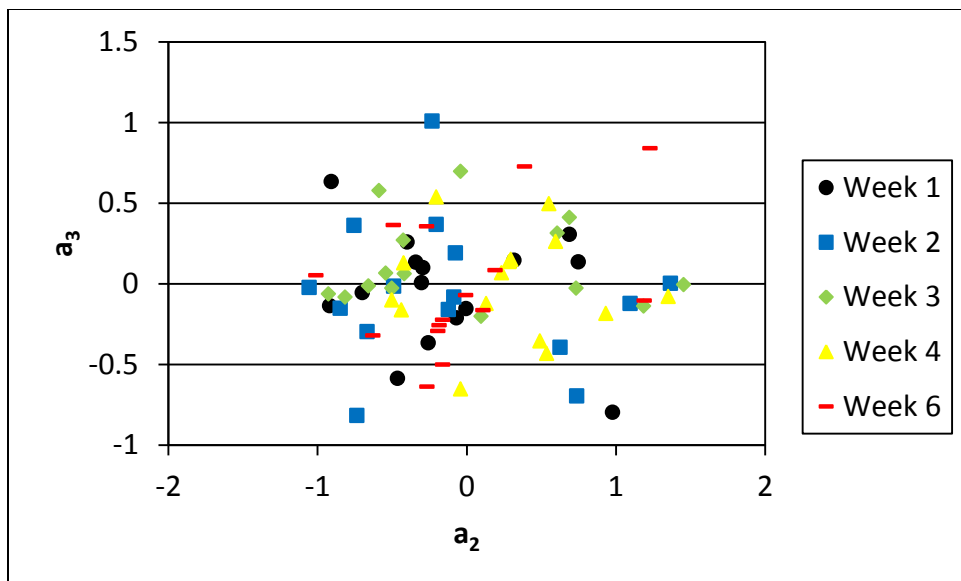


Figure D.50: A plot of the second and third coefficients by week in the $1220-850\text{ cm}^{-1}$ band for sample B3. There is no week to week trend in the second and third coefficients this band.

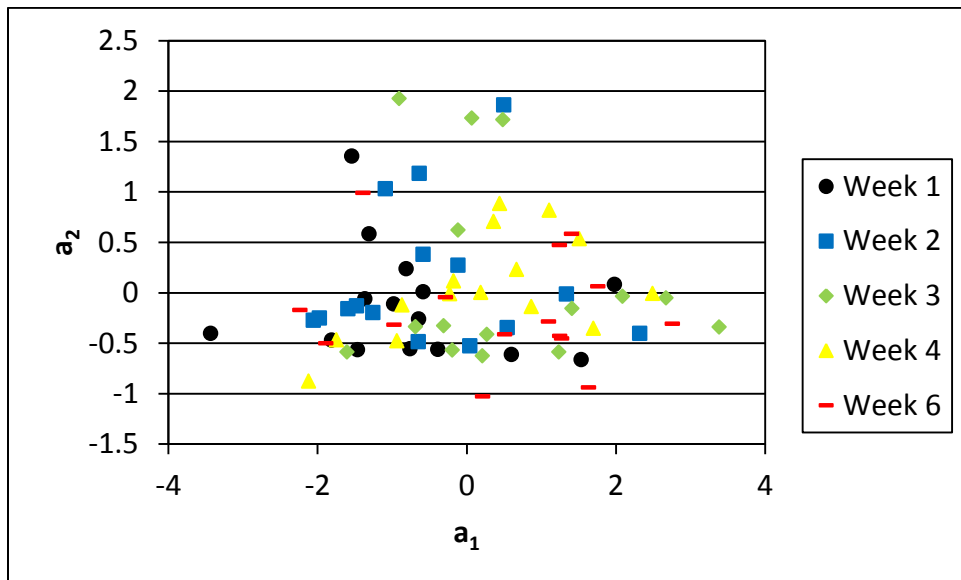


Figure D.51: A plot of the first and second coefficients by week in the $1800-1200\text{ cm}^{-1}$ band for sample B3. There is no separation between the weeks and no apparent trend in this band.

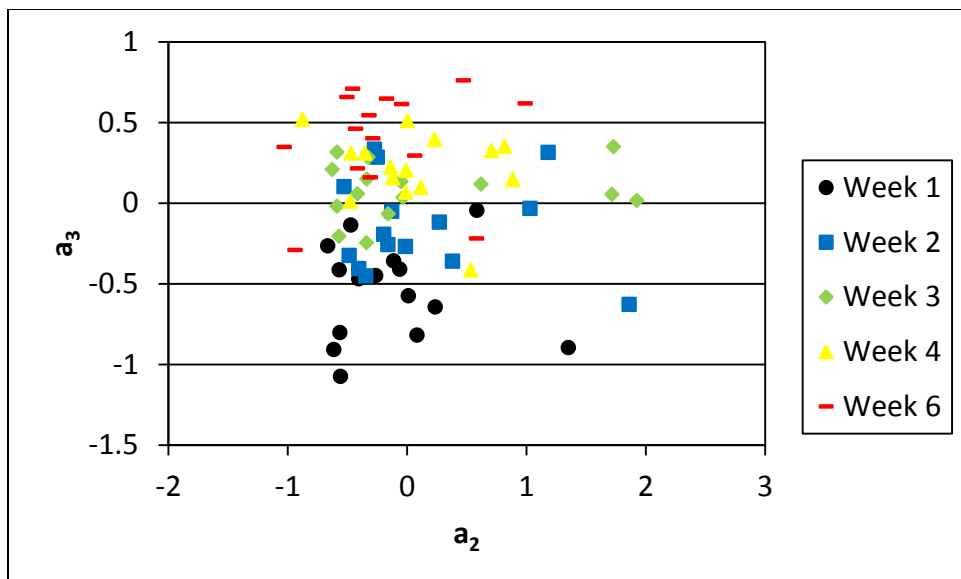


Figure D.52: A plot of the second and third coefficients by week in the $1800\text{-}1200\text{ cm}^{-1}$ band for sample B3. There appears to be some progression along the third coefficient from week to week, but not along the second coefficient.

D.3.4. 96 Hour Treatment (B4).

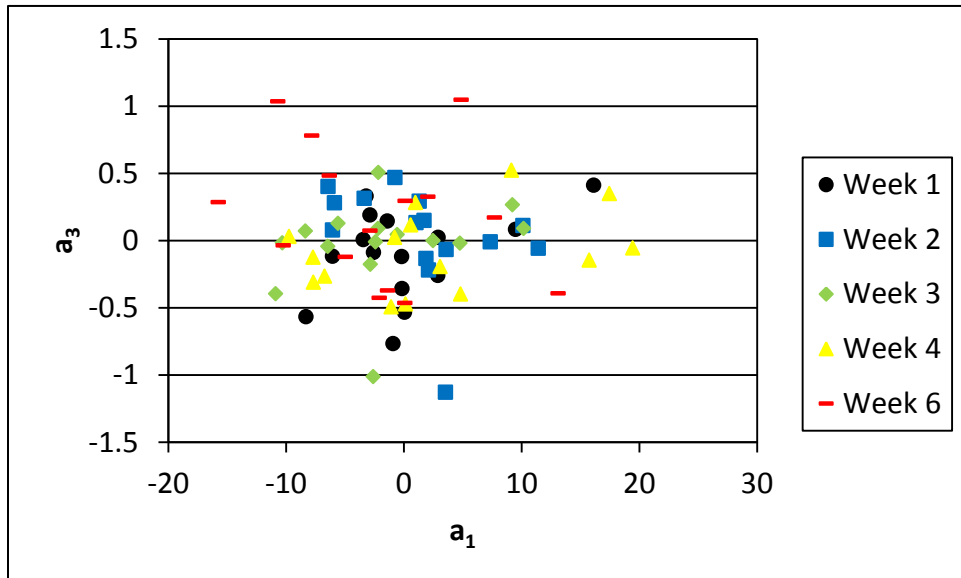


Figure D.53: Plot of the first and third coefficients by week in the $1220\text{-}850\text{ cm}^{-1}$ band for sample B4. As with the other samples, there is no apparent week to week trend as there is significant overlap between all the weeks.

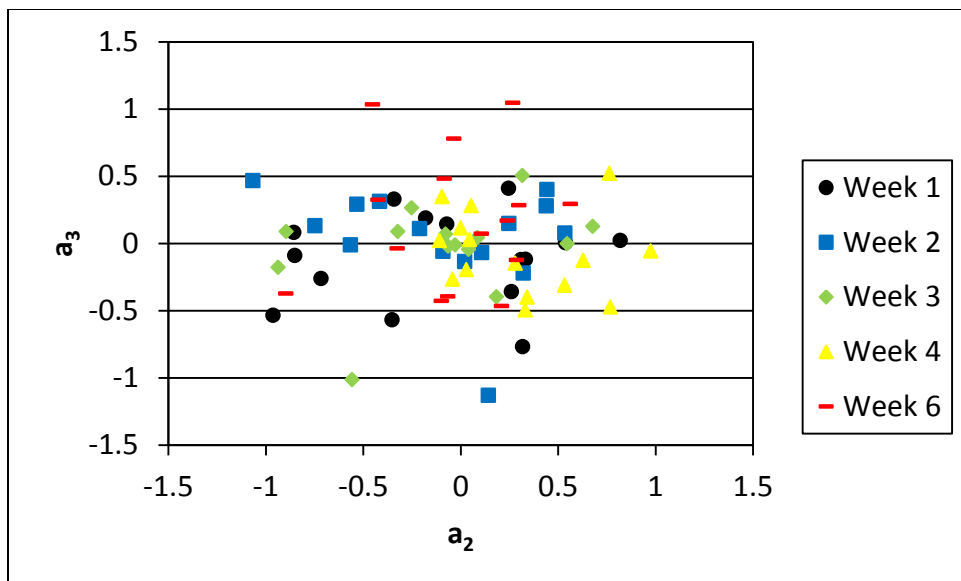


Figure D.54: A plot of the second and third coefficients by week in the $1220\text{-}850\text{ cm}^{-1}$ band for sample B4. There is no week to week trend in the second and third coefficients this band.

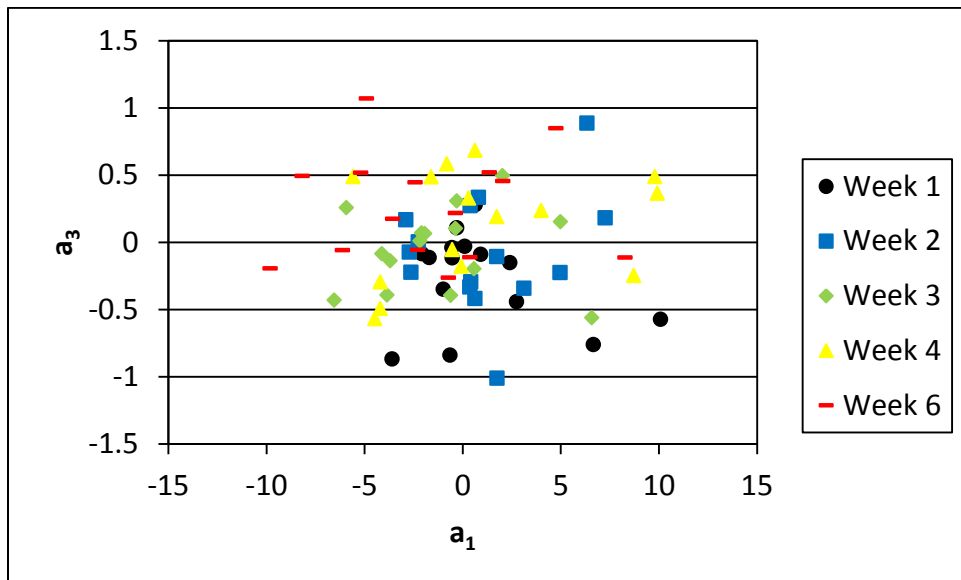


Figure D.55: A plot of the first and third coefficients by week in the $1800\text{-}1200\text{ cm}^{-1}$ band for sample B4. There is no separation between the weeks and no apparent trend in this band.

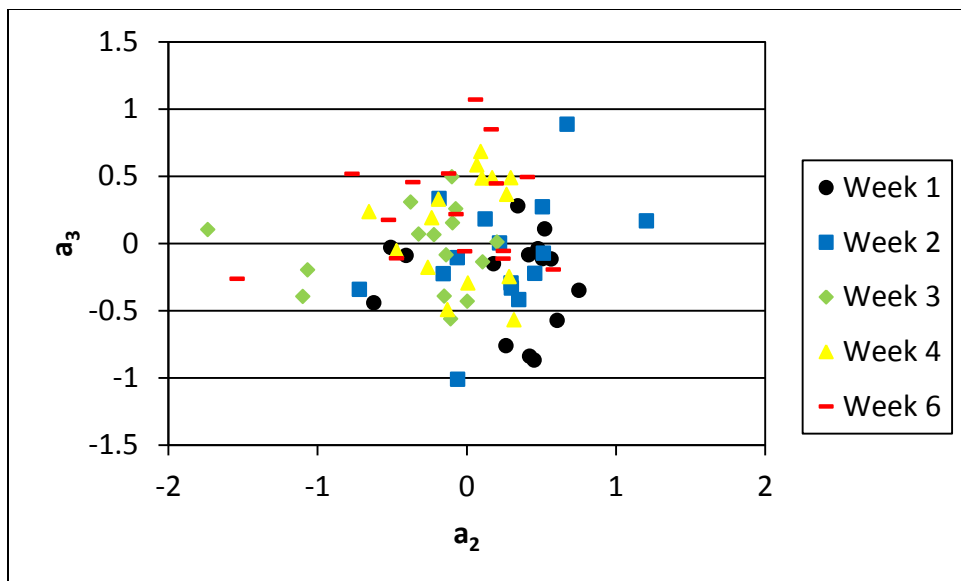


Figure D.56: A plot of the second and third coefficients by week in the $1800-1200\text{ cm}^{-1}$ band for sample B4. There is no trend in the second or third coefficient for sample B4 in this band.

Appendix E. Discriminant Analysis Data

Table E.1: Confusion matrix and error rates for the $1150-850 \text{ cm}^{-1}$ band using both the first two and first three SVD coefficients to generate the classifier.

1150-850 (cm⁻¹)	2 Coefficients	Predict		Resubstitution Error %	Number of Errors (#/300)	Kfold Error (10 Fold) %
		Truth	0 hr			
		0 hr	75	0	0	3.33
		24 hr	0	70	5	0
		48 hr	1	4	70	0
		96 hr	0	0	0	75
	3 Coefficients	0hr	73	0	2	0
		24 hr	1	71	3	0
		48 hr	0	3	72	0
		96 hr	0	0	0	75

Table E.2: Confusion matrix and error rates for the $1150-1050 \text{ cm}^{-1}$ band using both the first two and first three SVD coefficients to generate the classifier.

1150-1050 (cm⁻¹)	2 Coefficients	Predict		Resubstitution Error %	Number of Errors (#/300)	Kfold Error (10 Fold) %
		Truth	0 hr			
		0 hr	71	0	4	0
		24 hr	0	71	4	0
		48 hr	1	6	68	0
		96 hr	0	0	0	75
	3 Coefficients	0hr	75	0	0	0
		24 hr	0	70	5	0
		48 hr	0	4	71	0
		96 hr	0	0	0	75

Table E.3: Confusion matrix and error rates for the $1200-800 \text{ cm}^{-1}$ band using both the first two and first three SVD coefficients to generate the classifier.

1200-800 (cm^{-1})	2 Coefficients	Predict	0 hr	24 hr	48 hr	96 hr	Resubstitution Error %	Number of Errors (#/300)	Kfold Error (10 Fold) %
		Truth							
0 hr		0 hr	75	0	0	0	3.33	10	3.33
		24 hr	0	70	5	0			
		48 hr	1	4	70	0			
		96 hr	0	0	0	75			
3 Coefficients		0hr	74	0	1	0	2.67	8	2.33
		24 hr	0	72	3	0			
		48 hr	0	4	71	0			
		96 hr	0	0	0	75			

Table E.4: Confusion matrix and error rates for the $1800-800 \text{ cm}^{-1}$ band using both the first two and first three SVD coefficients to generate the classifier.

1800-800 (cm^{-1})	2 Coefficients	Predict	0 hr	24 hr	48 hr	96 hr	Resubstitution Error %	Number of Errors (#/300)	Kfold Error (10 Fold) %
		Truth							
0 hr		0 hr	75	0	0	0	7.67	23	7.33
		24 hr	0	64	11	0			
		48 hr	0	12	63	0			
		96 hr	0	0	0	75			
3 Coefficients		0hr	75	0	0	0	2.67	8	3.0
		24 hr	0	71	4	0			
		48 hr	0	4	71	0			
		96 hr	0	0	0	75			

Table E.5: Confusion matrix and error rates for the $1800-1200 \text{ cm}^{-1}$ band using both the first two and first three SVD coefficients to generate the classifier.

1800-1200 (cm ⁻¹)	2 Coefficients	Predict	0 hr	24 hr	48 hr	96 hr	Resubstitution Error %	Number of Errors (#/300)	Kfold Error (10 Fold) %
		Truth							
0 hr		0 hr	73	2	0	0	8.33	25	8.33
		24 hr	0	71	4	0			
		48 hr	0	14	61	0			
		96 hr	0	4	1	70			
3 Coefficients		0hr	73	2	0	0	8.0	24	8.67
		24 hr	0	71	4	0			
		48 hr	0	14	61	0			
		96 hr	0	4	0	71			

Table E.6: Confusion matrix and error rates for the $1800-1450 \text{ cm}^{-1}$ band using both the first two and first three SVD coefficients to generate the classifier.

1800-1450 (cm ⁻¹)	2 Coefficients	Predict	0 hr	24 hr	48 hr	96 hr	Resubstitution Error %	Number of Errors (#/300)	Kfold Error (10 Fold) %
		Truth							
0 hr		0 hr	72	2	1	0	8.67	26	9.33
		24 hr	1	71	3	0			
		48 hr	0	13	62	0			
		96 hr	0	4	2	69			
3 Coefficients		0hr	74	0	1	0	7.0	21	8.67
		24 hr	0	73	2	0			
		48 hr	0	13	62	0			
		96 hr	0	4	1	70			

Table E.7: Confusion matrix and error rates for the $1800-1650\text{ cm}^{-1}$ band using both the first two and first three SVD coefficients to generate the classifier.

1800-1650 (cm ⁻¹)	2 Coefficients	Predict	0 hr	24 hr	48 hr	96 hr	Resubstitution Error %	Number of Errors (#/300)	Kfold Error (10 Fold) %
		Truth							
0 hr		0 hr	72	3	0	0	11.33	34	11.67
		24 hr	0	63	12	0			
		48 hr	0	10	65	0			
		96 hr	0	2	7	66			
3 Coefficients		0hr	72	3	0	0	12.0	36	12.0
		24 hr	0	62	13	0			
		48 hr	0	11	64	0			
		96 hr	0	0	9	66			

Table E.8: Confusion matrix and error rates for the $1800-800$ minus $1500-1200\text{ cm}^{-1}$ band using both the first two and first three SVD coefficients to generate the classifier.

[1800-800] - [1500-1200] (cm ⁻¹)	2 Coefficients	Predict	0 hr	24 hr	48 hr	96 hr	Resubstitution Error %	Number of Errors (#/300)	Kfold Error (10 Fold) %
		Truth							
0 hr		0 hr	75	0	0	0	4.33	13	4.33
		24 hr	1	68	6	0			
		48 hr	0	6	69	0			
		96 hr	0	0	0	75			
3 Coefficients		0hr	75	0	0	0	2.67	8	2.67
		24 hr	0	71	4	0			
		48 hr	0	4	71	0			
		96 hr	0	0	0	75			

Appendix F. Data Normalization and SVD Details

F.1. Effect of Normalization on SVD Coefficient Clustering

During the defense of this work, the committee asked that the author investigate whether or not the normalization of each spectra, before the SVD analysis was applied, would tighten the coefficient clusters. It was posited that if this normalization tightened the clusters, it would reduce or eliminate the overlap between samples, thus increasing the accuracy of the discriminant analysis. The normalization was conducted in LabVIEW on the entire spectrum as well as the $1220-850 \text{ cm}^{-1}$ band. The results of the normalization for the $1220-850 \text{ cm}^{-1}$ band are shown in figures F.1 and F.2 below.

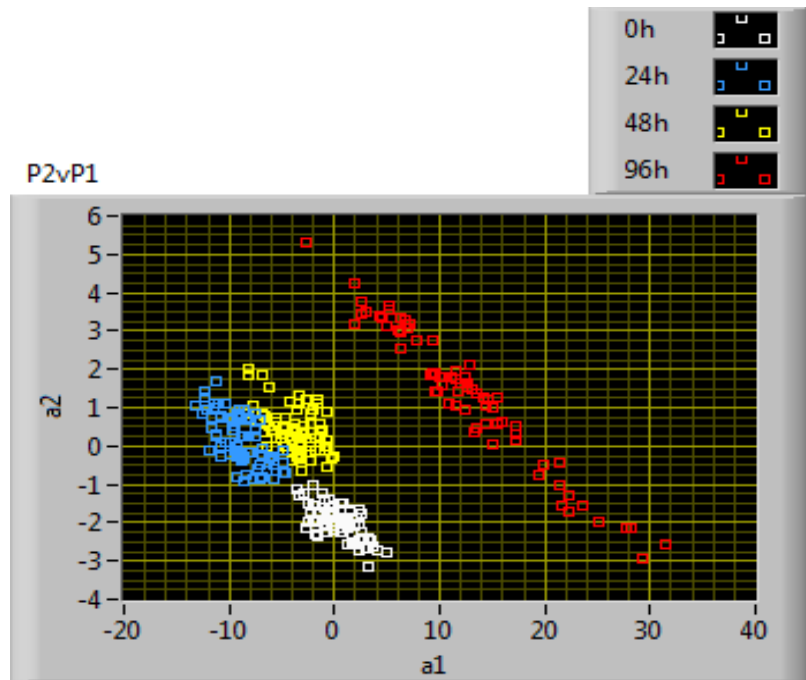


Figure F.1: Plot of the first two SVD coefficients for sample set B in the $1220-850 \text{ cm}^{-1}$ band without normalization.

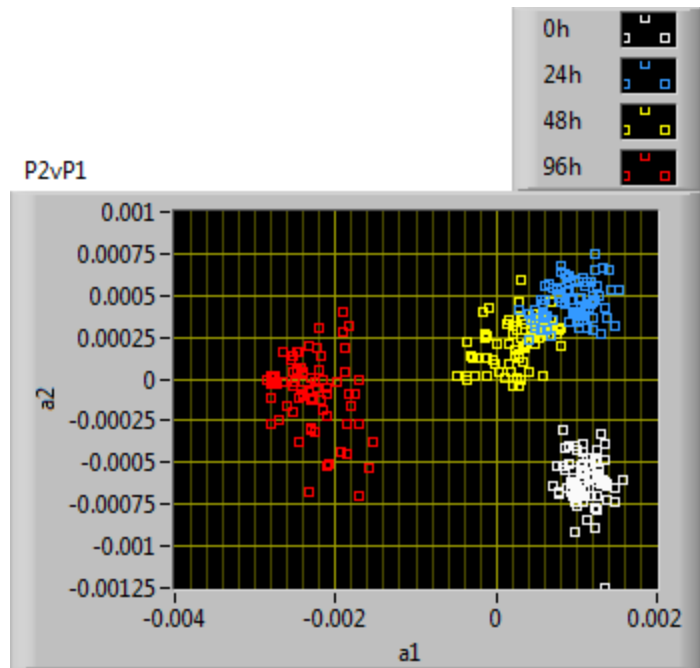


Figure F.2: Plot of the first two SVD coefficients for sample set B in the $1220-850\text{ cm}^{-1}$ band with normalization. The coefficient clusters for the untreated and 96 hr samples tightened, but the overlap between the 24 and 48 hour samples increased.

Figures F.1 and F.2 are plots of the first two SVD coefficients for sample set B in the $1220-850\text{ cm}^{-1}$ band before and after normalization, respectively. While the untreated and 96 hour samples do show a tightening of the coefficient clusters, the overlap between the 24 and 48 hour samples increased. The increased overlap will reduce the ability of discriminant analysis to discern the sample degradation levels. The effect of normalization on the entire band was much worse, so the results were not included here.

F.2. SVD Details

In addition to the investigation into the effects of normalization on the data, questions were asked about the basis vectors and relative importance of the basis vectors to describing the data. It is common to present this information during the discussion when publishing to give the reader insight into the underlying basis vectors as well as how much of the data variance is being captured by each. As mentioned in section 4.3, data with high SNR will often have a primary basis vector that captures upwards of 85% of the data variance. Again, LabVIEW was used to calculate the magnitudes of the basis vectors for the 1220-850 cm⁻¹ band and the results are shown in figures F.3 and F.4 below. As expected from the coefficient plots in chapter 4 and appendix D, the first basis vector captures significantly more data variance than the rest. However, what was unexpected was how low the value was for the first basis vector relative to published values for experimental data in the literature. The general trend showing a significant reduction in relative importance for subsequent basis vectors does agree with the expected behavior. This plot confirms that higher order terms (a_4 and above) can be neglected for classification purposes because they are capturing noise in the measurement.

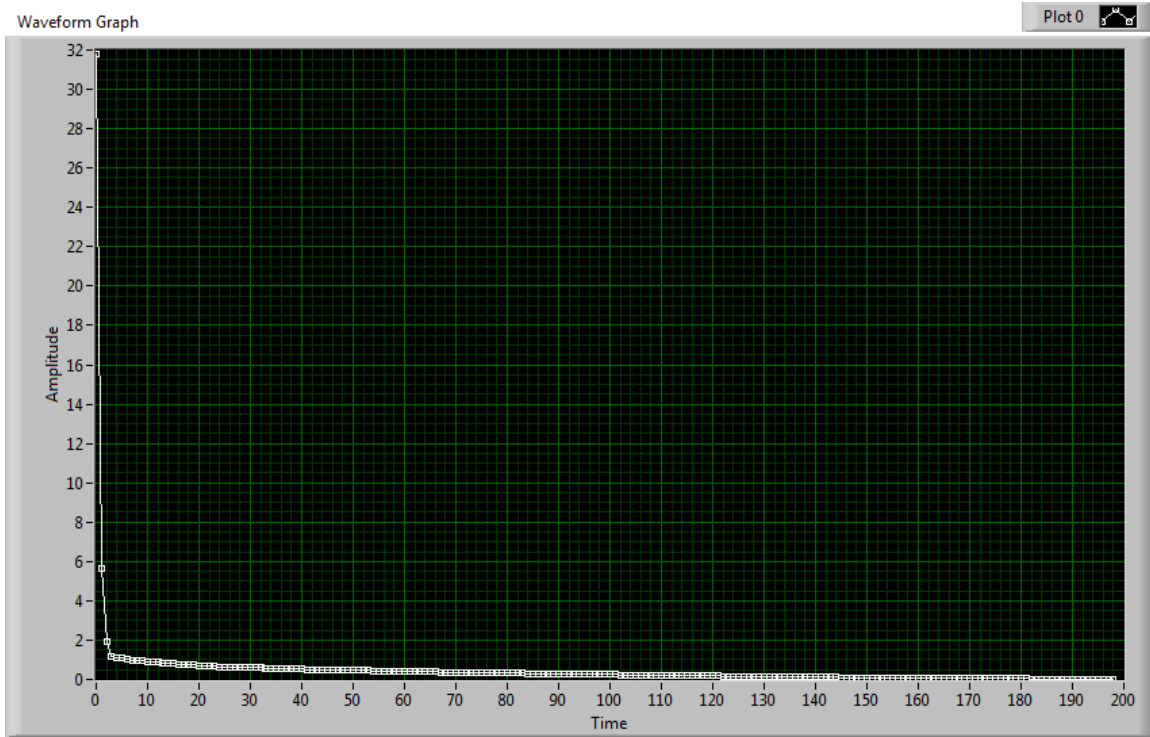


Figure F.3: Plot of the percent of the data variance captured by each basis vector generated by SVD for sample set B in the $1220-850\text{ cm}^{-1}$ band. While the first basis vector is lower than anticipated (31.7%), the significant reduction in magnitude for subsequent basis vectors shows that higher order terms (a_4 and above) are capturing noise and can be neglected for discrimination purposes.

The first three basis vectors for sample set B in the $1220-850\text{ cm}^{-1}$ band are plotted in figure F.4. Since a mean subtraction was conducted on the data before the SVD basis vectors and coefficients were calculated, the first basis vector is primarily capturing the deviation from the mean reflectance for each wavenumber interrogated. Had the mean subtraction not been done first, the first basis vector would have resembled the mean reflectance.

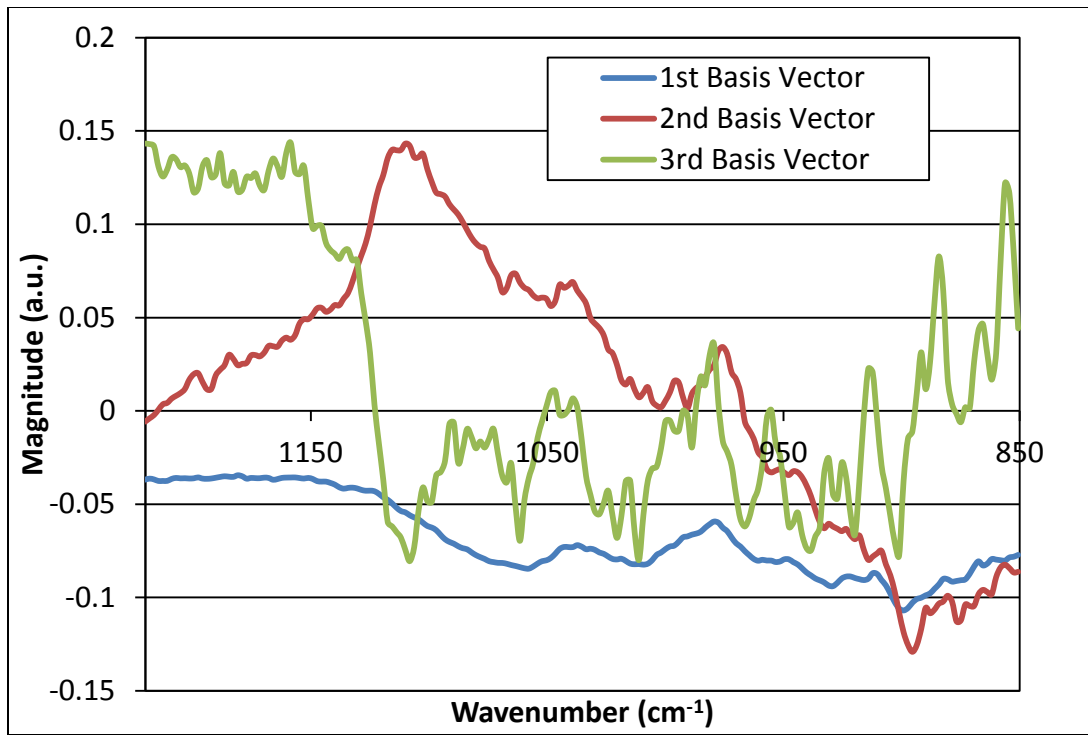


Figure F.4: Plot of the first three basis vectors for sample set B in the $1220-850\text{ cm}^{-1}$ band. The third basis vector largely represents measurement noise relative to the first two basis vectors.

Some measurement noise is contained the second basis vector while the third basis vector is mostly capturing noise. This is further evidence that the coefficients calculated from the higher order basis vectors are negligible for classification purposes.

References

- [1] W. E. Kosik, "Mechanisms of Military Coatings Degradation Final Technical Report," Weapons and Materials Directorate Army Research Laboratory, Aberdeen Proving Grounds, MD, 2003.
- [2] G. Grundmeier and M. Stratmann, "Adhesion and De-adhesion Mechanisms at Polymer/Metal Interfaces: Mechanistic Understanding Based on In Situ Studies of Buried Interfaces," *Annu. Rev. Mater. Res.*, vol. 35, no. 1, pp. 571–615, Aug. 2005.
- [3] D. A. Forman, R. Baty, E. F. Herzberg, A. R. Kelly, M. V Kumaran, and N. T. O'Meara, "The Annual Cost of Corrosion for Air Force Aircraft and Missile Equipment," 2009.
- [4] Department of the Air Force, *T.O.33B-1-1: Nondestructive Inspection Methods, Basic Theory*. Tinker AFB: AFRL/RXS-OL, 2013.
- [5] X. F. Yang, J. Li, S. G. Croll, D. E. Tallman, and G. P. Bierwagen, "Degradation of Low Gloss Polyurethane Aircraft Coatings Under UV and Prohesion Alternating Exposures," *Polym. Degrad. Stab.*, vol. 80, no. 1, pp. 51–58, Jan. 2003.
- [6] X. F. Yang, D. E. Tallman, G. P. Bierwagen, S. G. Croll, and S. Rohlik, "Blistering and Degradation of Polyurethane Coatings Under Different Accelerated Weathering Tests," *Polym. Degrad. Stab.*, vol. 77, no. 1, pp. 103–109, 2002.
- [7] X. F. Yang, D. E. Tallman, S. G. Croll, and G. P. Bierwagen, "Morphological Changes in Polyurethane Coatings on Exposure to Water," *Polym. Degrad. Stab.*, vol. 77, no. 3, pp. 391–396, 2002.
- [8] X. F. Yang, C. Vang, D. E. Tallman, G. P. Bierwagen, S. G. Croll, and S. Rohlik, "Weathering Degradation of a Polyurethane Coating," *Polym. Degrad. Stab.*, vol. 74, no. 2, pp. 341–351, 2001.
- [9] M. Szycher, *Szycher's Handbook of Polyurethanes*, Second. Boca Raton, FL: Taylor & Francis Group, 1999.
- [10] D. Y. Perera, "Effect of Pigmentation on Organic Coating Characteristics," *Prog. Org. Coatings*, vol. 50, no. 4, pp. 247–262, Sep. 2004.
- [11] D. Y. Perera, "Physical Ageing of Organic Coatings," *Prog. Org. Coatings*, vol. 47, no. 1, pp. 61–76, Jul. 2003.

- [12] I. Yilgor, E. Yilgor, I. G. Guler, T. C. Ward, and G. L. Wilkes, "FTIR Investigation of the Influence of Diisocyanate Symmetry on the Morphology Development in Model Segmented Polyurethanes," *Polymer (Guildf.)*, vol. 47, no. 11, pp. 4105–4114, May 2006.
- [13] S. G. Croll, X. Shi, and B. M. D. Fernando, "The Interplay of Physical Aging and Degradation during Weathering for Two Crosslinked Coatings," *Prog. Org. Coatings*, vol. 61, no. 2–4, pp. 136–144, Feb. 2008.
- [14] D. Y. Perera, "Effect of Thermal and Hygroscopic History on Physical Ageing of Organic Coatings," *Prog. Org. Coatings*, vol. 44, no. 1, pp. 55–62, 2002.
- [15] M. R. Kamal and R. Saxon, "Recent Developments in the Analysis and Prediction of the Weatherability of Plastics," *Appl. Polym. Symp.*, vol. 4, pp. 1–28, 1967.
- [16] B. W. Johnson and R. McIntyre, "Analysis of Test Methods for UV Durability Polymer Coatings," *Prog. Org. Coatings*, vol. 27, pp. 95–106, 1996.
- [17] Y. Leng, "Vibrational Spectroscopy," in *Materials Characterization: Introduction to Microscopic and Spectroscopic Methods*, 1st ed., John Wiley & Sons, 2008, pp. 253–297.
- [18] S. F. Sun, "Infrared Spectroscopy," in *Physical Chemistry of Macromolecules: Basic Principles and Issues*, 2nd ed., John Wiley & Sons, 2004, pp. 420–430.
- [19] C. S. Hsu, "Infrared Spectroscopy," in *Handbook of Instrumental Techniques for Analytical Chemistry*, F. A. Settle, Ed. Prentice-Hall, pp. 247–284.
- [20] L. Mariey, J. P. Signolle, C. Amiel, and J. Travert, "Discrimination, Classification, Identification of Microorganisms Using FTIR Spectroscopy and Chemometrics," *Vib. Spectrosc.*, vol. 26, no. 2, pp. 151–159, Nov. 2001.
- [21] F. A. Settle, *Handbook of Instrumental Techniques for Analytical Chemistry*. Upper Saddle River: Prentice-Hall, 1997.
- [22] J. Coates, "Interpretation of Infrared Spectra, A Practical Approach," in *Encyclopedia of Analytical Chemistry*, John Wiley & Sons, Ltd, 2006.
- [23] R. J. Barnes, M. S. Dhanoa, and S. J. Lister, "Standard Normal Variate Transformation and De-trending of Near-Infrared Diffuse Reflectance Spectra," *Appl. Spectrosc.*, vol. 43, no. 5, pp. 772–777, 1989.

[24] R. A. Viscarra Rossel, D. J. J. Walvoort, A. B. McBratney, L. J. Janik, and J. O. Skjemstad, "Visible, Near Infrared, Mid Infrared or Combined Diffuse Reflectance Spectroscopy for Simultaneous Assessment of Various Soil Properties," *Geoderma*, vol. 131, no. 1–2, pp. 59–75, Mar. 2006.

[25] S. R. Culler, M. T. McKenzie, L. J. Fina, H. Ishida, and J. L. Koenig, "Fourier Transform Diffuse Reflectance Infrared Study of Polymer Films and Coatings: A Method for Studying Polymer Surfaces," *Appl. Spectrosc.*, vol. 38, no. 6, pp. 791–795, 1984.

[26] S. Wold, K. Esbensen, and P. Geladi, "Principal Component Analysis," *Chemom. Intell. Lab. Syst.*, vol. 2, no. 1–3, pp. 37–52, Aug. 1987.

[27] M. Wall, A. Rechtsteiner, and L. Rocha, "Singular Value Decomposition and Principal Component Analysis," in *A Practical Approach to Microarray Data Analysis SE - 5*, D. Berrar, W. Dubitzky, and M. Granzow, Eds. Springer US, 2003, pp. 91–109.

[28] J. Shlens, "A Tutorial on Principal Component Analysis," 2009. [Online]. Available: <http://www.snl.salk.edu/~shlens/pca.pdf>. [Accessed: 05-Mar-2014].

[29] R. A. FISHER, "The Use of Multiple Measurements in Taxonomic Problems," *Ann. Eugen.*, vol. 7, no. 2, pp. 179–188, Sep. 1936.

[30] H. Yang, J. Irudayaraj, and M. M. Paradkar, "Discriminant Analysis of edible Oils and Fats by FTIR, FT-NIR and FT-Raman Spectroscopy," *Food Chem.*, vol. 93, no. 1, pp. 25–32, Nov. 2005.

[31] W. Zhao, A. Krishnaswamy, R. Chellappa, D. Swets, and J. Weng, "Discriminant Analysis of Principal Components for Face Recognition," in in *Face Recognition SE - 4*, vol. 163, H. Wechsler, P. J. Phillips, V. Bruce, F. Soulié, and T. Huang, Eds. Springer Berlin Heidelberg, 1998, pp. 73–85.

[32] "Agilent." [Online]. Available: [http://www.chem.agilent.com/en-US/products-services/Instruments-Systems/Molecular-Spectroscopy/4100-ExoScan-Series-FTIR-\(handheld\)/Pages/default.aspx](http://www.chem.agilent.com/en-US/products-services/Instruments-Systems/Molecular-Spectroscopy/4100-ExoScan-Series-FTIR-(handheld)/Pages/default.aspx).

REPORT DOCUMENTATION PAGE				Form Approved OMB No. 0704-0188
<p>The public reporting burden for this collection of information is estimated to average 1 hour per response, including the time for reviewing instructions, searching existing data sources, gathering and maintaining the data needed, and completing and reviewing the collection of information. Send comments regarding this burden estimate or any other aspect of this collection of information, including suggestions for reducing this burden to Department of Defense, Washington Headquarters Services, Directorate for Information Operations and Reports (0704-0188), 1215 Jefferson Davis Highway, Suite 1204, Arlington, VA 22202-4302. Respondents should be aware that notwithstanding any other provision of law, no person shall be subject to any penalty for failing to comply with a collection of information if it does not display a currently valid OMB control number. PLEASE DO NOT RETURN YOUR FORM TO THE ABOVE ADDRESS.</p>				
1. REPORT DATE (DD-MM-YYYY) 27-Mar-2014		2. REPORT TYPE Master's Thesis		3. DATES COVERED (From — To) Sep 2012-Mar 2014
4. TITLE AND SUBTITLE Investigation of the Potential for FTIR as a Nondestructive Inspection Technique for Aircraft Coating Degradation		5a. CONTRACT NUMBER 5b. GRANT NUMBER 5c. PROGRAM ELEMENT NUMBER		
6. AUTHOR(S) Korth, Hans G, Capt, USAF		5d. PROJECT NUMBER 5e. TASK NUMBER 5f. WORK UNIT NUMBER		
7. PERFORMING ORGANIZATION NAME(S) AND ADDRESS(ES) Air Force Institute of Technology Graduate School of 2950 Hobson Way WPAFB OH 45433-7765		8. PERFORMING ORGANIZATION REPORT NUMBER AFIT-ENP-14-M-19		
9. SPONSORING / MONITORING AGENCY NAME(S) AND ADDRESS(ES) Intentionally Left Blank		10. SPONSOR/MONITOR'S ACRONYM(S) AFRL/RX		
		11. SPONSOR/MONITOR'S REPORT NUMBER(S)		
12. DISTRIBUTION / AVAILABILITY STATEMENT Distribution Statement A. Approved for Public Release; Distribution Unlimited				
13. SUPPLEMENTARY NOTES This material is declared a work of the U.S. Government and is not subject to copyright protection in the United States.				
14. ABSTRACT Polyurethane-based aircraft coating degradation was examined using Diffuse Reflectance Infrared Fourier Transform spectroscopy (DRIFTS). Two sample sets were aged in an autoclave; each containing four samples. Sample set A contained two as-cured samples and two samples treated to a level of visual degradation. Sample set B contained one sample left as-cured and three samples of differing degradation. DRIFTS spectra were collected on sample set B and singular value decomposition (SVD) was used to reveal trends between the degradation levels. Linear discriminant analysis (LDA) was then applied to the SVD coefficients to determine the most accurate spectral band for classification of unknown degradation. The 1220-850 cm ⁻¹ band proved to be the most accurate at discerning between degradation levels with 98.3% accuracy. The approach was then applied to sample set A using one each of the as-cured and degraded samples as unknown degradation levels. The prediction accuracy of LDA was 100% for the as-cured sample, but only 28% for the visibly degraded sample in the fingerprint region. When the misclassification cost was adjusted, the accuracy improved to 78%. It is recommended that this work continue towards generating a field NDI technique.				
15. SUBJECT TERMS FTIR; Singular Value Decomposition; Discriminant Analysis; Coatings; Polyurethane				
16. SECURITY CLASSIFICATION OF:		17. LIMITATION OF ABSTRACT	18. NUMBER OF PAGES	19a. NAME OF RESPONSIBLE PERSON Maj Timothy W. Zens, AFIT/ENP
a. REPORT U	b. ABSTRACT U	c. THIS PAGE U	UU	19b. TELEPHONE NUMBER (Include Area Code) (937) 255-3636 x4695; Timothy.Zens@afit.edu

Standard Form 298 (Rev. 8-98)
Prescribed by ANSI Std. Z39.18